

IVANA MATANOVIĆ

**KVANTNI OPIS GIBANJA VELIKE
AMPLITUDE U SUSTAVIMA S
VODIKOVOM VEZOM**

Doktorska disertacija

predložena Kemijskom odsjeku
Prirodoslovnog fakulteta Sveučilišta u Zagrebu
radi stjecanja akademskog stupnja
doktora prirodnih znanosti (kemija)

**Zagreb
2007.**

IVANA MATANOVIĆ

**QUANTUM TREATMENT OF
LARGE AMPLITUDE MOTION IN
HYDROGEN BONDED SYSTEMS**

Doctoral Thesis

submitted to the Department of Chemistry,
Faculty of Science, University of Zagreb,
for the academic degree of
Doctor of Natural Sciences (Chemistry)

**Zagreb
2007.**

Ovaj rad je većim dijelom izrađen u Grupi za teorijsku kemiju Zavoda za fizičku kemiju Instituta "Ruđer Bošković" pod vodstvom dr. sc. Nađe Došlić u sklopu projekta "Istraživanje kemijske reaktivnosti i femtokemijskih procesa" te projekta "Kontrola atomske i molekularne dinamike oblikovanim elektromagnetskim poljima" financiranih od Ministarstva znanosti obrazovanja i športa Republike Hrvatske. Dio rada izrađen je za vrijeme studijskog boravka na Freie Universität Berlin u radnoj grupi Prof. dr. Jörna Manza, pod vodstvom dr. sc. Olivera Kühna uz financijsku pomoć Humboldt fondacije. Rad je predan na ocijenu Kemijskom odsjeku Prirodoslovno-matematičkog fakulteta Sveučilišta u Zagrebu radi stjecanja akademskog stupnja doktora prirodnih znanosti (kemija).

The majority of this work has been carried out in the Theoretical Chemistry Group of the Physical Chemistry Department at Ruđer Bošković Institute under the supervision of dr. sc. Nađa Došlić and under projects "Investigation on chemical reactivity and ultrafast processes" (0098033) and "Control of atomic and molecular dynamics by shaped electromagnetic fields" supported by the Croatian Ministry of Science, Education and Sports. Part of the work had been done at the Freie Universität Berlin, in the workgroup of Prof. dr. Jörn Manz, under the supervision of dr. sc. Oliver Kühn, founded by the Humboldt foundation. The work was submitted to the Department of Chemistry, Faculty of Science, University of Zagreb, for the academic degree of Doctor of Natural Sciences (Chemistry).

Predgovor

...nastupit će vrijeme kada će brižljiva istraživanja vođena tijekom dugih razdoblja iznijeti na svjetlost dana ono što je još skriveno. Jedan životni vijek, čak kad bi se posve posvetio nebu, ne bi bio dovoljan da se protumači nešto tako prostrano...I tako će to znanje rascvjetati u toku dugog niza epoha. Nastupit će tada vrijeme kada će naši potomci biti zapanjeni da mi nismo znali ono što je njima samo po sebi jasno...

...Mnoga otkrića očuvana su za vrijeme koje tek dolazi, kada sjećanje na nas bude već izbljedjelo. Naš bi svijet bio ubogo mjesto da svakoj epohi nema ponuditi nešto za istraživanje...priroda ne otkriva svoje tajne odjednom i svima...

Seneca, Naturales questiones

Ovom prilikom želim najiskrenije zahvaliti mom voditelju, dr. Nađi Došlić na ne-sebičnoj pomoći, podršci i strpljenju tijekom izrade ove teze, čovjek rijetko ima sreću imati tako posebnog mentora. Također zahvaljujem prof. Jörnu Manzu i Oliveru Kühnu na pruženom gostoprimstvu i pomoći tijekom studijskog boravaka u Berlinu, te Humboldt fondaciji za financijsku pomoć. Hvala članovima Grupe za teorijsku kemiju za sve pomoći, razgovore i ustupke. Pogotovo dr. I. Ljubiću, G. Kovačeviću, dr. D. Babiću te Kalle Kahru.

Veliko hvala mojoj mami, tati i sestri što su u svim situacijama uz mene.

Hvala Marinu...

Contents

1	Introduction	1
2	Model systems	7
2.1	Intramolecular hydrogen bonding in acetylacetone	7
2.2	Intermolecular hydrogen bonding in the formic acid dimer	12
3	Fundamentals of vibrational spectroscopy	16
3.1	Vibration rotation tunneling spectroscopy	16
3.2	Small amplitude treatment	23
3.2.1	Normal coordinates	23
3.2.2	Treating anharmonicity	30
3.3	Large amplitude treatment	35
3.3.1	Internal coordinates	35
3.3.2	Minimum energy path based methods	38
3.3.3	Collective large amplitude coordinates	39
4	Results and discussion	45
4.1	Electronic structure calculations	45
4.1.1	Acetylacetone	45
4.1.2	The formic acid dimer	54
4.2	Normal mode based approaches	58
4.2.1	Acetylacetone	58
4.2.2	The formic acid dimer	74
4.3	Large amplitude approaches	81
4.3.1	Internal coordinates	81
4.3.2	Reaction Space Hamiltonian approach	93
4.3.3	Generalized approximation to the reaction path	109
4.3.4	Summary and outlook	116
5	Conclusion	119

Bibliography	122
A The Eckart Equations	xvi
B The Fourier Grid Hamiltonian method for solving the vibrational Schrödinger equation	xix
C List of abbreviations	xxi
C.1 Notation	xxi
C.2 Abbreviations	xxii

University of Zagreb

Doctoral Thesis

Faculty of Science

Department of Chemistry

QUANTUM TREATMENT OF LARGE AMPLITUDE MOTION IN HYDROGEN BONDED SYSTEMS

Ivana Matanović

Ruđer Bošković Institute, Bijenička cesta 54

The large amplitude internal motion (LAM) of the bridging hydrogen represents the key feature of H-atom transfer systems. Several methods are employed in order to gain new insight into H-atom transfer (HAT) dynamics in acetylacetone (ACAC) and formic acid dimer (FAD), molecules that serve as prototype systems for single and multiple HAT reactions. The IR spectra related to the OH...O fragment of ACAC and FAD were first analyzed using a combination of a second order perturbative treatment and direct solution of the nuclear Schrödinger equation in reduced dimensionality. While capable of describing general features of IR spectra, normal mode based methods are unsuited to account for the double minimum nature of the potential surface, and thus unable to reproduce the results of high resolution ro-vibrational spectroscopy. Further, three quantum methods capable of quantitatively describing the LAM dynamics are discussed. The first method is based on localized internal coordinates and in the other two methods collective LA coordinates are constructed using the minimum energy path geometries. In the two last cases, the remaining orthogonal degrees of freedom are linearized and the FAD dynamics is treated within the reaction surface Hamiltonian approach. Results for the ground and excited state tunneling splittings are confronted with the results of the experimental high resolution spectrum.

(129 pages, 41 figures, 21 tables, 118 references, original in English language)

Thesis deposited in Central Chemical Library, Horvatovac 102a

Keywords: acetylacetone / formic acid dimer / hydrogen atom transfer / large amplitude motion / tunneling splitting

Supervisor: Dr. sc. Nađa Došlić, v. zn. sur.

Reviewers: Dr. sc. Oliver Kühn, privat doc., Dr. Tomica Hrenar, doc.

Thesis accepted:

Sveučilište u Zagrebu

Doktorska disertacija

Prirodoslovno-matematički fakultet

Kemijski odsjek

**KVANTNI OPIS GIBANJA VELIKE AMPLITUDE U
SUSTAVIMA S VODIKOVOM VEZOM***Ivana Matanović**Institut Ruđer Bošković, Bijenička cesta 54*

U teorijskom smislu gibanje velike amplitude predstavlja ključni korak u razumijevanju dinamike sustava s vodikovom vezom. Teza se bavi razvojem teorijskih metoda za opis gibanja velike amplitude te njihovom primjenom na dvije modelne reakcije, jednostruki intramolekularni prijenos vodika u acetilacetonu (ACAC) i dvostruki intermolekularni prijenos vodika u dimeru mravlje kiseline (FAD). Infracrveni spektar $\text{OH} \cdots \text{O}$ fragmenta u ACAC i FAD-u analiziran je početno perturbacijskom teorijom i direktnim rješavanjem Schrödingerove jednadžbe za jezgre u reduciranoj dimenzionalnosti. Nađeno je da ove metode, temeljene na opisu u normalnim koordinatama, na zadovoljavajući način opisuju opće značajke IR spektra, ali nisu pogodne ukoliko se želi reproducirati potencijal dvostruke jame karakterističan za sustave s vodikovom vezom, pa stoga ne mogu objasniti cijepanja ro-vibracijskih nivoa u IR spektrima visokoga razlučivanja. Za objašnjenje cijepanja ro-vibracijskih nivoa primjenjene su tri kvantne metode. Prva metoda temelji se na opisu u lokaliziranim internim koordinatama, dok se druge dvije metode temelje na definiranju ortogonalnih kolektivnih koordinata velike amplitude pomoću geometrija sustava na putu minimalne energije. U posljednja dva slučaja preostali, ortogonalni stupnjevi slobode uključeni su kroz harmoničku aproksimaciju i dinamika FAD-a tretirana je koristeći Hamiltonian reakcijske plohe. Dobivena cijepanja u osnovnom i pobuđenim vibracijskim stanjima uspoređena su sa vrijednostima dobivenim iz ro-vibracijskih spektara visokog razlučivanja.

(129 stranica, 41 slika, 21 tablica, 118 literaturnih navoda, engleski jezik)

Rad je pohranjen u Centralnoj kemijskoj biblioteci, Horvatovac 102a

Ključne riječi: acetilaceton/ dimer mravlje kiseline / prijenos vodikova atoma / gibanje velike amplitude

Mentor: Dr. sc. Nađa Došlić v. zn. sur.

Ocjenitelji: Dr. sc. Oliver Kühn, privat docent, Dr. sc. Tomica Hrenar, doc.

Rad prihvaćen:

Sveučilište u Zagrebu

Doktorska disertacija

Prirodoslovno-matematički fakultet

Kemijski odsjek

KVANTNI OPIS GIBANJA VELIKE AMPLITUDE U SUSTAVIMA S VODIKOVOM VEZOM

Ivana Matanović

Institut Ruđer Bošković, Bijenička cesta 54

Istraživanja formiranja i dinamike vodikovih veza od presudne su važnosti za razumijevanje brojnih kemijskih i bioloških procesa. Vodikove veze određuju strukturu i svojstva vrlo različitih molekula, od molekule vode do proteina i DNA. Cilj teze je razumijevanje ovih važnih interakcija na fundamentalnoj osnovi, prvenstveno vibracijske spektroskopije ovih sustava.

Poznato je da stvaranje vodikove veze $A-H \cdots B$ između donora vodikova atoma (A) i akceptorske grupe (B) uzrokuje specifičan otisak u vibracijskom spektru molekule. Stvaranjem vodikove veze, vrpca $A-H$ istezanja postaje šira te se, u odnosu na slobodnu $A-H$ vezu, pomiče prema crvenom dijelu spektra. Ove osobine, uzrokovane anharmoničkim sprežanjem visoko-frekventnog moda $A-H$ istezanja i nisko-frekventnih modova molekulskog kostura, upućuju na višedimenzionalnu prirodu Born-Oppenheimerova potencijala sustava s vodikovom vezom. S druge strane, gibanje vodikova atoma između donorske (A) i akceptorske (B) grupe predstavlja gibanje velike amplitude pa razumijevanje vibracijskih spektara sustava u kojima se dešava prijenos vodikova atoma zahtijeva primjenu posebnih teorijskih opisa. Jedno od najvažnijih pitanja vezano uz infracrvenu spektroskopiju ovakvih sustava je cijepanje vibracijskih nivoa molekule uzrokovano potencijalom dvostruke jame. Danas postoje razne metode kojima se cijepanje osnovnog stanja može izračunati s velikom točnošću. No, proračun cijepanja u pobuđenim vibracijskim stanjima predstavlja neriješen problem. Rješavanje navedenih problema omogućilo bi izravno zaključivanje o utjecaju pobuđenja pojedinih vibracijskih modova na dinamiku prijenosa vodikova atoma, odnosno o utjecaju prijenosa vodikova atoma na vibracijske modove sustava.

Razvijeni teorijski pristupi iskorišteni su za opis reakcija prijenosa vodikova atoma u acetalacetonu (ACAC) i dimeru mravlje kiseline (FAD), dviju molekula koje predstavljaju modelne sustave za reakcije jednostrukog i dvostrukog prijenosa vodikova atoma. Male molekule kao ove predstavljaju idealne sustave za proučavanje problematike vezane uz strukturu i dinamiku sustava s vodikovom vezom. Istovremeno,

mnoštvo dostupnih eksperimentalnih podataka omogućuju testiranje uspješnosti teorija. Upravo razvoj i testiranje pouzdanih teorijskih metoda na jednostavnim, modelnim molekulama predstavlja ključni korak prema kvantitativnom opisu reakcija prijenosa vodika u velikim sustavima od biološke važnosti.

Iako se već nekoliko desetljeća pentan-2,4-dion, poznat kao i acetilaceton, istražuje upotrebom mnogih eksperimentalnih i teorijskih metoda, još uvijek se malo zna o mehanizmu prijenosa vodikova atoma u toj molekuli. Teorijski opis ovog sustava otežan je sprežanjem reakcije prijenosa vodikova atoma s internom rotacijom metilnih skupina. S druge strane, veliki broj eksperimentalnih podataka, od kojih je za ovaj rad najvažniji IR spektar u plinskoj fazi, omogućuje usporedbu teorijskih predviđanja i eksperimentalnih rezultata.

Nadalje, veliki broj teorijskih radova odnosi se na reakciju prijenosa vodikova atoma u dimeru mravlje kiseline jer ova molekula predstavlja najjednostavniji dimer iz skupine karboksilnih kiselina te predstavlja prototip reakcije višestrukog prijenosa vodikova atoma. Teorijski interes je dodatno pojačan nedavno snimljenim vibracijsko-rotacijsko-tunelirajućim (VRT) spektrom visoke rezolucije. Izmjereno je cijepanje u osnovnom vibracijskom stanju molekule (DCOOH)₂ kao i cijepanje u modu antisimetričnog C-O istezanja. Iako postoje određene nejasnoće vezane uz intenzitete pojedinih prijelaza, autori su zaključili da pobuđenje ovoga vibracijskog moda ubrzava reakciju prijenosa vodika i odredili cijepanje u osnovnom nivou kao 0.00286(25) cm⁻¹ a u pobuđenom vibracijskom stanju kao 0.00999(21) cm⁻¹. Ipak, upozoreno je na mogućnost alternativne asignacije po kojoj bi mod antisimetričnog C-O istezanja bio mod koji usporava reakciju prijenosa vodika (cijepanje u osnovnom novou tada bi iznosilo 0.0125 cm⁻¹ a u pobuđenom vibracijskom nivou 0.00313 cm⁻¹). Većina teorijskih radova odnosila se na račun cijepanja u osnovnom vibracijskom nivou molekule, a gotovo su svi rezultati potvrdili originalnu asignaciju. Do sada postoji samo jedan teorijski rad koji je u proračun uključio mod C-O istezanja, a autori su potvrdili alternativnu asignaciju. Ipak, kako se radi o računu aproksimativnom instanton teorijom čija je primjena u frekvencijskom području C-O istezanja diskutabilna, nejasnoće vezane uz asignaciju VRT spektra ostaju.

Računi elektronske strukture

Šest stacionarnih točaka na plohi potencijalne energije acetilacetona značajnih za reakciju intramolekulskog prijenosa vodika te rotacije metilnih skupina analizirano je koristeći *ab initio* metode, teoriju funkcionala gustoće (DFT) s raznim osnovnim skupovima. Barijera za prijenos vodika procijenjena je na 3.03 kcal mol⁻¹ na CCSD(T)/cc-pVTZ//MP2(FC)/cc-pVTZ razini teorije. Numerički rezultati slične kvalitete mogu se dobiti

upotrebom računski isplativije DFT/B1LYP metode. Račun puta najmanje energije i analiza normalnih modova u točkama na putu najmanje energije utvrdile su da je reakcija prijenosa vodika spregnuta s rotacijom distalne metilne skupine ali se dva procesa ne dešavaju istovremeno: krećući od minimuma, prijenos vodika se dešava tek nakon što se metilne skupine u ACAC-u postave u zasjenjenu konformaciju. Barijera za rotaciju distalne metilne skupine procijenjena je na 0.27 kcal mol⁻¹ na CCSD(T)/cc-pVTZ//MP2(FC)/cc-pVTZ razini teorije.

U slučaju dimera mravlje kiseline, strukture značajne za reakciju prijenosa vodika u FAD-u proučavane su upotrebom *ab initio* MP2 metoda, DFT/B3LYP metode, te teorije spregnutih grozdova. Barijera za prijenos vodika procijenjena je na 7.89 kcal mol⁻¹ na CCSD(T)/aug-pVTZ//MP2(FC)/aug-pVTZ razini teorije. Pozornost je usmjerena na proučavanje učinkovitosti B3LYP/6-31+G(d) te B3LYP/6-311++G(3df,3pd) metoda u opisu energetike te strukturnih svojstava dimera jer se radi o metodama vezanim uz dosadašnje račune dinamike vodikove veze. Nađeno je da B3LYP/6-31+G(d) daje rezultate slične referentnim vrijednostima dobivenim upotrebom teorije spregnutih grozdova. Ipak, nakon što je kod metoda proučen utjecaj greške zbog superpozicije osnovnog skupa, upozoreno je da se kod B3LYP/6-31+G(d) metode radi o mogućem povoljnom poništavanju pogrešaka.

Koordinate male amplitude

Područje IR spektara koje odgovara O-H...O fragmentu u ACAC i FAD-u proučeno je teorijom perturbacije drugog reda te direktnim rješavanjem Schrödingerove jednadžbe u reduciranoj dimenzionalnosti. Pokušalo se zaključiti o interakcijama i efektima koje određuju položaj, oblik i širinu vrpce koja odgovara OH istezanju. IR spektar ACAC proučen je korištenjem četverodimenzijskog modela razapetog modom OH istezanja (ν_{OH}), OH savijanja u ravnini (δ_{OH}) te dvama niskofrekventim modovima $\nu_{OH...O}$ i ν_{OO} . U slučaju FAD-a različiti dvodimenzijski i trodimenzijski potencijali razapeti su IR aktivnim modom antisimetričnog O-H istezanja (ν_{OH}) te jednim od sljedećih modova: IR neaktivnim simetričnim O-H istezanjem (ν_{OH}), simetričnim i antisimetričnim C=O i C-O istezanjima ($\nu_{C=O}$ i ν_{C-O}) te simetričnim i antisimetričnim savijanjima OH veze u ravnini (δ_{OH}). U nisko frekvencijskom području uzeti su u obzir istezanje dimera te simetrično i antisimetrično njihanje u ravnini. U ovom pristupu vibracijski Hamiltonian ima sljedeći oblik:

$$\hat{H}_v = -\frac{\hbar^2}{2} \sum_{i=1}^{\tilde{n}} \left[\frac{1}{\mu_i} \frac{\partial^2}{\partial Q_i^2} \right] + V(Q_1, \dots, Q_{\tilde{n}})$$

gdje \tilde{n} označava dimenziju problema, a μ_i reduciranu masu normalnog moda Q_i . Vlastite vrijednosti i vlastite funkcije vibracijskog Hamiltoniana dobivene su korištenjem Fourier

grid Hamiltonian metode uz Lanczosovu diagonalizaciju. Iz izračunatih vibracijskih spektara zaključeno je da je za širinu vrpce OH istezanja u ACAC-u zaslužno postojanje dviju enolnih formi acetilacetona jer su prijelazi s najvećim intenzitetom u dvije konformacije (s metilima u zasjenjenoj i s metilima u antiperiplanarnoj konformaciji) razmaknuti za više od 500 cm^{-1} . Vrpca također pokazuje efekte kao što su snažno sprezanje s niskofrekventnim vibracijama te ne postojanje osnovnog prijelaza OH istezanja. Ove karakteristike mogu se smatrati općim značajkama vibracijske dinamike intramolekulskih vodikovih veza. Vezano uz FAD, zaključeno je da je crveni pomak antisimetričnog OH istezanja isključivo uzrokovan Davydovim sprežanjem sa IR neaktivnim modom simetričnog OH istezanja. Anharmonička sprežanja s niskofrekventnim modovima te Fermijeve rezonancije s modovima iz središnjeg IR područja doprinose širini i obliku, ali ne i položaju vrpce OH istezanja u FADu.

Koordinate velike amplitude

Hamiltonian u internim koordinatama

U ovoj metodi prijenos vodikova atoma u ACAC-u i FAD-u opisan je simetrijski prilagođenim internim koordinatama. Pri konstrukciji plohe potencijalne energije odabrani, interni stupnjevi slobode tretiraju se egzaktno dok se energija sustava minimizira s obzirom na preostale stupnjeve slobode. Za račun vibracijskih nivoa potrebno je riješiti vibracijsku Schrödingerovu jednadžbu čiji operator kinetičke energije ima oblik

$$\hat{T}_v \simeq -\frac{\hbar^2}{2} \sum_{r=1}^{\tilde{n}} \sum_{s=1}^{\tilde{n}} \frac{\partial}{\partial \rho_r} \left[G^{rs} \frac{\partial}{\partial \rho_s} \right]$$

Izraz sadrži koordinatno ovisnu G -matricu definiranu kao

$$G^{rs} = \sum_{i=1}^{3N} \frac{1}{m_i} \frac{\partial \rho_r}{\partial x_i} \frac{\partial \rho_s}{\partial x_i}$$

koja ima ulogu koordinatno ovisnih reduciranih masa te približno uzima u obzir sprežanje između egzaktno tretiranih internih i preostalih stupnjeva slobode molekule. Različitim aproksimacijama u kinetičkom dijelu Hamiltoniana može se zaključivati o važnosti uključivanja kinematičkog sprežanja. U slučaju acetilacetona ploha potencijalne energije razapeta je trima internim koordinatama $\rho_1 = r_1 + r_2$, $\rho_2 = r_1 - r_2$ i $\rho_3 = \theta$ gdje r_1 opisuje udaljenost vodikova atoma od kisikova atoma, donora vodikova atoma, r_2 udaljenost vodikova atoma od kisikova atoma akceptora vodika, a kut θ predstavlja kut između kisika, atoma donora vodikova atoma i kisika akceptora i uzima u obzir udaljenost između atoma donora i akceptora vodikova atoma. U slučaju FAD-a, upotrebene su dvije analogne interne koordinate koje uzimaju u obzir simetrični, sinkroni prijenos

vodikovih atoma te udaljenost između monomera u dimeru. Nakon rješavanja vibracijskog problema za ACAC upotrebom Fourier Grid Hamiltonian metode u internim koordinatama, određeno je cijepanje u osnovnom stanju ACAC-a kao 116 cm^{-1} , a u modu OH istezanja kao 850 cm^{-1} koristeći B1LYP/6-311G(d) metodu za konstrukciju potencijala. Također se zaključilo da bi zanimljiva i dosad ne objašnjena struktura vrpce C=O istezanja s tri maksimuma mogla biti posljedica cijepanja u vrpce OH istezanja uzrokovano reakcijom prijenosa vodika. Za FAD određeno je cijepanje u osnovnom vibracijskom nivou kao 0.011 cm^{-1} na B3LYP/6-311++G(3df,3pd) nivou teorije. U oba slučaja je višedimenzionalna priroda reakcije prijenosa H atoma dovela do snažne koordinatne ovisnosti elemenata G -matrice pa je za dobivanje kvantitativnih rezultata bilo presudno na točan način uključiti kinematička sprežanja.

Metode Kartezijske reakcijske plohe i Opća aproksimacija reakcijskog puta

Ove metode temelje se na ideji separacije koordinatnog prostora u prostor reakcijske plohe (sustav) i prostor harmoničkih pomaka od plohe (okolina). Konstrukcija koordinata koje razapinju prostor reakcijske plohe temelje se u oba slučaja na putu najmanje energije koji povezuje prijelazno stanje i reaktant (produkt). Istražene su dvije opcije za opis koordinate prijenosa vodikova atoma:

- (i) korištenje skupa ortogonalnih delokaliziranih koordinata koje se nizom kinematičkih rotacija reduciraju na manji broj koordinata koje mogu uspješno reproducirati put najmanje energije (Opća aproksimacija reakcijskog puta)
- (ii) korištenje relevantnih geometrija na putu najmanje energije i konstrukcija kolektivnih koordinata linearnom kombinacijom kartezijevih koordinata relevantnih geometrija (Metoda Kartezijske reakcijske plohe)

U oba slučaja preostali, ortogonalni stupnjevi slobode (okolina) tretiraju se kao harmonički pomaci oko reakcijske plohe razapete koordinatama pod (i) i (ii). U slučaju FAD-a uz koordinate velike amplitude (ovdje označene kao d_1, d_2, d_3) u konstrukciji plohe uključena su dva dodatna stupnja slobode (q_a, q_s) čija kombinacija reproducira mod antisimetričnog C-O istezanja čije je cijepanje određeno u VRT spektru visoke rezolucije. Vibracijski Hamiltonian oblika

$$\hat{H}_v = -\frac{1}{2} \sum_{i=1}^3 \frac{\partial^2}{\partial d_i^2} - \frac{1}{2} \sum_{k=1}^2 \frac{\partial^2}{\partial q_k^2} + V(d_1, d_2, d_3, \mathbf{q} = 0) + \sum_{k=1}^2 \left. \frac{\partial V(d_1, d_2, d_3, \mathbf{q})}{\partial q_k} \right|_{q=0} q_k + \frac{1}{2} \sum_{k,l=1}^2 \left. \frac{\partial^2 V(d_1, d_2, d_3, \mathbf{q})}{\partial q_k \partial q_l} \right|_{q=0} q_k q_l$$

riješen je korištenjem reprezentacije Hamiltoniana na mreži (Fourier grid Hamiltonian metoda) te korištenjem Lanczos diagonalizacije. Određeno je cijepanje u osnovnom vibracijskom nivou FAD-a kao 0.155 cm^{-1} , a u modu antisimetričnog C-O istezanja kao 0.0655 cm^{-1} na B3LYP/6-311++G(3df,3pd) nivou teorije, te 0.0012 cm^{-1} i 0.0032 cm^{-1} na B3LYP/6-31+G(d) nivou. Ovi rezultati upućuju na alternativnu asignaciju VRT spektra iz 2002. po kojoj bi mod C-O istezanja bio mod čije pobuđenje usporava reakciju prenosa vodika. Rezultati su u slaganju s najnovijim VRT spektrom $(\text{HCOOH})_2$ snimljenim 2007. prema kojemu je cijepanje u osnovnom nivou određeno kao 0.0158 cm^{-1} a u vibracijski pobuđenom nivou kao 0.0100 cm^{-1} . Pogreška u apsolutnim vrijednostima za cijepanja pripisana je nemogućnošću metoda kvantne kemije da točno procijene visinu barijere za reakciju prijenosa vodika. Ipak, relativne vrijednosti cijepanja gotovo su kvantitativno reproducirane.

Za razliku od internih koordinata koje mogu opisati gibanja velike amplitude ali daju komplicirani oblik vibracijskog Hamiltoniana, koordinate opisane u okvirima metode Reakcijske plohe i Opće aproksimacije reakcijskog puta predstavljaju kolektivne koordinate koje daju diagonalan oblik operatora za kinetičku energiju. Uključivanje proizvoljnih vibracijskih modova u račun je jednostavno, pa se ove dvije metode mogu smatrati metodom izbora kod tretiranja dinamike u pobuđenim vibracijskim stanjima.

Chapter 1

Introduction

Hydrogen bonds (HB) and *hydrogen atom transfer* (HAT)¹ reactions represent important concepts in life sciences [3]. A hydrogen bond represents a special type of attractive interaction, stronger than van der Waals but weaker than a covalent bond, usually existing between an electronegative atom and a hydrogen atom bonded to another electronegative atom. The most fundamental example of hydrogen bonds is found between water molecules where they determine its unique and essential for life properties (for example temperature of maximum density or its specific heat capacity). Furthermore, hydrogen bonds play an important role in determining the three-dimensional structures of proteins and nucleic basis and consequently influence their physiological or biochemical functions. For instance, much of the binding selectivity of some proteins comes from the hydrogen bond formation between the protein and its substrate [4]. A wide range of enzyme reactions and pumping mechanisms of transmembrane proteins also include hydrogen atom or proton exchange between the donor and an acceptor group [5, 6]. HAT reactions also occur in DNA base pairs such as adenine-thymine and have even been hypothesised as a possible cause of spontaneous point mutations in DNA [7].

Although the term hydrogen bond emerged after 1930 (Pauling, Huggins) the idea of a weak interactions involving hydrides dates from the end of 19th century. Since then a vast number of studies on different aspects of hydrogen bonded interactions and

¹In general one distinguishes hydride, hydrogen atom and proton transfer depending on the degree of charge transfer. In principle, the former two cases can be viewed as types of proton-coupled electron transfer reactions, since they involve the coupled transfer of protons and electrons [1]. On the other hand the transfer of proton can be coupled to simultaneous transfer of the negative charge along different pathways, for instance through conjugated systems [2]. There exists an inconsistency in literature concerning the distinction of the hydrogen and proton transfer processes, much due to the fact that for certain systems it is very difficult to determine whether a proton transfer or hydrogen atom transfer occurs. In this thesis the electrostatic aspects of the problem will not be the issue and the processes will be always referred as hydrogen atom transfer reactions.

hydrogen atom transfer reactions were reported. This is reflected in a great number of papers, review articles and books covering this phenomena. But even today, with significant advances in theoretical and computational methodology, the description and the understanding of hydrogen bonded systems still presents a significant challenge to theory. Much of the difficulty is due to the specific nature of the transferring hydrogen, which is, being the lightest element, especially prone to quantum effects such as delocalization, tunnelling phenomena and *large amplitude motion* (LAM). Moreover, the formation of the hydrogen bond $A-H \cdots B$ between a hydrogen donor (A) and hydrogen acceptor group (B) produces anharmonic couplings between the hydrogen atom motion and the motion of the molecular frame of the system. Thus, for a quantitative understanding of such processes, an accurate treatment of the HB dynamics on multidimensional potential energy surfaces (PESs) is required [8].

From the experimental side, vibrational spectroscopy, both in the frequency and time domains, has proven to be a valuable tool for investigating HB systems [3, 9]. The formation of a hydrogen bond leaves a characteristic imprint in the vibrational spectra of the molecule. Upon hydrogen bonding the A-H stretching band is red-shifted and broadened compared to the free A-H stretch [10]. These features allow us to correlate the A-H band profile to the strength of the HBs and to the shape of the underlying potential [11]. Already early theoretical works showed that the potential energy curves for the motion of hydrogen strongly depend on a distance between the hydrogen donor (A) and hydrogen acceptor group (B) [8]. Accordingly, upon decreasing the donor-acceptor distance, the nature of the potential changes drastically, i.e., the double minima shape of the potential changes to a single minima potential.

According to the strength hydrogen bonds can be classified into weak ($1-4 \text{ kcal mol}^{-1}$), medium strong ($4-15 \text{ kcal mol}^{-1}$) and strong hydrogen bonds ($15-40 \text{ kcal mol}^{-1}$).

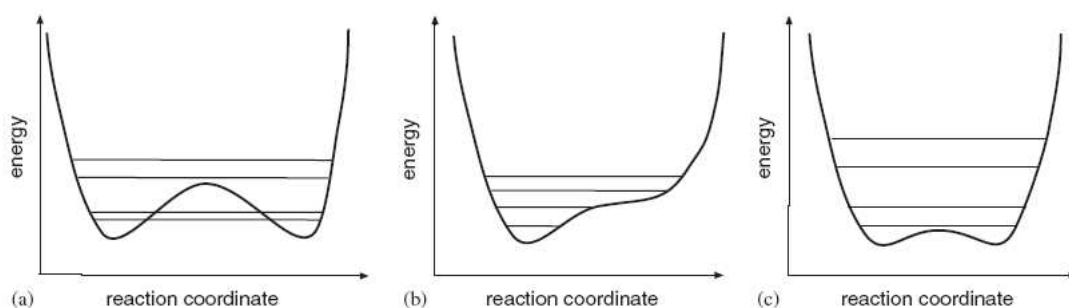


Figure 1.1: Potential energy curves for (a) weak symmetric (b) moderate asymmetric (c) strong symmetric HBs. Figure courtesy of K. Giese et al., *Physics Reports* **430** (2006) 211.

Weak HB systems (Figure 1.1a) are characterized with A-B distances that exceed 2.8-3.2 Å and spectroscopically with the A-H stretching band in the infrared (IR) spectrum which is located between the 3330 and 3500 cm⁻¹. The PES of weak HB systems exhibit a double minimum structure with a relatively large barrier height for HAT reaction. The hydrogen atom transfer reaction between the two minima can occur as a thermally activated process (over the reaction barrier) or as a tunneling process (through the barrier) depending on the height and width of the barrier and on the position of the zero-point energy. This gives rise to a splitting of each rotational-vibrational state of the molecule into two states which are separated by the energy

$$\Delta E = h\nu_{\text{tunneling}}$$

where $\nu_{\text{tunneling}}$ is the tunneling frequency. The period of the tunneling is related to the tunneling splitting by $\tau = 1/\nu_{\text{tunneling}}$. Medium strong HBs have much lower HAT barriers as a consequence of a shorter A-B distance ranging between 2.5 Å and 3.2 Å. In this case, the A-H stretching band is located between the 2600-3300 cm⁻¹. The case of an asymmetric (A-H...B) medium strong HB is shown in Figure 1.1b. Strong HBs, usually called "low-barrier hydrogen bonds", are characterized with HB distances less than 2.5 Å. The barrier between the two minima is much smaller and the zero point energy often exceeds the barrier height (Figure 1.1c). Nevertheless, the double-well shape of the potential still has a strong influence on the vibrational spectra of the molecule and will lead to the doubling of rovibrational states. A further shortening of the HB distance would lead to the single-well potential but such bonds are thought to exist only in [FHF]⁻ and [HO-HOH]⁻ ions with the F-F and O-O distances of 2.26 Å and 2.29 Å.

The effect of hydrogen bond formation on IR and Raman spectra had been realized in the thirties [12] and has been later extensively studied, both experimentally and theoretically. A contribution by D. Hadži and coworkers on this subject has been especially valuable [10, 13]. As a result of the development in laser technology in the eighties, new experimental techniques provided valuable insights into HB systems and triggered new theoretical investigations. Due to the high resolution obtained in IR spectroscopy, the transitions between the rovibration levels of the molecule, split due to the hydrogen atom transfer, could be measured and compared to the theoretical predictions. In the past twenty years the splitting of the ground vibrational level in small model molecules (like malonaldehyde, formic acid dimer or tropolone) has been a subject of extensive experimental [14, 15] and theoretical studies [16, 17, 18, 19]. Consequently, a significant methodological advances in both electronic structure and dynamical treatments have been obtained [20, 21, 22] and nowadays the ground state tunnelling splitting can

be calculated with remarkable accuracy. For instance, in malonaldehyde the ground state tunneling splitting of $25.7 \pm 0.3 \text{ cm}^{-1}$ was obtained using the exact diffusion Monte Carlo and the projection operator imaginary time spectral evolution methods [23]. The computed tunneling splitting is slightly higher than the experimental value of 21.58 cm^{-1} [24]. However, the understanding of splittings in the excited vibrational states and the modelling of vibrational spectra of intramolecular HAT systems in general, still presents a significant challenge to theory [25, 26].

The present work will focusses on the vibrational spectroscopy of the small model molecules, which can serve as prototype systems for the understanding of hydrogen bonded systems and single and multiple HAT reactions. First we consider the enol form of pentane-2,4-dione, known as acetylacetone (ACAC) (Figure 2.1). This system has been extensively studied both experimentally [27, 28, 29] and theoretically [30, 31, 32], but the pathways of the HAT reaction in ACAC are still not well understood. Compared to its simpler analogue malonaldehyde (MA), the theoretical description in ACAC is complicated by the coupling of the transferring hydrogen atom to the internal rotation of the two methyl groups [33]. On the other hand, spectroscopic information about the OH stretching region of the IR spectra in MA are scant due to the very low intensity of the OH stretch band thus preventing the direct comparison between the theoretical description and experiment [34, 35]. The situation is rather different in ACAC where the IR spectra is dominated by a broad OH stretching band located between 1800 and 3400 cm^{-1} [28, 29].

The second model system is the formic acid dimer (FAD), a prototype example exhibiting double hydrogen bonds (Figure 2.4). Due to the importance of the double HAT reactions in nature a great number of theoretical studies of FAD have been reported thus far [17, 18, 36, 37, 38]. A large number of them emerged recently, triggered by the high resolution vibration-rotation-tunneling (VRT) spectrum of $(\text{DCOOH})_2$ in the gas phase reported by F. Madeja and M. Havenith in 2002 [14]. They reported the ground state tunnelling splitting of $0.00286(25) \text{ cm}^{-1}$ and the splitting in the antisymmetric C-O stretching mode as $0.00999(2) \text{ cm}^{-1}$. Despite the lack of precise intensity measurement for weak *a*-type transitions between the rovibration levels of FAD, they assumed that the HAT is accelerated upon the vibrational excitation of the molecule. Their conclusion was based on the earlier theoretical work on the ground state tunneling splitting in FAD where, based on a three-dimensional reaction surface model, a ground state splitting of 0.004 cm^{-1} was predicted [39]. Their second argument was the enhancement of hydrogen atom tunneling upon the excitation of an O-O stretching vibration in malonaldehyde [17, 40]. Nevertheless the authors also pointed out the possibility of an alternative assignment for the observed splittings (ground state: $0.125(3) \text{ cm}^{-1}$, excited

state: $0.0031(3) \text{ cm}^{-1}$), in which the CO stretching mode is a mode which suppresses the tunnelling. Despite the large number of theoretical papers on the ground state tunneling splitting [17, 18, 36, 39, 41, 42, 43], apart from the work presented in this thesis, only Z. Smedarchina and coworkers included the CO stretching mode directly in their computation [43, 44]. All the results on the ground state tunneling splitting supported the original assignment of the $(\text{DCOOH})_2$ spectra. Surprisingly, the work of Z. Smedarchina et al. supported the alternative assignment. However, the computation was performed by using the approximate instanton theory whose validity in treating the excited vibrational states is questionable [42] and part of the controversy remained unsolved. Independently of the theoretical work presented here, high resolution spectrum of $(\text{HCOOH})_2$ in the region of the antisymmetric C-O stretch vibration was recorded and analyzed by M. Ortlieb and M. Havenith in 2007 [45]. The ground state tunneling splitting in $(\text{HCOOH})_2$ was determined as $0.0158(4) \text{ cm}^{-1}$ which is close to the value of $0.0123(3) \text{ cm}^{-1}$ for $(\text{DCOOH})_2$ for the reversed assignment. According to the authors this strongly supports the alternative assignment for the $(\text{DCOOH})_2$ classifying the antisymmetric C-O stretching mode as a tunneling suppressing mode. This nicely exemplifies the complexity of the multidimensional tunneling dynamics and embraces a number of interesting issues. One of the most important being the physical reason under which a vibrational excitation promotes or suppresses the tunneling.

In summary, this work is oriented towards the understanding of the HAT reactions in simple benchmark systems which will:

- help to clarify the pathways and time-scales of hydrogen dynamics
- clarify the ways in which the vibrational excitation of the system influences the tunnelling rates as well as the ways in which the HAT dynamics affects the vibrational modes of the system

and most importantly

- provide and test a reliable theoretical method capable of describing quantitatively the large amplitude motion of the transferring hydrogen and of the explaining experimental observations, particularly the mode specific tunnelling dynamics.

Outline of the work

The thesis is organized as follows.

Chapter 2 gives a short literature overview of the most important theoretical and experimental results concerning the molecules that are contained in this work as model systems for single and double HAT reactions.

Chapter 3 is concerned with fundamentals of vibrational spectroscopy. First, the basics of molecular symmetry and the selection rules used in the assignment of the rovibrational transitions resolved in high resolution spectra of HB systems are given. Further, the theoretical background is introduced. Special attention is paid to the nature of the coordinates used to describe small and large amplitude motion. The quantum-dynamical methods based on the introduced coordinates that are essential for this work are detailed.

Chapter 4, which contains the results and discussion, is further divided into three sections. In section 4.1 the results of electronic structure calculations on model molecules are presented. This is crucial for providing a reliable and computationally efficient quantum chemical method for the construction of the PESs needed for further calculations. Section 4.2 presents the results of the normal mode based methods, i.e., the IR spectra related to the OH \cdots O fragment of ACAC and FAD is analyzed using a combination of a second order perturbative treatment and direct solution of the nuclear Schrödinger equation in reduced dimensionality. However, normal mode coordinates model the motion in the vicinity of the most stable conformation, while capable of describing the general features of infrared spectra, are unsuited to account for the double minimum topology of the potential surface. As a result, normal mode based methods are unsuitable for reproducing the results of high resolution VRT spectroscopy. Section 4.3 introduces three large amplitude approaches in order to quantitatively describe the large amplitude internal motion of the transferring hydrogen in FAD. They are an internal coordinate approach, the Reaction Surface Hamiltonian (RSH) method and the Generalized approximation to the reaction path method (GARP). Comparison between the methods will be provided on the PESs of the same quantum-chemical quality.

Finally, the main conclusions of the work are summarized in Chapter 5.

Chapter 2

Model systems

2.1 Intramolecular hydrogen bonding in acetylacetone

Pentane-2,4-dione, also known as acetylacetone (ACAC) can exist in two tautomeric forms: the keto and enol form. The tautomeric equilibrium depends on both temperature and solvent [28]. In the solution, the percentage of the enol form increases as the polarity of the solvent decreases and in the gaseous phase, the percentage of the enol form increases as the temperature decreases. The enol form is characterized by an intramolecular hydrogen bond and is known to be the most stable form in the gas phase at room temperature. It contains a donor and an acceptor oxygen atom connected by a system of conjugated double bonds (Figure 2.1). The hydrogen may transfer between these two equivalent C_s structures via the C_{2v} structure in which two C-O and C=O bonds become equal to each other, the O...O distance becomes shorter and the hydrogen atom

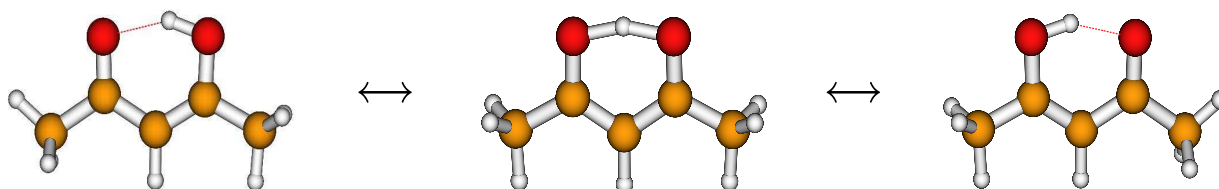


Figure 2.1: Hydrogen atom transfer in enolic acetylacetone. Left and right: two equivalent C_s structures, in the middle: C_{2v} structure. Red - oxygen, yellow - carbon, white - hydrogen atoms

lies between the two oxygens (Figure 2.1). As a prototypical enolone¹ acetylacetone has been the subject of numerous experimental [46, 47, 48, 49, 50, 51] and theoretical studies [30, 31, 32, 52]. Still, a number of issues concerning the nature of hydrogen bond in ACAC is not very well understood.

The first issue to be considered is the geometry of the lowest energy form of ACAC. The gas-phase electron diffraction experiments presented two conflicting enol structures. In the seventies a symmetric (C_{2v}) structure with symmetric, linear HB was predicted [53, 54] while more recent experiments predict an asymmetric (C_s) structure with an asymmetric bent HB [46, 47]. Surprisingly, experiments reporting symmetric structure gave very different values for the O \cdots O distance (2.381 Å [53] and 2.514 Å [54]). Experiments reporting an asymmetric structure gave the values 2.512 Å at room temperature [46] and 2.592 Å at 428.15 K [47]. On the other hand, X-ray crystallography gave a value of 2.535 Å for O \cdots O distance [48]. The last two electron diffraction studies, along with the neutron scattering in crystals [33], liquid phase NMR [49] and gas phase vibrational spectroscopy [50] are consistent with an asymmetric structure. However, a high resolution rotational spectrum of ACAC was reported confirming the symmetric C_{2v} structure as the lowest energy enolic form of ACAC [51].

Furthermore, the orientation of the methyl groups in ACAC depends sensitively on the position of the hydrogen atom. It was the work of Horsewill et al. that established the presence of two energetically inequivalent methyl groups in ACAC with hindering potentials of 180 and 590 K (equivalent to 0.35 and 1.17 kcal mol⁻¹) [27] but direct evidence of the coupling between the HAT motion and internal rotation of the two methyl groups came from inelastic neutron scattering measurements [33]. Namely, it has been shown that two methyl tunneling peaks shift upon deuteration of the non-methyl hydrogen atoms.

Experimental spectroscopic studies of the ACAC hydrogen bond date back to the investigation of the IR absorption bands associated with the chelate ring in a number of β -diketones by S. Bratož et al. in early fifties [13]. This was later continued in an IR and Raman studies of the enol form of ACAC and its deuterated analogs by S. F. Tayyari et al. [29, 50], Ogoshi et al. [28] and Chiavassa et al. [55]. In the eighties B. Cohen and S. Weiss reported the only temperature dependent IR spectra of ACAC and its deuterated analogue in the region of the C=C and C=O stretches [56].

The IR spectrum of ACAC is dominated by an extremely broadened OH-stretch band located between 1800 and 3400 cm⁻¹ with a maximum at 2800 cm⁻¹ [28, 29]. Such a broad band reflects strong anharmonic mixing between the OH-stretch and low frequency modes of ACAC [26]. Moreover, the band shape is further complicated by

¹the enol tautomers of β -diketons

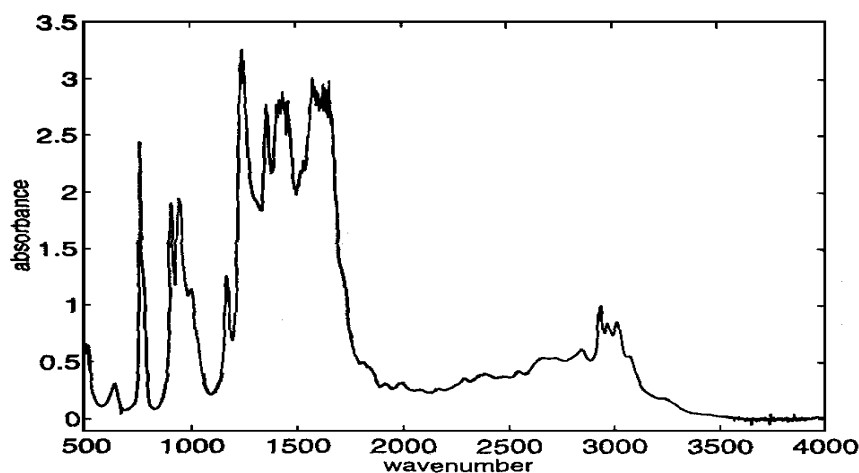


Figure 2.2: Experimental gas phase IR spectrum of ACAC. Courtesy of J. Mavri and J. Grdadolnik, *J. Phys. Chem. A*, **105** (2001) 2049.

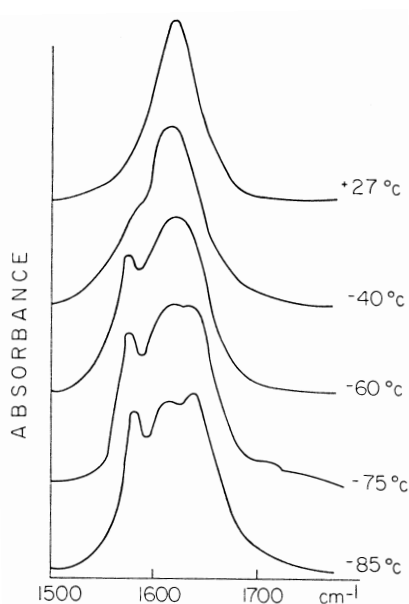


Figure 2.3: The 1500-1800 cm^{-1} region of the IR spectra of ACAC. Taken from B. Cohen and S. Weiss, *J. Phys. Chem.* **88** (1984) 3160

Fermi-type resonances [57] and Franck-Condon type vibrational progressions which are expected to arise from combination transitions involving stretching of the hydrogen bond [34, 58]. Upon deuteration of the enolic hydrogen, the O-D stretch appears as a band centered at $\sim 2000 \text{ cm}^{-1}$ with a bandwidth of $\sim 200 \text{ cm}^{-1}$.

The 1700-1000 cm^{-1} region of the spectra of ACAC displays some intriguing features. This is the region of enol ring modes, the C=O, C-O, C=C and C-C stretching and the

O-H bending. In the C=O region of the room temperature gas phase ACAC spectrum, only a single band is reported at $\sim 1620 \text{ cm}^{-1}$. However, in the work of B. Cohen and S. Weiss the low temperature IR spectrum of ACAC shows three distinct bands at $\sim 1635, 1600$ and 1575 cm^{-1} [56] (Figure 2.3). It was found that only the intensity of the middle component increases with temperature. In the spectrum of the deuterated component (nonmethyl hydrogen deuterated) only two components can be found at all temperatures. Although authors have considered hydrogen tunneling, they attributed the three-maxima structure of the band to two different forms of enol-ACAC: the ground state and a low-lying vibrationally excited state. On the other hand, Tayyari et al. explained the structure of a C=O band on the basis of the coexistence of two conformers of ACAC, exhibiting eclipsed and staggered methyl groups [29].

The region between 1500 and 1200 cm^{-1} belongs to the C-O stretching, the O-H \cdots O in plane bending and two CH₃ deformation modes. There are two bands in this region that deserve further attention. One band at $\approx 1300 \text{ cm}^{-1}$ is strong in Raman and weak in IR, and the other at 1250 cm^{-1} is weak in Raman but strong in IR. Ogoshi et al. did not consider the former in their normal mode analysis [28], but two different assignments are given by Chiavassa et al. [55] and Tayyari et al. [29]. The strong IR band at 1250 cm^{-1} is assigned by Ogoshi et al. to the C-C stretching coupled with C=C stretching mode [28]. According to Tayyari et al. on the basis of harmonic normal mode calculation, this band has a more complicate character, i.e., it consists of a symmetric C-C=C, a symmetric C-CH₃ stretch and an O-H bend [29].

In the region below 1000 cm^{-1} the most interesting bands are the bands at 945 cm^{-1} and 908 cm^{-1} corresponding to the OH out-of-plane bendings and two bands at 515 cm^{-1} and 397 cm^{-1} which are assigned to the in-plane ring deformations. The lowest frequency observed is at 230 cm^{-1} . This band is due to the stretching of the hydrogen bond.

Concerning theoretical investigations there exists the same controversy concerning the relative energies of C_{2v} and C_s structures. Early work of J. Dannenberg and R. Rios with MP2/D95** level of theory and zero-point vibrational correction placed the C_{2v} structure below the C_s structure [30]. J. Mavri and J. Grdadolnik using various levels of theory (Hartree Fock (HF), Moller-Plesset (MP2) and Density Functional theory (DFT)) placed the C_{2v} structure above the C_s structure [31]. Their best estimate of the barrier height on MP2/6-311+G(2d,2p) level of theory is $2.669 \text{ kcal mol}^{-1}$. The same authors simulated the IR spectrum of ACAC in the gas phase and in a chloroform solution by using mixed quantum-classical dynamics [32]. They have found that the simulated bands corresponding to asymmetric OH (OD) stretching match the experimental position and shape. However, they could not explain the fine structure of the bands. The importance of intramolecular coupling in acetylacetone was also discussed although the influence

of the methyl internal rotation in ACAC was not treated explicitly. A thorough *ab initio* study of the enol forms of ACAC was performed by Sliznev et al. [52]. They employed various levels of theory, Moller-Plesset perturbation theory (MP2, MP3, MP4) and the configuration interaction methods (CISD, CISD + Q) to calculate the relative stability of ACAC stationary points important for the intramolecular HAT reaction and internal methyl rotation. Yet, the geometry optimization were performed on a Hartree-Fock (HF) level of theory and it still remains to be investigated how the HF approximation affects the energetics.

Before this work, the most accurate *ab initio* harmonic vibrational frequencies have been reported together with the experimental IR and Raman spectra by Tayyari et al. [29]. An investigation beyond the harmonic approximation is however needed in order to explain the nature of the vibrational modes coupling that leads to anharmonicities in the ACAC spectrum. Also, the double well shape of the potential is expected to leave a characteristic imprint in the IR spectrum. Till now no such features were observed, but this could be due to the fact that the infrared spectrum of ACAC has been studied only at low resolution. Furthermore, none of the simulations aimed at explaining the shape and the position of the bands in the IR spectra of ACAC did take into account tunneling effects.

2.2 Intermolecular hydrogen bonding in the formic acid dimer

Double hydrogen bonded systems play a crucial role in understanding multiple HAT reactions in biological systems. For instance, they are highly relevant for understanding fundamental aspects of DNA base pair dynamics. The formic acid dimer (FAD) is the smallest molecule exhibiting multiple intermolecular hydrogen bonds, therefore it is a perfect prototype for studying multiple HAT reactions. Due to its moderate size FAD allows for highly accurate theoretical treatments. The formic acid (FA) monomers dimerize like all carboxylic acid dimers with two hydrogen bonds forming a planar eight-membered ring (Figure 2.4). The HAT is occurring between two equivalent C_{2h} global minima. During hydrogen transfer, monomers move closer together, ending in the transition state structure of D_{2h} symmetry. Most of the authors agree on a synchronous concerted mechanism of HAT [17, 59, 60]. On the other hand, the classical molecular dynamics study of H. Ushiyama and K. Takatsuka suggested an asynchronous mechanism with the time delay of 8 fs between two HA transfers [61].

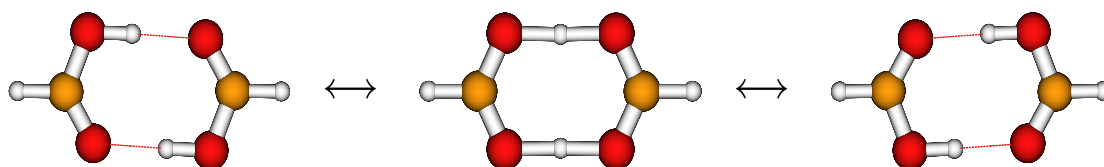


Figure 2.4: Double hydrogen atom transfer reaction in the formic acid dimer. Left and right: two equivalent minima C_{2h} structures, in the middle: D_{2h} structure. Red - oxygen, yellow - carbon, white - hydrogen atoms.

Electronic structure calculations on FAD are numerous. The computed geometries of the dimer [62, 59] are consistent with the experimental structures. Namely, the rotational constants determined in the VRT spectrum [14] indicated that the rotationally averaged structure of the minima corresponds to a C_{2h} geometry which is in agreement with previous electron diffraction experiments [63]. However, the reported barrier heights for the HAT reaction differ considerably and range between 7.8 and 11.4 kcal mol⁻¹ for MP2 calculations [59, 17, 41] and between 1.2 and 6.4 kcal mol⁻¹ for various DFT functionals [38, 62, 64]. The stabilisation energy of FAD has been calculated using more sophisticated treatments. For example, Tsuzuki et al. constructed the stabilization energy of FAD as the sum of the stabilization energy at MP2 basis set limit and a correction term

covering the higher correlation energy contributions (which was calculated as a difference between the interaction energies at the CCSD(T)/cc-pVTZ and MP2/cc-pVTZ level of theory) [64]. They obtained the value of $\Delta E = -13.54 \text{ kcal mol}^{-1}$ for the stabilization energy of FAD. On the other hand, P. Jurečka and P. Hobza in their work on the convergence of a correlation correction term reported a stabilization energy for the FAD formation of $\Delta E = -17.28 \text{ kcal mol}^{-1}$ at the CCSD(T)/cc-pVTZ level of theory [37].

The double minima shape of the potential in FAD gives rise to splittings of each rovibrational state into two states (upper (*u*) and lower (*l*) state). In 2002 F. Madeja and H. Havenith reported the first high resolution spectroscopic measurement of FAD in the gas phase with fully resolved rotational-vibrational-tunneling transitions [14]. The region of the antisymmetric C-O stretch $1241.7 - 1250.7 \text{ cm}^{-1}$ was recorded and analyzed for $(\text{DCOOH})_2$. The simultaneous observation of *a*-type transitions ($(u) \leftarrow (u)$ and $(l) \leftarrow (l)$) and *b*-type transitions ($(l) \leftarrow (u)$ and $(u) \leftarrow (l)$) in the C-O stretch region allowed the determination of the ground state tunneling splitting as $0.00286(25) \text{ cm}^{-1}$ (DE_g in Figure 2.5) and the splitting in the vibrationally excited state as $0.00999(21) \text{ cm}^{-1}$ (DE_e in Figure 2.5). This would correspond to the HAT times of 5.8 and 1.7 ns, respectively. This implies that the HA transfer is accelerated upon the vibrational excitation of the antisymmetric C-O stretching mode. However, due to a lack of precise intensity measurements for the weaker *a*-type transitions, the authors allowed for an alternative assignment. In this case the transition $(u) \leftarrow (u)$ has to be switched to $(l) \leftarrow (l)$ and *vice*

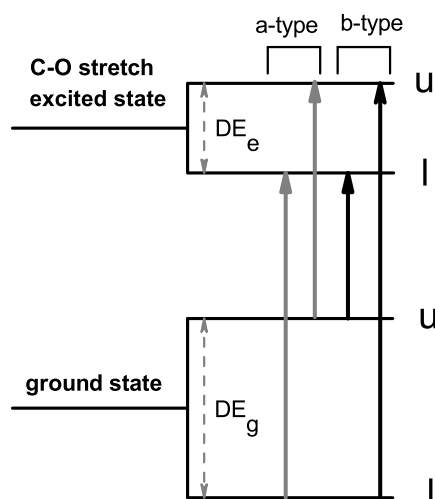


Figure 2.5: Sketch of *a*-type and *b*-type transitions observed in the formic acid dimer VRT spectrum [45].

versa (Figure 2.5) and this would give the following tunneling splittings: the ground state 0.0125 cm^{-1} and excited state $0.0031(3)\text{ cm}^{-1}$. In other words, the C-O stretching mode is a mode which suppress the tunneling. This ambiguity nicely exemplifies the complexity of the multidimensional tunneling and embraces a number of interesting questions which yet have to be answered. One of them being the question whether the vibrational excitation suppresses or promotes the tunneling. Very recent investigation of $(\text{HCOOH})_2$ in the region of the antisymmetric CO stretch vibration by M. Ortlieb and M. Havenith allowed for an unambiguous determination of a ground state tunneling splitting of $0.0158(4)\text{ cm}^{-1}$ together with the vibrationally excited state splitting of $0.0100(3)\text{ cm}^{-1}$ [45]. The ground state splitting of $0.0158(4)\text{ cm}^{-1}$ in $(\text{HCOOH})_2$ is in close agreement with the value of $0.0123(3)\text{ cm}^{-1}$ for $(\text{DCOOH})_2$ strongly supporting the alternative assignment for $(\text{DCOOH})_2$ as well.

There has been a great number of theoretical attempts to predict the ground state tunneling splitting in FAD using various dynamical models and various levels of theory. The first estimate of 0.3 cm^{-1} was given in 1987 by Chang et al. [36]. In 1991 N. Shida et al. on the basis of a three-dimensional reaction surface model and using MPCF (modified couple pair functionals) predicted a ground state tunneling splitting of 0.004 cm^{-1} [17]. Further, a three dimensional reduced dimensionality model was applied on FAD by Vener et al. focusing on the effect of the tunneling on the OH-stretch region of the spectra [41]. This study obtained a ground state splitting of 0.3 cm^{-1} and predicted a $\sim 300\text{ cm}^{-1}$ splitting of the symmetric OH-stretch as well as a $\sim 70\text{ cm}^{-1}$ splitting in the antisymmetric (IR-active) OH-stretch. The original assignment of F. Madeja and H. Havenith was recently supported by a systematic study of reduced dimensionality models by D. Luckhaus [18]. The ground state tunneling splitting of 0.0013 cm^{-1} was obtained based on the B3LYP/6-31+G* five dimensional surface with a barrier height of 2930 cm^{-1} . However, this model as all previous did not include the C-O stretching vibration. Additionally, Tautermann et al. [38] used their approximate version of instanton theory, based on the Wentzel-Kramers-Brillouin (WKB) theory [65] and reported the ground state splitting of 0.0021 cm^{-1} . The calculation was based on an approximate tunneling path between the two minima structures generated as a linear combination of the minimum energy path (MEP) and the large curvature tunneling (LCT) path (the straight line short cut between the minima). In spite of the moderate B3LYP/6-31+G(d) level of theory used to calculate the tunneling path, the reported value agrees remarkably well with the experimental result of $0.00286(25)\text{ cm}^{-1}$. Finally, the ground state tunneling splitting of 0.0038 cm^{-1} was obtained by full-dimensional numerically exact instanton theory by G. V. Mil'nikov et al. [42]. The instanton trajectory was found on a B3LYP/6-311++G(3df,3pd) potential accounting for the CCSD(T) energy correction

which gave the effective potential barrier of 2837 cm^{-1} . Due to the fact that the calculation of the splitting in the vibrationally excited states still represents serious challenge for the theory, besides this work there has been only one theoretical work that reported the splitting in the C-O stretching mode. Z. Smedarchina et al. in their dynamic calculations based on instanton techniques obtained the ground state splitting of 0.0147 cm^{-1} and a C-O excited state splitting of 0.004 cm^{-1} for $(\text{DCOOH})_2$ and 0.0149 cm^{-1} and 0.0031 cm^{-1} for $(\text{HCOOH})_2$, respectively [43, 44]. These calculations were performed on a potential evaluated at MCG3//MCQCISD/3 level. That was the first work which supported the alternative assignment of F. Madeja and M. Havenith. However, their simulation was based on approximate instanton theory whose validity in treating the vibrationally excited states is questionable. For instance, the work of G. V. Mil'nikov et al. has shown that in the case of FAD the semiclassical instanton solution for the excitations above 1000 cm^{-1} is unstable, indicating the breakdown of the theory [42].

Chapter 3

Fundamentals of vibrational spectroscopy

3.1 Vibration rotation tunneling spectroscopy

High resolution vibration rotation tunneling (VRT) spectroscopy can fully resolve each ro-vibrational transition in the molecule and can thereby provide the values for the hydrogen atom tunneling induced splittings in the ground and vibrationally excited states of IR active transitions. However, due to the high density of fully resolved rotational-vibrational-tunneling transitions, often no definite assignment is possible [14]. In order to understand experimental VRT spectra this section focuses on some basic issues concerning symmetry and selection rules used in the VRT assignment. As an example the VRT spectra of FAD is used which will in the same time allow for a better insight into the experimental results reported by F. Madeja and M. Havenith [14] and M. Ortlieb and M. Havenith [45].

The minimum energy structure of the FAD has C_{2h} symmetry. At the transition state the structure changes to D_{2h} symmetry. The usual decomposition of the $3N - 6$ vibrational modes in FAD would lead to either $9 A_g \oplus 4 A_u \oplus 3 B_g \oplus 8 B_u$ for the C_{2h} structure or $5 A_g \oplus 4 B_{3g} \oplus 1 A_u \oplus 3 B_{3u} \oplus 2 B_{2g} \oplus 1 B_{1g} \oplus 4 B_{2u} \oplus 4 B_{1u}$ for the D_{2h} one. To describe the symmetry of the system in the case of hydrogen atom transfer between two equivalent molecular structures via the transition state of different symmetry (Figure 2.4) the notion of *permutation inversion groups* are used. If a synchronous hydrogen atom transfer in FAD is assumed the molecular symmetry group is the permutation-inversion group G_8 which is isomorphic to D_{2h} . The use of the permutation inversion group G_8 avoids the dilemma posed by considering the limiting C_{2h} and D_{2h} structures of FAD. In general, the elements of permutation inversion group include:

- identity operation, labelled as E .
- permutation of equivalent nuclei. There are two kind of permutations. Permutations labelled as (12), (23) or (13) are called transpositions or interchanges while the permutations labelled (123) or (132) are called cycles. If the coordinates of the nuclei 1 and 2 are initially given by (x_1, y_1, z_1) and (x_2, y_2, z_2) after applying the operation of permuting nuclei 1 and 2 they become (x_2, y_2, z_2) and (x_1, y_1, z_1) or

$$(12)[x_1, y_1, z_1, x_2, y_2, z_2, \dots] = [x_2, y_2, z_2, x_1, y_1, z_1, \dots]$$

The cycle permutation denoted as $(abc \dots d)$ is a permutation operation that replaces a by b , b by c , \dots , d by a etc.

$$(123)[x_1, y_1, z_1, x_2, y_2, z_2, x_3, y_3, z_3 \dots] = [x_2, y_2, z_2, x_3, y_3, z_3, x_1, y_1, z_1 \dots]$$

- inversion operation, E^* changes the sign of the Cartesian coordinates of all the particles in the molecule:

$$E^*[x_i, y_i, z_i] = [-x_i, -y_i, -z_i]$$

- permutation operations combined with inversion. For instance, effect of $(12)^*$ operation on a Cartesian coordinates of the nuclei is given as

$$(12)^*[x_1, y_1, z_1, x_2, y_2, z_2, x_3, y_3, z_3 \dots] = [-x_2, -y_2, -z_2, -x_1, -y_1, -z_1, -x_3, -y_3, -z_3 \dots]$$

Adopting the nuclear labels shown in Fig. 3.1 the elements of the group G_8 for FAD would be: the identity element E , permutation of equivalent nuclei through the molecular center of mass E^* , permutation of equivalent nuclei about the a axes $P:(910)(64)(35)$,

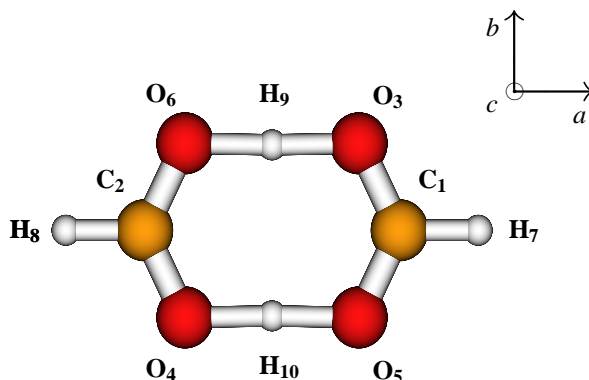


Figure 3.1: Principal inertial axes of the FAD D_{2h} structure.

Table 3.1: Character table of G_8 and the isomorphic group D_{2h} . The symmetry elements are: E , P :(910)(64)(35), P_2 : (910)(87)(21)(65)(43), PP_2 : (87)(12)(63)(45), E^* , P_2^* , P^* and PP_2^*

G_8	(D_{2h})	E	P_2	P	PP_2	E^*	P_2^*	P^*	PP_2^*
A_1'	(A_g)	1	1	1	1	1	1	1	1
A_1''	(B_{3g})	1	1	-1	-1	1	1	-1	-1
A_2'	(A_u)	1	1	1	1	-1	-1	-1	-1
A_2''	(B_{3u})	1	1	-1	-1	-1	-1	1	1
B_1'	(B_{2g})	1	-1	-1	1	-1	1	1	-1
B_1''	(B_{1g})	1	-1	1	-1	-1	1	-1	1
B_2'	(B_{2u})	1	-1	-1	1	1	-1	-1	1
B_2''	(B_{1u})	1	-1	1	-1	1	-1	1	-1

Table 3.2: Character table of C_{2h} group. The symmetry elements are: E , C_{2c} (P_2 : (910)(87)(21)(65)(43)), σ_{ab} (E^*) and i (P_2^*). The corresponding elements of D_{2h} group are given in brackets.

C_{2h}	E	C_{2c}	σ_{ab}	i
	E	P_2	E^*	P_2^*
A_g	1	1	1	1
A_u	1	1	-1	-1
B_g	1	-1	-1	1
B_u	1	-1	1	-1

Table 3.3: Correlation between C_{2h} and G_8 group

C_{2h}	G_8	D_{2h}
A_g	$A_1' \oplus A_1''$	$A_g \oplus B_{3g}$
A_u	$A_2' \oplus A_2''$	$A_u \oplus B_{3u}$
B_g	$B_1' \oplus B_1''$	$B_{2g} \oplus B_{1g}$
B_u	$B_2' \oplus B_2''$	$B_{2u} \oplus B_{1u}$

permutation of equivalent nuclei about the c axes P_2 : (910)(87)(21)(65)(43), permutation of equivalent nuclei about b axes PP_2 : (87)(12)(63)(45) and the permutation-inversion, P_2^* , P^* and PP_2^* . The character table of G_8 is given in Table 3.1. The formal decomposition of the vibrational modes of FAD in G_8 would be $5 A'_1 \oplus 3 A''_1 \oplus 1 A'_2 \oplus 3 A''_2 \oplus 2 B'_1 \oplus 1 B''_1 \oplus 4 B'_2 \oplus 4 B''_2 \oplus A''_1$ (tunneling coordinate) and this is identical to the previous D_{2h} decomposition (Table 3.1).

For understanding the symmetry of the vibrational levels split due to tunneling the definition of the correlation between the group and its subgroups is introduced. The correlation rule shows how the irreducible representations of a group (\mathbf{G}) correlates to these of the subgroup (\mathbf{A} and \mathbf{B}) where

$$\mathbf{G} = \mathbf{A} \otimes \mathbf{B}$$

If the energy levels of the molecule are labelled according to the irreducible representations of a subgroup (\mathbf{A}) then the symmetry labels using the irreducible representations of a group (\mathbf{G}) can be deduced if the correlation of the irreducible representations of a group (\mathbf{G}) to those of a subgroup (\mathbf{A}) is known¹. In the case of FAD, 309 lines in the frequency range from 1221.0 to 1226.7 cm^{-1} corresponding to the C-O antisymmetric stretch vibration has been assigned [45]. The C-O antisymmetric stretch corresponds to the B_u irreducible representation of the C_{2h} group. This is schematically represented on the right side in Figure 3.2. The ground state is labelled as A_g and excited vibrational state as a B_u state. Due to the HA transfer reaction each of these two levels split into two levels whose symmetry is labelled according to the correlation of the irreducible representations of a $D_{2h}(G_8)$ group to those of C_{2h} subgroup (Table 3.3). Accordingly, B_u level splits into two levels with symmetry corresponding to the irreducible representations of the D_{2h} group as B_{1u} and B_{2u} and the A_g level splits into A_g and B_{3g} levels. This means, that if there would be no rotation, the fundamental transition corresponding to the C-O antisymmetric excitation would split into four components corresponding to the $B_{1u} \leftarrow A_g$, $B_{2u} \leftarrow A_g$, $B_{1u} \leftarrow B_{3g}$ and $B_{2u} \leftarrow B_{3g}$ transitions.

For each vibrational level one has also to consider the rotational levels. As FAD is an asymmetric rotor, the rotational levels are described by their quantum numbers K_a and K_c . In Figure 3.2 the rotational levels described by the quantum numbers $K_a = 0$ and

¹Consider that the group \mathbf{G} of order g has elements $\{G_1, G_2, \dots, G_g\}$ and its subgroup \mathbf{A} of order $a < g$ has elements $\{A_1, A_2, \dots, A_a\}$. Also, suppose that $A_1 = G_1, A_2 = G_2, \dots, A_a = G_a$. Any irreducible matrix representation of \mathbf{G} will provide the matrix representation of \mathbf{A} by considering only the matrices corresponding the elements G_1, G_2, \dots, G_a of \mathbf{G} . For instance, to determine the correlation table of the G_8 (D_{2h}) group with the C_{2h} group one has to consider only the elements E, P_2, E^* and P_2^* (see Table 3.2). The representations A'_1 and A''_1 have characters 1 under each of this four operations and hence correlate with the representation A_g of C_{2h} . The representations A'_2 and A''_2 have characters 1 under operations E and P_2 and -1 under operations E^* and P_2^* and hence correlate with the representation A_u of C_{2h} etc.

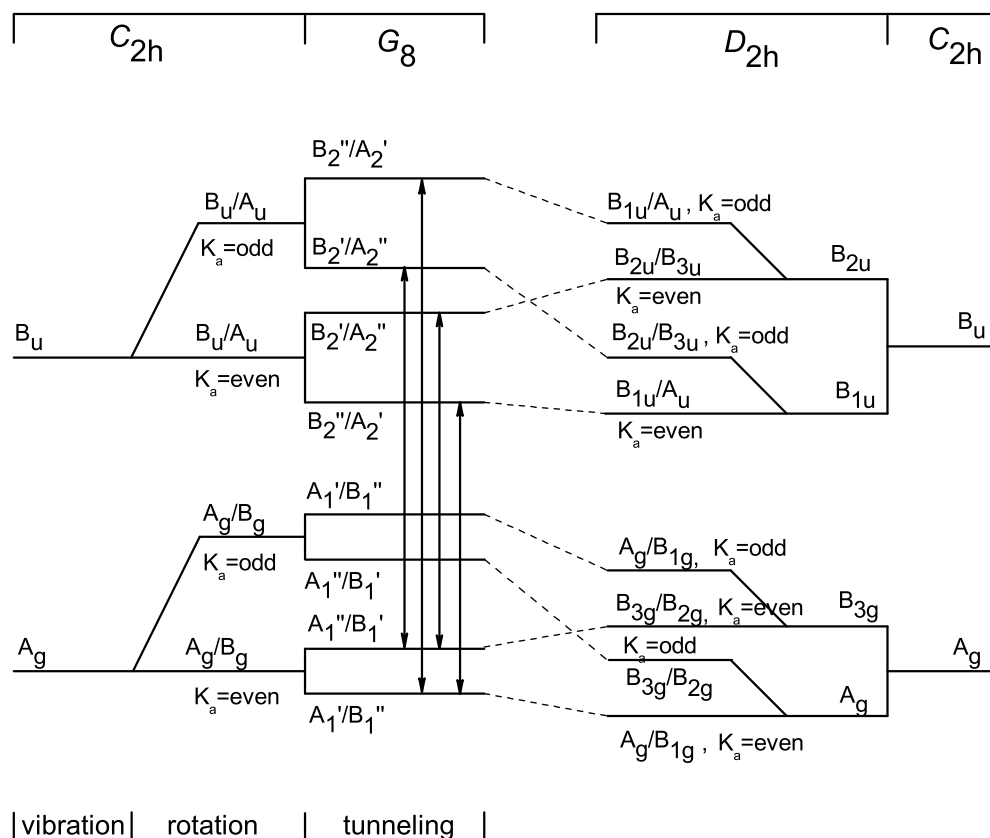


Figure 3.2: Energy scheme for the vibrational rotational tunneling states of FAD in D_{2h} and G_8 symmetry.

$K_a = 1$ for each of the four vibrational levels are shown in the middle of the scheme. In the middle of the right side of the scheme the *overall* symmetry of the levels is denoted according to the D_{2h} group i.e. as A_g/B_{1g} , B_{3g}/B_{2g} etc. The overall symmetry of each level in the symmetry group D_{2h} is a product of the vibrational, rotational and tunneling symmetry.

The symmetry of the rotational state depends on the evenness or oddness of K_a and K_c (which is in the scheme 3.2 denoted as A_g/B_{1g}). The symmetry of the rotational levels in the case of a D_{2h} group are presented in Table 3.4². For instance, for the vibrational state with the B_{1u} symmetry two rotational levels are shown: one for $K_a = 0$ and the other for $K_a = 1$. In the case when $K_a = 0$ (K_a even) and K_c even then the rotational

²For the asymmetric top one can use the asymmetric top symmetry rule which states that the *ee* function will transform as the totally symmetric representation. The *eo* function as the representation having +1 for R_a^π (and -1 for R_b^π and R_c^π), the *oe* function as the representation having +1 for R_c^π (and -1 for R_a^π and R_b^π), and the *oo* function as the representation having +1 under R_b^π (and -1 for R_a^π and R_c^π). R_a^π corresponds to the rotation of the asymmetric top molecule through π radians about the *a* axes and in the case of the D_{2h} symmetry group it corresponds to the C_{2a} element. These correlations are usually given in the character table of the group.

Table 3.4: Symmetry of the $J_{K_a K_c}$ rotational levels of the D_{2h} group

$K_a K_c$	$\Gamma_{rot}(D_{2h})$
ee	A_g
eo	B_{1g}
oe	B_{3g}
oo	B_{2g}

Table 3.5: Symmetry of the $J_{K_a K_c}$ rotational levels of the C_{2h} group

$K_a K_c$	$\Gamma_{rot}(C_{2h})$
ee	A_g
eo	B_g
oe	A_g
oo	B_g

state should have an A_g symmetry (Table 3.4). As a vibrational state is of B_{1u} symmetry the overall symmetry of the level is $A_g \times B_{1u} = B_{1u}$. In the case when $K_a = 0$ (K_a even) and K_c odd then the rotational state should have a B_{1g} symmetry. As this rotational state corresponds again to the vibrational state of B_{1u} symmetry, overall symmetry of the state is $B_{1g} \times B_{1u} = A_u$. This is denoted as a B_{1u}/A_u (ee/eo) state. The same can be done for a $K_a = 1$ (K_a odd) and K_c even (oe) level, the overall symmetry of the state is $B_{2u} = B_{3g} \times B_{1u}$ or K_a odd and K_c odd (oo), the overall symmetry is $B_{3u} = B_{2g} \times B_{1u}$. The same procedure can be used to explain the symmetry of the states by using the C_{2h} group on the left side of the Figure 3.2. Starting from the left the symmetry of the vibrational states is given (A_g and B_u). In the middle, the symmetry of rovibrational states is labeled (for the symmetry of rotational states see Table 3.5). And then the splittings of rovibrational states due to the tunneling is included. The symmetry of the states is denoted according to the correlation table between the C_{2h} and G_8 group (Table 3.3).

The electric dipole moment in FAD has a A'_2 symmetry which implies that the $A'_1 \leftrightarrow A'_2$, $A''_1 \leftrightarrow A''_2$, $B'_1 \leftrightarrow B'_2$ and $B''_1 \leftrightarrow B''_2$ transitions are allowed because the products $A'_1 \times A'_2 \times A'_2$, $A''_1 \times A''_2 \times A''_2$, $B'_1 \times A'_2 \times B'_2$ and $B''_1 \times A'_2 \times B''_2$ give totally symmetric irreducible representation of D_{2h} group. These selection rules imply that for FAD the HA transfer tunneling splittings in the ground and vibrationally excited states can be determined by measuring two types of transitions: a type ($\Delta K_a = 0$) and b type ($\Delta K_a = 1$) transitions. For b type transitions the selection rules require a change of the tunneling state upon the vibrational excitation: the vibrational transition will go from the lower tunneling component (l) to the upper tunneling component (u) or vice versa. For a type transitions

tunneling state changes from (*u*) to (*u*) or (*l*) to (*l*). By measuring both *a* and *b* type transitions the sum and the difference of the tunneling splittings in the vibrational ground and excited state can be obtained as shown in Figure 2.5. However, it is very difficult to further decide which level shows larger splitting. For instance, in Figure 3.2 for the excited vibrational state and K_a even the upper tunneling state denoted as B'_2/A''_2 lies above the lower tunneling state denoted as B''_2/A'_2 . But the symmetry notation doesn't have to imply the energy ordering. In the case when the energy differences between the two tunneling states are small, a coupling to the nearby state of the same symmetry can switch the energy ordering. This also reverses the assignment of splittings in the ground and excited vibrational state [14, 45].

3.2 Small amplitude treatment

As this thesis is concerned with the vibrational spectroscopy of hydrogen bonded systems and specifically with the choice of the proper coordinates for the treatment of large amplitude motion, this section compiles some basic notion of molecular vibrations. The validity of the Born-Oppenheimer approximation is assumed and hereafter the focus will be on different forms of the vibrational Hamiltonian describing the nuclear motion.

3.2.1 Normal coordinates

Let X, Y, Z define the space fixed axis system (Figure 3.3). The position O denotes the center of mass of the molecule in the (X, Y, Z) axis system and is given by vector \mathbf{R} . The position of an i th particle in the (x, y, z) axis system is given by the vector \mathbf{r}_i , while its equilibrium position is given by \mathbf{r}_i^0 . The displacement vector $\boldsymbol{\rho}_i$ is defined as

$$\boldsymbol{\rho}_i = \mathbf{r}_i - \mathbf{r}_i^0$$

with the components $\Delta x_i = x_i - x_i^0$, $\Delta y_i = y_i - y_i^0$ and $\Delta z_i = z_i - z_i^0$. The total velocity of the i th particle in space is then

$$\mathbf{V}_i = \dot{\mathbf{R}} + \boldsymbol{\omega} \times \mathbf{r}_i + \mathbf{v}_i$$

where $\boldsymbol{\omega}$ is the angular velocity of the rotating coordinate system and the vector \mathbf{v}_i has components \dot{x}_i , \dot{y}_i and \dot{z}_i . The kinetic energy of the whole molecule is:

$$\begin{aligned} 2T &= \sum_i m_i (\dot{\mathbf{R}} + \boldsymbol{\omega} \times \mathbf{r}_i + \mathbf{v}_i)^2 \\ &= \dot{\mathbf{R}}^2 \sum_i m_i + \sum_i m_i (\boldsymbol{\omega} \times \mathbf{r}_i) \cdot (\boldsymbol{\omega} \times \mathbf{r}_i) + \sum_i m_i \mathbf{v}_i^2 \\ &\quad + 2\dot{\mathbf{R}} \cdot \boldsymbol{\omega} \times \sum_i m_i \mathbf{r}_i + 2\dot{\mathbf{R}} \cdot \sum_i m_i \mathbf{v}_i + 2\boldsymbol{\omega} \cdot \sum_i m_i (\mathbf{r}_i \times \mathbf{v}_i) \end{aligned} \quad (3.1)$$

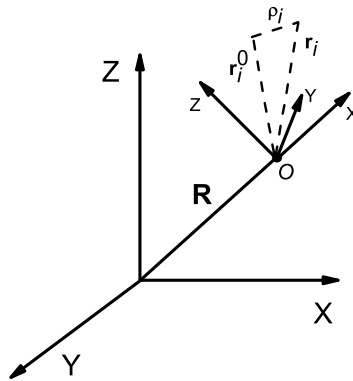


Figure 3.3: Space fixed (XYZ) axes (laboratory coordinate system) and the molecule fixed (xyz) axes (rotating coordinate system).

Since the O is the center of mass of the whole molecule, at every instant it must be

$$\sum_i m_i \mathbf{r}_i = 0 \quad (3.2)$$

It follows then that also

$$\sum_i m_i \mathbf{v}_i = 0$$

must be satisfied³. By replacing \mathbf{r}_i with $\boldsymbol{\rho}_i + \mathbf{r}_i^0$ Eq. (3.1) becomes

$$\begin{aligned} 2T = & \mathbf{R}^2 \sum_i m_i + \sum_i m_i (\boldsymbol{\omega} \times \mathbf{r}_i) \cdot (\boldsymbol{\omega} \times \mathbf{r}_i) + \sum_i m_i \mathbf{v}_i^2 \\ & + 2\boldsymbol{\omega} \cdot \sum_i m_i (\boldsymbol{\rho}_i \times \mathbf{v}_i) + 2\boldsymbol{\omega} \cdot \sum_i m_i (\mathbf{r}_i^0 \times \mathbf{v}_i) \end{aligned} \quad (3.3)$$

The first term in Eq. (3.3) is the translational energy of the molecule, the second is the rotational energy, the third the vibrational energy and the fourth and fifth represent the coupling between rotation and vibration. However, for every displacement $\boldsymbol{\rho}_i$ in a molecular vibration, the molecule fixed axes (x, y, z) can be rotated to a new system of axes (x', y', z') in order to satisfy the equations (for details see the Appendix A)

$$\sum_i m_i \mathbf{r}_i^0 \times \mathbf{v}_i = 0 \quad (3.4)$$

In this case, the fifth term in Eq. (3.3) vanishes. The remaining fourth term, called the *Coriolis energy*, ($2\boldsymbol{\omega} \cdot \sum_i m_i (\boldsymbol{\rho}_i \times \mathbf{v}_i)$) can be neglected since it small compared to the pure vibrational term. The Coriolis energy term depends both on the displacement coordinates and the angular velocity which are small compared to the vibrational velocity. Usually, Eq. (3.4) is modified and the condition

$$\sum_i m_i \mathbf{r}_i^0 \times \mathbf{r}_i = 0 \quad (3.5)$$

is used since the condition (3.5) implies the condition (3.4)⁴. The three components of the last equation are

$$\sum_i m_i (x_i^0 y_i - y_i^0 x_i) = 0$$

³If $\sum_i m_i \mathbf{r}_i = 0$, then $\sum_i m_i \dot{\mathbf{r}}_i = \sum_i m_i [(\boldsymbol{\omega} \times \mathbf{r}_i + \mathbf{v}_i)] = \boldsymbol{\omega} \times \sum_i m_i \mathbf{r}_i + \sum_i m_i \mathbf{v}_i = \sum_i m_i \mathbf{v}_i = 0$

⁴On differentiating (3.5) it follows

$$\begin{aligned} 0 &= \sum_i m_i \dot{\mathbf{r}}_i^0 \times \mathbf{r}_i + \sum_i m_i \mathbf{r}_i^0 \times \dot{\mathbf{r}}_i \\ &= \sum_i m_i (\boldsymbol{\omega} \times \mathbf{r}_i^0) \times \mathbf{r}_i + \sum_i m_i \mathbf{r}_i^0 \times (\boldsymbol{\omega} \times \mathbf{r}_i) + \sum_i m_i \mathbf{r}_i^0 \times \mathbf{v}_i \\ &= \sum_i m_i \mathbf{r}_i^0 \times \mathbf{v}_i \end{aligned}$$

$$\begin{aligned}\sum_i m_i (y_i^0 z_i - z_i^0 y_i) &= 0 \\ \sum_i m_i (z_i^0 x_i - x_i^0 z_i) &= 0\end{aligned}$$

and represent the so called Eckart conditions [66].

Introduction of normal coordinates

At this stage a new set of coordinates $X_1, \dots, X_{3N_{\text{at}}}$, known as *mass-weighted coordinates* is introduced to replace the coordinates $\rho_i(\Delta x_i, \Delta y_i, \Delta z_i)$:

$$X_1 = \sqrt{m_1} \Delta x_1, \quad X_2 = \sqrt{m_1} \Delta y_1, \quad X_3 = \sqrt{m_1} \Delta z_1, \quad X_4 = \sqrt{m_2} \Delta x_2, \quad \text{etc.}$$

The classical kinetic energy in these coordinates is:

$$2T = \sum_{i=1}^{3N_{\text{at}}} \dot{X}_i^2 \quad (3.6)$$

For small displacements the potential energy V may be expressed as a Taylor expansion in the displacement of X_i :

$$\begin{aligned}2V &= 2V_0 + 2 \sum_{i=1}^{3N_{\text{at}}} \left(\frac{\partial V}{\partial X_i} \right)_0 X_i + \sum_{i,j=1}^{3N_{\text{at}}} \left(\frac{\partial^2 V}{\partial X_i \partial X_j} \right)_0 X_i X_j + \text{higher terms} \\ &= 2V_0 + 2 \sum_{i=1}^{3N_{\text{at}}} K_i X_i + \sum_{i,j=1}^{3N_{\text{at}}} K_{ij} X_i X_j + \text{higher terms}\end{aligned} \quad (3.7)$$

The zero of energy can be chosen in such a way that the energy of the equilibrium geometry is zero ($V_0 = 0$). Moreover, as the equilibrium geometry represents a stationary point on a potential energy surface, the first derivative of the potential is also zero i.e. $K_i = 0$. For *small amplitudes of vibration* the higher terms in the expansion can be neglected and the potential is expressed as:

$$2V = \sum_{i,j=1}^{3N_{\text{at}}} K_{ij} X_i X_j \quad (3.8)$$

The $3N_{\text{at}} \times 3N_{\text{at}}$ matrix \mathbf{K} whose elements are denoted as K_{ij} is called the force constant matrix or the Hessian matrix. Newton's equations of motion⁵ for a vibrating molecule can now be written as

$$\ddot{X}_j + \sum_{i=1}^{3N_{\text{at}}} K_{ij} X_i = 0, \quad j = 1, \dots, 3N_{\text{at}} \quad (3.9)$$

⁵Newton's equations of motion in Lagrangian form are:

$$\frac{\partial}{\partial t} \frac{\partial T}{\partial \dot{X}_j} + \frac{\partial V}{\partial X_j} = 0 \quad j = 1, \dots, 3N_{\text{at}}$$

This represents a set of $3N_{\text{at}}$ simultaneous second-order linear differential equations whose solutions can be written as

$$X_i = l_i \cos(\sqrt{\lambda}t + \phi) \quad (3.10)$$

where l_i represents the amplitude of the vibrational motion, $\sqrt{\lambda}$ is its frequency and ϕ is the phase. If the expression (3.10) is substituted into Eq. (3.9), a set of simultaneous linear algebraic equations is obtained:

$$\sum_{i=1}^{3N_{\text{at}}} (K_{ij} - \delta_{ij}\lambda)l_i = 0 \quad j = 1, \dots, 3N_{\text{at}} \quad (3.11)$$

in which δ_{ij} is the Kronecker delta symbol that equals unity if $i = j$, and is zero otherwise. In general, there are $3N_{\text{at}}$ values λ_k that satisfy the $3N_{\text{at}}$ simultaneous equations (3.11) and there are $3N_{\text{at}}$ corresponding vectors l_{ki} . The set of equations (3.11) have a solution only if the determinant of the coefficients is zero. This determinant is just $|\mathbf{K} - \lambda\mathbf{1}|$ and the values λ_k and l_{ki} may be found from the solution of the *secular equation*

$$|K_{ij} - \delta_{ij}\lambda| = 0 \quad (3.12)$$

In fact, the λ_k represent the eigenvalues and l_{ki} represent the eigenvectors of the eigenvalue equation:

$$\mathbf{K}\mathbf{l} = \lambda\mathbf{l} \quad (3.13)$$

where the matrix \mathbf{K} is the force constant matrix whose elements K_{ij} are defined in Eq. (3.7). The quantities L_{ki} derived from the values l_{ki} as

$$L_{ki} = \frac{l_{ki}}{\left[\sum_i^{3N_{\text{at}}} (l_{ki})^2 \right]^{1/2}} \quad (3.14)$$

define a new set of coordinates Q_k , $k = 1, 2, \dots, 3N_{\text{at}}$ called the *normal coordinates*⁶

$$Q_k = \sum_i^{3N_{\text{at}}} L_{ki} X_i \quad k = 1, 2, \dots, 3N_{\text{at}} \quad (3.15)$$

In the output of quantum chemistry programs (Gaussian [67] and Gamess [68]) normal coordinates are defined as displacements along the non-mass weighted Cartesian coordinates using the quantities L'_{ki}

$$L'_{ki} = \frac{l_{ki} m_i^{-1/2}}{\left[\sum_i^{3N_{\text{at}}} (l_{ki} m_i^{-1/2})^2 \right]^{1/2}} \quad (3.16)$$

⁶note the orthogonality $\sum_i L_{ki} L_{li} = \delta_{kl}$

where the square of the normalization factor in the denominator is given as a reduced mass μ_k for the vibrational mode Q_k .

When the secular equation (3.12) is solved for a stationary point, six values of λ should be exactly zero for a nonlinear molecule, corresponding to the translational and rotational modes. In real calculations using quantum chemistry packages, these modes are never exactly zero but very close to zero (rotational modes even have frequencies as large as $10\text{-}50\text{ cm}^{-1}$) due to the fact that the geometry cannot be optimized to a gradient of exactly zero. In quantum chemical packages like Gaussian [67] the geometry optimization is considered converged if the root mean square (RMS) gradient is less than $\approx 10^{-4} - 10^{-5}$ a.u. (the later corresponding to tight option) corresponding to the energy being converged to $\approx 10^{-6}$ a.u. The residual gradient shows up as frequencies for the rotation of the above magnitude.

However, if a system posses real vibrational frequencies of the same magnitude as the residual rotational frequencies, mixing can occur and result in inaccurate values for the true vibrations. It is thus necessary to project the directions corresponding to infinitesimal rotations and translations from the force constant matrix \mathbf{K} by using the projector \mathcal{P} [69, 70]. The projector \mathcal{P} is a $3N_{\text{at}} \times 3N_{\text{at}}$ matrix defined as⁷

$$\mathcal{P}_{i\gamma, i'\gamma'} = \sqrt{\frac{m_i m_{i'}}{M^2}} \delta_{\gamma\gamma'} + \sum_{\alpha\beta\alpha'\beta'} \epsilon_{\alpha\beta\gamma} X_{i\beta} [I^{-1}]_{\alpha\alpha'} \epsilon_{\alpha'\beta'\gamma'} X_{i'\beta'} \quad (3.18)$$

where $\mathbf{X} \equiv \{X_{i\gamma}\}$ represents a $3N_{\text{at}}$ dimensional vector, a mass weighted geometry on a potential energy surface, and the 3×3 matrix \mathbf{I} is the moments of inertia tensor at the corresponding point on the surface. It is defined as

$$I_{\beta\gamma} = \sum_i \left[\left(\sum_{\alpha} X_{i\alpha}^2 \right) \delta_{\beta\gamma} - X_{i\beta} X_{i\gamma} \right] \quad (3.19)$$

Note also that here composite indexes $i\gamma$ are used where $i = 1, \dots, N_{\text{at}}$, $\gamma = x, y, z$.

The normal modes are in this case defined by diagonalizing the projected value of the force constant matrix $\mathbf{K}^{\mathcal{P}}$

$$\mathbf{K}^{\mathcal{P}} = (\mathbf{1} - \mathcal{P}) \cdot \mathbf{K} \cdot (\mathbf{1} - \mathcal{P}) \quad (3.20)$$

Quantum chemical softwares [67, 68] normally remove translational and rotational directions from the force constant matrix before obtaining the normal modes.

⁷the definition of $\epsilon_{\alpha\beta\gamma}$

$$\epsilon_{\alpha\beta\gamma} = \begin{cases} 0 & \text{if any of two indices are equal.} \\ 1 & \text{if } \alpha, \beta, \gamma \text{ are an 'even' permutations of } 1,2,3. \\ -1 & \text{if } \alpha, \beta, \gamma \text{ are an 'odd' permutations of } 1,2,3. \end{cases} \quad (3.17)$$

The Quantum-mechanical Hamiltonian for a Molecule

The form of the quantum-mechanical ro-vibrational Hamiltonian for a molecule is deduced from the classical expression for the kinetic energy given in Eq. (3.3) after separating the kinetic energy of translation. For the derivation the reader is referred to Ref. [71]. Expressed in normal coordinates it has a general form

$$\hat{H}_n = \frac{1}{2} \sum_{\alpha\beta} (\hat{J}_\alpha - \hat{\pi}_\alpha) (I^{-1})'_{\alpha\beta} (\hat{J}_\beta - \hat{\pi}_\beta) - \frac{\hbar^2}{8} \sum_{\alpha} (I^{-1})'_{\alpha\alpha} + \frac{1}{2} \sum_k^N \hat{P}_k^2 + V(Q_1, \dots, Q_N) \quad (3.21)$$

where $\hat{\mathbf{J}} = (\hat{J}_x, \hat{J}_y, \hat{J}_z)$ is the angular momentum operator:

$$\hat{\mathbf{J}} = \frac{\hbar}{i} (\mathbf{r} \times \nabla) \quad (3.22)$$

and

$$\hat{P}_k = \frac{\hbar}{i} \left(\frac{\partial}{\partial Q_k} \right) \quad (3.23)$$

is the momentum operator conjugate to the normal coordinate Q_k . $\hat{\pi}_\alpha$ is the so called vibrational angular momentum defined as

$$\hat{\pi}_\alpha = \sum_{lk} \zeta_{lk}^\alpha Q_l \hat{P}_k \quad (3.24)$$

and ζ_{lk}^α are the Coriolis coupling constants of the form

$$\zeta_{lk}^\alpha = \sum_i \sum_{\beta\gamma} \epsilon_{\alpha\beta\gamma} L_{i\beta,l} L_{i\gamma,k} \quad (3.25)$$

Further, the quantities $\epsilon_{\alpha\beta\gamma}$ and $L_{i\beta,l}$ are defined in Eq. (3.17) and Eq. (3.14). The $(I^{-1})'$ is the inverse of the effective moments of inertia tensor I' which is, compared to the one defined in Eq. (3.19), dependent on the Coriolis coupling constants⁸.

The separation of rotational and vibrational motion

As seen previously, the Eckart conditions minimize the coupling between the rotational and vibrational motion. Hence, the separation of the ro-vibrational Hamiltonian into a pure vibrational and pure rotational Hamiltonian is possible if the Coriolis energy is neglected. To this degree of approximation, the total nuclear wave function Ψ_n , eigenfunction of the Hamiltonian (3.21) can be written as a product of a vibrational and rotational wave functions:

$$\Psi_n \cong \Psi_v \Psi_r$$

⁸The moments of inertia tensor is here given as

$$I'_{\beta\gamma} = \sum_i \left[\left(\sum_{\alpha} X_{i\alpha}^2 - \sum_{lk} (\zeta_{lk}^\alpha Q_l)^2 \right) \delta_{\beta\gamma} - \left(X_{i\beta} X_{i\gamma} - \sum_{lk} \zeta_{lk}^\beta \zeta_{lk}^\gamma Q_l^2 \right) \right]$$

The function Ψ_r is obtained as a solution of the rotational wave equation. It is a function of three Eulerian angles θ, ϕ and χ describing the orientation of the rotating coordinate system in space (Appendix A). Here, we will be interested in a special case of zero total angular momentum and will neglect the rotational-vibrational coupling. The rotational problem will not be further discussed.

The vibrational wave function Ψ_v , is obtained as a solution of the vibrational Schrödinger equation. In normal coordinates the classical kinetic energy (3.6) is retained in its original diagonal form

$$2T = \sum_i^{3N_{\text{at}}} \dot{X}_i^2 = \sum_{i,k,l} L_{ik} L_{il} \dot{Q}_k \dot{Q}_l = \sum_k \dot{Q}_k^2 \quad (3.26)$$

and the harmonic potential energy (3.8) involves no cross products⁹

$$2V = \sum_k^{3N_{\text{at}}} \lambda_k Q_k^2. \quad (3.27)$$

Consequently, the vibrational Schrödinger equation has the form

$$-\frac{\hbar^2}{2} \sum_{k=1}^N \frac{\partial^2 \Psi_v}{\partial Q_k^2} + \frac{1}{2} \sum_{k=1}^N \lambda_k Q_k^2 \Psi_v = E_v \Psi_v \quad (3.28)$$

where E_v is the vibrational energy and N is the number of vibrational modes and equals $3N_{\text{at}} - 6$ for a nonlinear and $3N_{\text{at}} - 5$ for a linear molecule. This N dimensional Schrödinger equations is separable into N equations, one for each normal coordinate. If

$$E_v = E(1) + E(2) + \dots + E(N)$$

and

$$\Psi_v = \psi(Q_1) \psi(Q_2) \dots \psi(Q_N)$$

then Eq. (3.28) is satisfied if $E(k)$ and $\psi(Q_k)$ satisfy

$$-\frac{\hbar^2}{2} \frac{\partial^2 \psi(Q_k)}{\partial Q_k^2} + \frac{1}{2} \lambda_k Q_k^2 \psi(Q_k) = E(k) \psi(Q_k) \quad (3.29)$$

Each of these equations correspond to a one-dimensional Schrödinger equation for a linear harmonic oscillator of unit mass in the normal coordinate Q_k . As the energy levels of a linear harmonic oscillator are given as $E_v = (v + \frac{1}{2})h\nu$, $v = 0, 1, 2, \dots$ the vibrational energy of the molecule is thus

$$E_v = \sum_k^N \left(v_k + \frac{1}{2} \right) h\nu_k \quad (3.30)$$

where v_k are a quantum numbers and ν_k are frequencies associated with normal modes Q_k .

⁹note the orthogonality of the transformation between the mass weighted coordinates X_i and normal coordinates Q_k : $L_{ki}^{-1} = L_{ik}$

3.2.2 Treating anharmonicity

The harmonic approximation in which all terms beyond the second order in Taylor expansion of a molecular potential are neglected is a good approximation only for a small displacements from the equilibrium. In real molecules the neglected terms, also called anharmonic terms of the form

$$\begin{aligned} \text{higher terms} &= \frac{1}{3} \sum_{i,j,k} \left(\frac{\partial^3 V}{\partial X_i \partial X_j \partial X_k} \right)_0 X_i X_j X_k + \frac{1}{12} \sum_{i,j,k,l} \left(\frac{\partial^4 V}{\partial X_i \partial X_j \partial X_k \partial X_l} \right)_0 X_i X_j X_k X_l + \text{etc} \\ &= \frac{1}{3} \sum_{i,j,k} K_{ijk} X_i X_j X_k + \frac{1}{12} \sum_{i,j,k,l} K_{ijkl} X_i X_j X_k X_l + \text{etc} \end{aligned} \quad (3.31)$$

are important, particularly for molecules with inter- or intra-molecular hydrogen bonds. For instance, the stretching mode of a X-H donor group exhibits strong anharmonicity due to coupling to low-frequency modes. Furthermore, the higher terms in Taylor expansion have strong effects on the position of the overtones and combination levels which can mix leading to Fermi resonances. Hence, treating anharmonicity represents one of the central issues of the vibrational spectroscopy of hydrogen bonded molecules.

To obtain an anharmonic vibrational spectrum for a system of interest, the vibrational Schrödinger equation of the form

$$\left[-\frac{1}{2} \sum_{k=1}^N \frac{\partial^2}{\partial Q_k^2} + V(Q_1, \dots, Q_N) \right] \Psi_v(Q_1, \dots, Q_N) = E_v \Psi_v(Q_1, \dots, Q_N) \quad (3.32)$$

with the full potential $V(Q_1, \dots, Q_N)$ has to be solved. Obtaining the full potential energy surface (i.e. Born-Oppenheimer electronic energy) of a polyatomic molecule by quantum chemistry methods represents a formidable task. The number of the quantum chemistry calculations needed to represent the potential would be of order $n^{(3N_{\text{at}}-6)}$ where n is the number of grid point on the surface per degree of freedom. Obviously, for the systems with $N_{\text{at}} > 4$ construction of the full potential becomes a demanding task. To obtain anharmonic vibrational spectra, approximative methods are used.

Presently, some of the packages for electronic structure calculation [67, 68, 72] include methods for the computation of anharmonic frequencies. They are based on the vibrational self-consistent field (VSCF) method and/or on second-order perturbation theory (PT2) [73, 74, 75, 76].

The vibrational self-consistent field method

In the basic VSCF approach nuclear wave functions are obtained in a self-consistent field approach, termed *Vibrational Self-Consistent Field* (VSCF), starting from a product nuclear wave functions:

$$\Psi_v(Q_1, \dots, Q_N) = \prod_{k=1}^N \psi_k^{(v)}(Q_k) \quad (3.33)$$

In other words, the VSCF approach is based on an approximation in which nuclear wave function $\Psi_v(Q_1, \dots, Q_N)$, solution of the vibrational Schrödinger equation of the system, is written as a product of a single-mod wave functions $\psi_k^{(v)}(Q_k)$. Inserting the last equation into the vibrational Schrödinger equation of the system (Eq. (3.32)) results in a single-mod vibrational equation of the form

$$\left[-\frac{1}{2} \frac{\partial^2}{\partial Q_k^2} + \bar{V}_k^{(v)}(Q_k) \right] \psi_k^{(v)} = \epsilon_k^{(v)} \psi_k^{(v)} \quad (3.34)$$

where the effective potential for the normal mode Q_k is given by

$$\bar{V}_k^{(v)}(Q_k) = \left\langle \prod_{l \neq k} \psi_l^{(v)}(Q_l) \left| V(Q_1, \dots, Q_N) \right| \prod_{l \neq k} \psi_l^{(v)}(Q_l) \right\rangle \quad (3.35)$$

Equations (3.33)-(3.35) for the single-mode wave functions, the energies and effective potentials are solved *self-consistently*. The total energy is given by

$$E_v = \sum_{k=1}^N \epsilon_k^{(v)} - (N-1) \left\langle \prod_{k=1}^N \psi_k^{(v)}(Q_k) \left| V(Q_1, \dots, Q_N) \right| \prod_{k=1}^N \psi_k^{(v)}(Q_k) \right\rangle \quad (3.36)$$

The greatest computational difficulty for large systems represents evaluation of the multidimensional integrals in Eq. (3.35). One possible approach to solve this issue is the pairwise mode-mode coupling approximation in which the full potential is written in the form

$$V(Q_1, \dots, Q_N) = \sum_k V_k^{\text{diag}}(Q_k) + \sum_k \sum_{l>k} V_{kl}^{\text{coup}}(Q_k, Q_l) \quad (3.37)$$

where the diagonal potential functions $V_k^{\text{diag}}(Q_k)$ represents the anharmonic potential along the normal coordinate Q_k

$$V_k^{\text{diag}}(Q_k) = V(0, \dots, Q_k, \dots, 0) \quad (3.38)$$

and the pairwise mode-mode coupling functions $V_{kl}^{\text{coup}}(Q_k, Q_l)$ are given as two-dimensional potentials

$$V_{kl}^{\text{coup}}(Q_k, Q_l) = V(0, \dots, Q_k, \dots, Q_l, \dots, 0) \quad (3.39)$$

In this case VSCF potential $\bar{V}_k^{(v)}(Q_k)$ involves only one-dimensional integrals

$$\bar{V}_k^{(v)}(Q_k) = V_k^{\text{diag}}(Q_k) + \sum_{k \neq l} \langle \psi_k(Q_k) | V_{lk}^{\text{coup}}(Q_l, Q_k) | \psi_k(Q_k) \rangle \quad (3.40)$$

which can be computed using a grid representation for the potentials. However, the pairwise mode-mode coupling approximation can fail for large systems and for more highly excited states of the system.

The extensions of the basic approach are also used in order to correct the main deficiency of the basic VSCF approach, the neglect of the correlation between different normal modes. There are several ways to introduce vibrational correction, through configuration interaction (CI)(VSCF CI or VCI method), coupled-cluster (VCC method) or through a perturbation theory termed correlation corrected self-consistent field (CC VSCF method). Although it can be computationally expensive for medium and large size molecules, the VCI in combination with the local approach has proven to be a powerful tool for a prediction of anharmonic vibrational spectra [77]. In a case of a strong couplings between the vibrations, partially separable VSCF method (PS SCF) is also used [78].

The perturbative approach

Second-order perturbation treatment of V. Barone and coworkers [74, 75, 76] implemented in the Gaussian code is used in this thesis for the investigation of the anharmonic spectra of the acetylacetone and the formic acid dimer. Within this approach the anharmonic terms in the Taylor expansion are treated as a perturbation acting on the harmonic-normal mode Hamiltonian. The vibrational energy characterized by a set of quantum numbers $\{v_i\}$ is given in the form

$$\frac{E}{hc} = \sum_i \omega_i \left(v_i + \frac{1}{2} \right) + \sum_i \sum_{j < i} \chi_{ij} \left(v_i + \frac{1}{2} \right) \left(v_j + \frac{1}{2} \right), \quad (3.41)$$

where $\omega = \lambda_i^{1/2}$ are the harmonic frequencies of the normal modes, and χ is the matrix of anharmonic constants whose diagonal and off-diagonal elements are obtained from

$$\chi_{ii} = \frac{1}{16} K_{iiii} - \frac{1}{16} \sum_j K_{iij}^2 \frac{8\omega_i^2 - 3\omega_j^2}{\omega_j(4\omega_i^2 - \omega_j^2)},$$

$$\chi_{ij} = \frac{1}{4} K_{iijj} - \frac{1}{4} \sum_k \frac{K_{iik} K_{kjj}}{\omega_j} - \frac{1}{2} \sum_j \frac{K_{ijk}^2 \omega_k (\omega_k^2 - \omega_i^2 - \omega_j^2)}{\Delta_{ijk}}$$

and

$$\Delta_{ijk} = (\omega_i + \omega_j + \omega_k)(\omega_i - \omega_j - \omega_k)(-\omega_i + \omega_j - \omega_k)(-\omega_i - \omega_j + \omega_k)$$

The symbols K_{ijk} , K_{iiii} and K_{iijj} stand for mixed third, diagonal and semidiagonal fourth derivatives of the potential energy with respect to the normal modes. The third energy derivatives K_{ijk} are calculated numerically from the finite differences of analytical force constant matrices evaluated at positive and negative displacements δQ_i of each normal mode:

$$K_{ijk} = \frac{1}{3} \left[\frac{K_{jk}(\delta Q_i) - K_{jk}(-\delta Q_i)}{2\delta Q_i} + \frac{K_{ki}(\delta Q_j) - K_{ki}(-\delta Q_j)}{2\delta Q_j} + \frac{K_{ij}(\delta Q_k) - K_{ij}(-\delta Q_k)}{2\delta Q_k} \right]$$

The numerical calculation of fourth derivatives K_{ijkl} , requires, in principle, simultaneous displacements along two normal coordinates, which is computationally quite expensive. However, displacements of a single normal mode at a time are sufficient to evaluate terms with at most three distinct indices, which include all the derivatives required to compute vibrational energies using the second order perturbation theory (PT2)

$$K_{ijkk} = \frac{K_{ij}(\delta Q_k) + K_{ij}(-\delta Q_k) - 2K_{ij}(Q_0)}{\delta Q_k^2}$$

$$K_{iijj} = \frac{1}{2} \left[\frac{K_{ii}(\delta Q_j) + K_{ii}(-\delta Q_j) - 2K_{ii}(Q_0)}{\delta Q_j^2} + \frac{K_{jj}(\delta Q_i) + K_{jj}(-\delta Q_i) - 2K_{jj}(Q_0)}{\delta Q_i^2} \right]$$

The treatment is easily available through the Gaussian03 software and can be routinely applied for the investigation of molecules including up to 15 atoms. Also, it has been found that for several systems the computed anharmonic corrections are not very sensitive to the choice of the quantum chemistry method or the size of the basis set which means that the high-level computations may be performed to obtain harmonic frequencies while cheaper methods can be used for the calculation of the anharmonic corrections. Nevertheless, when applying the method it is not *a priori* clear whether the two assumptions on which the whole procedure rests are valid. Firstly, in the vicinity of a minimum the potential is approximated with the Taylor expansion which is truncated after the fourth order but often some of the two or three dimensional sections of the full molecular potential display more complicated dependence on the normal coordinates [79]. Secondly, the vibrational energy levels are obtained by using second order perturbation theory which can fail in the case of large anharmonic effects.

Anharmonic spectra in reduced dimensionality

In the case of large anharmonic effects and strong couplings between the vibrational modes a deeper insight into different coupling mechanisms shaping the vibrational bands can be obtained by the *reduced dimensionality approach*. In this method the vibrational problem is directly solved for a potential spanned by a smaller number of suitably chosen normal modes and evaluated on a grid of points. For example, the IR spectrum of the O-H...O fragment of malonaldehyde was investigated on the basis of a fully coupled 4D PES containing the O-H stretching, in-plane and out-of-plane OH bending and one low frequency mode O...O [34]. The normal mode representation of the Hamiltonian

$$\hat{H} = -\frac{\hbar^2}{2} \sum_{k=1}^{\tilde{n}} \left[\frac{1}{\mu_k} \frac{\partial^2}{\partial Q_k^2} \right] + V(Q_1, \dots, Q_{\tilde{n}}) \quad (3.42)$$

was used where \tilde{n} represents the dimensionality of the problem and μ_k is the reduced mass for the vibrational mode Q_k defined as¹⁰

$$\mu_k = \sum_i I_{ki}^{-2} m_i \quad (3.43)$$

A number of methods for solving the vibrational Schrödinger equation with the Hamiltonian given in Eq. (3.42) is known in the literature [80, 81, 82, 83]. In this work we implemented the Fourier grid Hamiltonian (FGH) method developed by C. C. Marston and G. G. Balint-Kurti [83]. The method represents a stable, fast and robust way for solving the vibrational Hamiltonian. It is combined with iterative diagonalization techniques to evaluate a limited number of the lowest eigenvalues. Briefly, the overall Hamiltonian is the sum of the kinetic energy and the potential energy term evaluated on an equidistant grid. The diagonalization of the resulting Hamiltonian matrix yields the eigenvalues and the eigenvectors which give the amplitudes of the vibrational wave functions on the grid points. The fundamental frequencies are then calculated as a differences of ground state and excited state energies. The FGH method is detailed in Appendix B.

An attractive feature of the normal mode approach is the assignment in terms of uncoupled normal modes (see Ref. [34]), the so called zero-order states

$$\hat{H}_0 = -\frac{\hbar^2}{2} \sum_k^{\tilde{n}} \left[\frac{1}{\mu_k} \frac{\partial^2}{\partial Q_k^2} + V(Q_k, \{Q_{l \neq k} = 0\}) \right] \quad (3.44)$$

The contribution of a particular eigenstate ψ_k^0 of \hat{H}_0 to the eigenstate of the full Hamiltonian \hat{H} in (3.42) can be inspected by analyzing the coefficients c_{lk}

$$\psi_l = \sum_k c_{lk} \psi_k^0 \quad (3.45)$$

The computationally limiting part, however, is the evaluation of a \tilde{n} -dimensional potential at the selected grid points since the potential is evaluated pointwise by using one of available quantum-chemistry methods.

¹⁰compare to Eq. (3.14)

3.3 Large amplitude treatment

None of the available methods for treating anharmonicity based on the normal mode coordinates is successful when treating the dynamics far away from the equilibrium position. In addition, normal mode coordinates appear to be unsuitable for reproducing the double minima shape of the potential energy surface. Consequently, the next section focuses on the LAM coordinates and gives an overview of the most important theoretical methods suitable for treating the large amplitude motion.

3.3.1 Internal coordinates

Internal coordinates (interatomic distances, valence and torsional angles) can serve as the coordinates that perform large amplitude motion. Typically, the remaining degrees of freedom (DOF) of the system are optimized in such a way to minimize the energy for a given internal coordinate.

For a set of \tilde{n} internal coordinates ρ the kinetic energy operator has a form [84]

$$\hat{T}_\rho = -\frac{\hbar^2}{2} \sum_{r=1}^{\tilde{n}} \sum_{s=1}^{\tilde{n}} \left[j^{-1/2} \frac{\partial}{\partial \rho_r} \left[j \cdot G^{rs} \frac{\partial}{\partial \rho_s} [j^{-1/2}] \right] \right] \quad (3.46)$$

where j is the determinant of the Jacobi transformation matrix $j = \det |J_{ij}|$, $J_{ij} = \partial x_i / \partial \rho_j$ and G^{rs} is an element of the Wilson kinetic energy G -matrix [71]:

$$G^{rs} = \sum_{i=1}^{3N} \frac{1}{m_i} \frac{\partial \rho_r}{\partial x_i} \frac{\partial \rho_s}{\partial x_i} \quad (3.47)$$

The G matrix is symmetric, i.e., $G^{rs} = G^{sr}$ and can be regarded as corresponding to reciprocal reduced masses. It is, like the terms j and $j^{-1/2}$, coordinate dependent. It is usually assumed that the coordinate dependence of the Jacobian j is much smaller than the dependence of the individual G^{rs} element and in that case Eq. (3.46) acquires a much simpler form:

$$\hat{T}_\rho \simeq -\frac{\hbar^2}{2} \sum_{r=1}^{\tilde{n}} \sum_{s=1}^{\tilde{n}} \frac{\partial}{\partial \rho_r} \left[G^{rs} \frac{\partial}{\partial \rho_s} \right] \quad (3.48)$$

By neglecting the kinetic energy coupling term Eq. (3.48) simplifies to

$$\hat{T}_\rho \simeq -\frac{\hbar^2}{2} \sum_{r=1}^{\tilde{n}} \frac{\partial}{\partial \rho_r} \left[G^{rr} \frac{\partial}{\partial \rho_r} \right] \quad (3.49)$$

while the assumption of a constant G -matrix leads to the expression

$$\hat{T}_\rho \simeq -\frac{\hbar^2}{2} \sum_{r=1}^{\tilde{n}} \sum_{s=1}^{\tilde{n}} G^{rs} \frac{\partial^2}{\partial \rho_s \partial \rho_r} \quad (3.50)$$

Finally, both the "no kinetic coupling" (3.49) and "constant G -matrix" (3.50) approximations can be combined giving an expression equal to the expression for the kinetic energy operator of orthogonal coordinates:

$$\hat{T}_\rho \simeq -\frac{\hbar^2}{2} \sum_{r=1}^{\tilde{n}} G^{rr} \frac{\partial^2}{\partial \rho_r^2} \quad (3.51)$$

The eigenvalues and eigenfunctions of the vibrational problems can be obtained by diagonalizing the grid representation of the vibrational Hamiltonians Eq. (3.46) - (3.51). The derivation of the Fourier grid Hamiltonian method (FGH) in internal coordinates was given by J. Stare and G. G. Balint-Kurti in 2003 [85] as a generalization of an already mentioned Fourier grid Hamiltonian method [83]. The procedure for solving the vibrational problem in internal coordinates by using the FGH method is explained in Appendix B.

The Reaction surface Hamiltonian approach (RSH)

Internal coordinates are often used as large amplitude coordinates that span the reaction surface in the Reaction surface Hamiltonian (RSH) approach. The method was developed by T. Carrington and W. Miller and was first applied to the dynamics of HAT in malonaldehyde [40]. It is based on the separation of the coordinate space into the reaction surface space of dimensionality \tilde{n} (the 'system') and the space of the harmonic displacement from the surface (the 'bath'). Consequently, the potential is just the potential energy on the surface V_0 of dimensionality \tilde{n} plus the vibrationally adiabatic energy of the $(3N - 6 - \tilde{n})$ modes:

$$V(\mathbf{r}) = V_0(\mathbf{r}) + \frac{\hbar}{2} \sum_{i=1}^{3N-6-\tilde{n}} \omega_i^2(\mathbf{r}) \mathbf{Q}_i^2 \quad (3.52)$$

The whole Hamiltonian has a form:

$$\hat{H}(\mathbf{r}, \mathbf{P}_r, \mathbf{Q}, \mathbf{P}_Q) = \frac{\hbar}{2} (\mathbf{P}_r, \mathbf{P}_Q) \begin{pmatrix} \mathbf{G}_{rr} & \mathbf{G}_{rQ} \\ \mathbf{G}_{Qr} & \mathbf{G}_{QQ} \end{pmatrix} \begin{pmatrix} \mathbf{P}_r \\ \mathbf{P}_Q \end{pmatrix} + V_0(\mathbf{r}) + \frac{\hbar}{2} \sum_{i=1}^{3N-6-\tilde{n}} \omega_i^2(\mathbf{r}) \mathbf{Q}_i^2 \quad (3.53)$$

where \mathbf{r} and \mathbf{Q} denote the reaction surface and the local normal mode coordinates, \mathbf{P}_r and \mathbf{P}_Q their conjugate momenta and ω_i is the frequency of the corresponding normal mode Q_i . In addition, \mathbf{G} denotes the G -matrix elements which can be treated as coordinate dependent reduced masses. Here the G -matrix is partitioned into \mathbf{G}_{rr} matrix of dimensions $\tilde{n} \times \tilde{n}$, \mathbf{G}_{rQ} matrix of dimensions $\tilde{n} \times (3N - \tilde{n})$ and \mathbf{G}_{QQ} matrix of dimensions $(3N - \tilde{n}) \times (3N - \tilde{n})$ to emphasize the kinetic couplings between the reaction space coordinates (on-surface degrees of freedom (DOF)) through \mathbf{G}_{rr} , the couplings

between the on-surface and off-surface DOF (\mathbf{G}_{r_Q}), and the couplings between the off-surface DOF (\mathbf{G}_{QQ}). If only the reaction space coordinates are strongly involved in the studied process then the coupling between the on-surface and off-surface DOF are neglected ($\mathbf{G}_{r_Q} = 0$) and the Hamiltonian has a simpler form

$$\hat{H}(\mathbf{r}, \mathbf{P}_r, \mathbf{Q}, \mathbf{P}_Q) = \hat{H}_r(\mathbf{r}, \mathbf{P}_r) + \hat{H}_Q(\mathbf{Q}, \mathbf{P}_Q; \mathbf{r}) \quad (3.54)$$

Here $\hat{H}_Q(\mathbf{Q}, \mathbf{P}_Q; \mathbf{r})$ is only parametrically dependent on the reaction surface coordinates \mathbf{r} . Several Hamiltonians related to the Eq. (3.54) exists in the literature [17, 39, 86], however only the formulation relevant for this thesis will be given in next section when discussing collective large amplitude coordinates.

For treating the HAT dynamics in malonaldehyde using the RSH approach, T. Carrington and W. Miller [40] have chosen two O-H bond lengths (the bond being broken and the bond being formed) as two large amplitude reaction surface coordinates. On a potential characterized by barrier height of 4.3 kcal mol⁻¹ they obtained the value of 60 cm⁻¹ for the tunneling splitting in malonaldehyde (experimental value being 21.58 cm⁻¹ [24, 87]). Three years later N. Shida, P. F. Barbara and J. E. Almöf [39] used the same approach to treat the HAT in malonaldehyde but on a three dimensional reaction surface spanned by the two O-H distances, and the O-O distance. On a potential with a barrier height of 7.1 kcal mol⁻¹ they obtained the ground state tunneling splitting of 9 cm⁻¹. More importantly, the same group of authors applied the RSH method in their investigation of the double HAT reaction in the formic acid dimer [17]. To span the 3D reaction surface they used six internal coordinates r_1, r_2, r_3, r_4, R_1 and R_2 (Figure 3.4) to form three symmetry adapted coordinates

$$\begin{aligned} \rho_1 &= (r_1 - r_3) + (r_2 - r_4) \\ \rho_2 &= R_1 + R_2 \\ \rho_3 &= (r_1 - r_3) - (r_2 - r_4) \end{aligned} \quad (3.55)$$

In this way, the symmetric synchronous hydrogen atom movement (ρ_1), the asymmet-

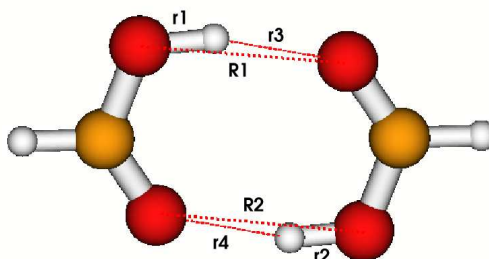


Figure 3.4: Formic acid dimer

ric (asynchronous) hydrogen atom movement (ρ_3) and the relative motion of the two monomers (ρ_2) have been explicitly included in the calculation. On a PES with the barrier height of 11.8 kcal mol⁻¹ the ground state tunneling splitting of 0.004 cm⁻¹ was predicted (the experimental value being 0.0125 cm⁻¹ [14]).

3.3.2 Minimum energy path based methods

A class of methods for treating LAM is based on the notion of the reaction path. The Intrinsic Reaction Path (IRP) [88] is the most widely used reaction path. It represents the steepest descent path in the mass weighted Cartesian coordinates connecting the saddle point and the minima on the PES. The IRP is obtained by solving the differential equation

$$\frac{d\mathbf{X}(s)}{ds} = -\frac{\nabla V}{|\nabla V|} \quad (3.56)$$

starting from a geometry slightly displaced from the saddle point along the normal mode with the imaginary frequency. In Eq. (3.56) $\mathbf{X}(s)$ is the mass-weighted geometry, s is the path length and ∇V is a gradient of a full-dimensional potential. Nowadays, efficient algorithms for following the reaction path have been developed [89, 90] and implemented in the quantum chemistry packages [67, 68].

The Reaction path Hamiltonian approach

Additional quantum chemistry calculations are required in order to generate the Hamiltonian on basis of the minimum energy path (Reaction path Hamiltonian [91]). At a sequence of points along the reaction path the vibrational analysis is performed. Hence, at each point on the reaction path ($X_{i\gamma}(s)$) one defines vibrational modes by diagonalizing the force constant matrix $\mathbf{K}^{\mathcal{P}}(s)$ (Eq. 3.20) from which rotation, translation and the vector that points along the reaction path have been projected out. Here, the projector \mathcal{P} differs from the one defined in Eq. (3.18) by an additional term which projects out the reaction path direction, i.e., the projector \mathcal{P} has a form

$$\mathcal{P}_{i\gamma, i'\gamma'} = \sqrt{\frac{m_i m_{i'}}{M^2}} \delta_{\gamma\gamma'} + \sum_{\alpha\beta\alpha'\beta'} \epsilon_{\alpha\beta\gamma} X_{i\beta} [I_0^{-1}]_{\alpha\alpha'} \epsilon_{\alpha'\beta'\gamma'} X_{i'\beta'} + v_{i\gamma}^t(s) v_{i'\gamma'}^t(s)$$

The eigenvectors $\{L_{i\gamma,k}\}$, $k = 1, \dots, 3N-7$ of the projected force constant matrix $\mathbf{K}^{\mathcal{P}}$ have frequencies $\{\omega_k^2\}$ and, as described previously, define the normal coordinates orthogonal to the IRP.

The potential is approximated as the reaction path energy ($V_0(s)$) plus a harmonic expansion with respect to the orthogonal degrees of freedom (Q_k) about the reaction

path:

$$V(s, Q_1, \dots, Q_{3N-7}) = V_0(s) + \sum_{k=1}^{3N-7} \omega_k(s)^2 Q_k^2$$

The kinetic energy of the system in terms of the coordinate set $(s, Q_1, \dots, Q_{3N-7})$ and their conjugate momenta $(p_s, P_1, \dots, P_{3N-7})$ has a rather complicated form. The classical Hamiltonian is

$$H(p_s, s, \{P_k, Q_k\}) = \sum_k \left(\frac{1}{2} P_k^2 + \frac{1}{2} \omega_k(s)^2 Q_k^2 \right) + V_0(s) + \frac{1}{2} \frac{[p_s - \sum_{k,l} Q_k P_l B_{k,l}(s)]^2}{[1 + \sum_k Q_k B_{k,3N-6}(s)]^2} \quad (3.57)$$

Central to this Hamiltonian are the coupling elements $B_{k,l}$ in the numerator defined by

$$B_{k,l}(s) = \sum_i \frac{\partial L_{i,k}(s)}{\partial s} L_{i,l}(s)$$

which describe the coupling of the different $(3N-7)$ vibrational modes Q_k along the reaction path. The $B_{k,3N-6}$ elements in the denominator of Eq. (3.57) describe the direct coupling of the reaction coordinate s and the $(3N-7)$ vibrational modes. These terms also define the curvature of the reaction path $\kappa(s)$ as

$$\kappa(s) = \left[\sum_k B_{k,3N-6}(s)^2 \right] \quad (3.58)$$

so one sees that the curvature is "portioned" among different vibrational modes. If the frequency of the normal modes greatly depend on the reaction coordinate s , it is an indication that the nature of the mode changes significantly along the reaction path. In that case strong coupling between these modes and the path mode is expected and this will manifest itself in the large contribution of these modes to the $B_{k,3N-6}$ and $B_{k,l}$ elements.

Although the RPH method has been used in the investigations of the vibrational spectra of HAT systems [69, 92], the form of kinetic energy operator in Eq. 3.57 complicates its application. Furthermore, it relies on *one*-dimensional dynamical model where the motion along the reaction path determines the large amplitude motion. Often, the IRP path is not a good representation of the actual reaction path and the dynamical motion can deviate strongly from the IRP. The alternative approach for treating the HAT systems would be the reaction surface Hamiltonian described in the previous section where the reaction surface allows for dynamics and tunneling far away and beyond the IRP.

3.3.3 Collective large amplitude coordinates

The collective large amplitude coordinates used here were first introduced by S. Takada and H. Nakamura [93] and were later used in the work of K. Yagi *et al.* [16] to span the

2D reaction surface (*reaction plane*) of malonaldehyde. They used the reaction plane as a starting point for the construction of a full-dimensional potential of malonaldehyde. The vectors that span the reaction plane are constructed on the basis of the known mass-weighted geometries of the stationary points on PES corresponding to the right-hand minimum (\mathbf{X}_R), the transition state (\mathbf{X}_{TS}) and the left-hand minimum (\mathbf{X}_L). For a system with N_{at} atoms, two $3N_{at}$ dimensional vectors defined as

$$\mathbf{d}_1 = \frac{\mathbf{X}_R - \mathbf{X}_L}{|\mathbf{X}_R - \mathbf{X}_L|} \quad (3.59)$$

$$\mathbf{d}_2 = \frac{\mathbf{X}_C - \mathbf{X}_{TS}}{|\mathbf{X}_C - \mathbf{X}_{TS}|} \quad (3.60)$$

correspond to two large amplitude coordinates, with \mathbf{X}_C being the center geometry

$$\mathbf{X}_C = \frac{1}{2}(\mathbf{X}_R + \mathbf{X}_L) \quad (3.61)$$

Given a molecular symmetry transformation i.e. permutation of atoms and rotation with the property

$$T\mathbf{X}_R = \mathbf{X}_L \quad (3.62)$$

the reaction plane vectors will transform as

$$T\mathbf{d}_1 = -\mathbf{d}_1, \quad T\mathbf{d}_2 = \mathbf{d}_2 \quad (3.63)$$

The All-Cartesian Reaction Plane (CRP) Hamiltonian

The all-Cartesian reaction surface Hamiltonian formulation has been originally introduced by Ruf and Miller [86]. They have selected the Cartesian coordinates of the reactive atom as reaction coordinates which span the reaction surface. All the other DOF are expanded in a Taylor series up to second order around this surface. However, a strong coupling between the resulting reactive coordinate and the DOF that describe the motion of the heavy atoms in the case of HAT processes indicates that such a separation might not give the simplest PES representation of the studied process [19]. K. Giese and O. Kühn were first to introduce the reaction plane coordinates into the formalism of the all-Cartesian reaction surface Hamiltonian and used it to describe the HAT reaction in tropolone [19]. In their method the reactive DOF are given by the reaction plane spanned by the vectors \mathbf{d}_1 and \mathbf{d}_2 and the remaining DOF $\{Q\}$ are harmonically approximated for each value of the \mathbf{d}_1 and \mathbf{d}_2 . The full potential is approximated with the potential

$$V(d_1, d_2, \mathbf{Q}) = V(d_1, d_2, 0) + \sum_{i=1}^{N-2} \left. \frac{\partial V(d_1, d_2, \mathbf{Q})}{\partial Q_i} \right|_{Q=0} Q_i + \frac{1}{2} \sum_{i,j=1}^{N-2} \left. \frac{\partial^2 V(d_1, d_2, \mathbf{Q})}{\partial Q_i \partial Q_j} \right|_{Q=0} Q_i Q_j \quad (3.64)$$

The validity of the expansion given in Eq. (3.64) depends on the choice of $\mathbf{Q} = \mathbf{0}$, but it relies primarily on the fact that the reaction plane should span the relevant configuration space. A reasonable assumption would be that in this case IRP should lie approximately in the reaction plane. The root mean squared (RMS) difference between the IRP geometries and the projection of the IRP on the reaction plane is given by

$$\sigma^{(2)}(s) = \frac{1}{\sqrt{N_{\text{at}}}} \left| \mathbf{M}^{-1/2} \left(1 - \sum_{i=1}^2 \mathbf{d}_i \mathbf{d}_i^t \right) (\mathbf{X}(s) - \mathbf{X}_{\text{TS}}) \right| \quad (3.65)$$

If the RMS difference, $\sigma^{(2)}(s)$, between the IRP geometries and the geometries projected onto the reaction plane is small, the IRP is incorporated in the reaction plane and the reaction plane can serve as a good starting point for the construction of the full dimensional PES as given in Eq. (3.64).

The choice of the Q modes

As emphasized in Ref. [19] the $\{Q\}$ modes should be decoupled, thus chosen in such a way that the off-diagonal elements in the third term of Eq. (3.64) are small. One possible way of achieving this would be to use the eigenvectors of the Hessian at some special geometry, for instance at the transition state geometry \mathbf{X}_{TS} :

$$K^{\mathcal{P}} = (\mathbf{1} - \mathcal{P}) \mathbf{K}^{(b)}(\mathbf{X}_{\text{TS}}) (\mathbf{1} - \mathcal{P}) \quad (3.66)$$

where \mathcal{P} is a projector onto the 8-dimensional space spanned by the \mathbf{d}_1 , \mathbf{d}_2 and the three rotational and the three translational directions. In this case the projector \mathcal{P} differs from the one defined in Eq. (3.18) by an additional term which projects out the reaction directions. Here, the projector \mathcal{P} has a form

$$\mathcal{P}_{i\gamma, i'\gamma'} = \sqrt{\frac{m_i m_{i'}}{M^2}} \delta_{\gamma\gamma'} + \sum_{\alpha\beta\alpha'\beta'} \epsilon_{\alpha\beta\gamma} X_{i\beta} [I_0^{-1}]_{\alpha\alpha'} \epsilon_{\alpha'\beta'\gamma'} X_{i'\beta'} + \sum_{i=1}^2 d_i^t d_i \quad (3.67)$$

$(3N-8)$ eigenvectors \mathbf{Q}_j of the projected force constant matrix $K^{\mathcal{P}}$ have non-zero eigenvalues. Selecting the transition state geometry as the reference geometry the eigenvectors \mathbf{Q}_j classify as symmetric (+) or antisymmetric (-) with respect to the symmetry transformation \mathcal{T} .

Definition of the model coordinates

The potential $V(d_1, d_2, Q_1, \dots, Q_{3N-8})$ is still full dimensional. In order to make the HAT reactions in polyatomic molecules feasible, a smaller number \tilde{n} of relevant modes

should be selected. In general, every linear combination of modes Q_j , $j = 1, \dots, 3N-8$ can be used as a relevant mode

$$q_k = \sum_{j=1}^{N-8} c_{kj} Q_j, \quad k = 1, \dots, N-8 \quad (3.68)$$

The assembly of vectors $(d_1, d_2, q_1, \dots, q_{\tilde{n}})$ is called *model coordinates* [19] and the remaining $(3N-8-\tilde{n})$ DOF are called *spectator modes*. In the new coordinates the CRP Hamiltonian is

$$\begin{aligned} \hat{H} = & -\frac{1}{2} \sum_{i=1}^2 \frac{\partial^2}{\partial d_i^2} - \frac{1}{2} \sum_{k=1}^{\tilde{n}} \frac{\partial^2}{\partial q_k^2} + V(d_1, d_2, 0) + \sum_{i=1}^{\tilde{n}} \frac{\partial V(d_1, d_2, \mathbf{q})}{\partial q_i} \Big|_{q=0} q_i \\ & + \frac{1}{2} \sum_{i,j=1}^{\tilde{n}} \frac{\partial^2 V(d_1, d_2, \mathbf{q})}{\partial q_i \partial q_j} \Big|_{q=0} q_i q_j + \frac{1}{2} \sum_{k=1}^{3N-8-\tilde{n}} \hbar \omega_k(d_1, d_2) \end{aligned} \quad (3.69)$$

and the spectator modes contribute to the potential only via their (d_1, d_2) dependent zero point energies. The set of model coordinates is orthogonal thus resulting in a diagonal form of a kinetic energy operator.

If the dynamical treatment is directed towards a specific frequency range, the relevant model coordinates q are chosen in such a way to reproduce the motion along targeted vibrational modes. As the vibrational assignment in the experimental spectra are done in term of the minimum energy structure, a practical choice of relevant directions q would thus be to analyze the overlaps between the Q_j modes and the normal modes at one of the minima ($\mathbf{Y}_k^{(f)}$)

$$p_{kj} = \mathbf{Y}_k^{(f)} \cdot \mathbf{Q}_j \quad (3.70)$$

If an absolute value p_{kj} is large, the corresponding Q_j mode is relevant and should be included as a model coordinate. In passing note that the vectors corresponding to model coordinates have to be either symmetric or antisymmetric with respect to the transformation \mathcal{T} and therefore the full normal modes of the minima ($\mathbf{Y}_k^{(f)}$) can not be chosen directly as modes q since they don't have the required symmetry properties. For instance, the normal modes of the right minima ($\mathbf{Y}_{k,R}^{(f)}$) will transform as

$$\mathcal{T} \mathbf{Y}_{k,R}^{(f)} = -\mathbf{Y}_{k,L}^{(f)} \quad \text{or} \quad \mathcal{T} \mathbf{Y}_{k,R}^{(f)} = \mathbf{Y}_{k,L}^{(f)}$$

According to the Ref. [19] for a normal mode $\mathbf{Y}_k^{(f)}$ the model coordinate q_k should be defined as $q_k = Q_j$ for that Q_j with the largest overlap $|p_{kj}|$. In the case when a certain mode $\mathbf{Y}_k^{(f)}$ has large overlaps with more than one Q_j mode, a linear combinations of these modes should be made according to Eq. (3.68).

It should be also emphasized that the modes q_k are arbitrary in a sense that any linear combination of q_k modes of the same symmetry is equivalent and must give the

same physical results. However, the so-called *reduced normal modes* represent a unique set of coordinates. They are defined as eigenvectors of the Hessian at the minimum or transition state geometry projected onto the $(\tilde{n}+2)$ space spanned by the \mathbf{d}_1 , \mathbf{d}_2 and \tilde{n} \mathbf{q}_k vectors (model coordinates):¹¹

$$\mathcal{R} \mathbf{K}^{(f)}(\mathbf{X}_{\text{MIN}})\mathcal{R} \quad (3.71)$$

where $\mathbf{K}^{(f)}$ is a full force constant matrix at the minima geometry. The reduced normal coordinates will be denoted as $\mathbf{Y}_k^{(\tilde{n}+2)\text{D}}$ where $(\tilde{n}+2)$ is the dimensionality of the reduced space. According to Ref. [19] for setting the Hamiltonian, it is most convenient to use model coordinates for they retain the required symmetry properties with respect to the symmetry transformation \mathcal{T} . All physically relevant quantities, however, should be related to the reduced normal modes.

The reduced normal modes ($\mathbf{Y}_k^{(\tilde{n}+2)\text{D}}$) can be further investigated by analyzing their connection with the full normal modes of the minima ($\mathbf{Y}_j^{(f)}$) by inspecting their overlaps \tilde{p}_{jk} :

$$\tilde{p}_{jk} = \left(\mathbf{Y}_j^{(f)} \right)^T \mathbf{B} \mathbf{Y}_k^{(\tilde{n}+2)\text{D}} \quad (3.72)$$

where \mathbf{B} is a $3N_{\text{at}} \times (\tilde{n}+2)$ matrix that transforms from the reduced space $(d_1, d_2, q_1, \dots, q_{\tilde{n}})$ to the full $3N_{\text{at}}$ dimensional space (d_1, d_2, \mathbf{Q}) :

$$\mathbf{B} = (\mathbf{d}_1 \mathbf{d}_2 \mathbf{q}_1 \dots \mathbf{q}_{\tilde{n}}) \quad (3.73)$$

and vectors $\mathbf{d}_1, \mathbf{d}_2, \mathbf{q}_1, \dots, \mathbf{q}_{\tilde{n}}$ that span the reduced space constitute its columns. The relation between the reduced and full normal modes of the minima are necessary in order to establish the connection to the experimental assignment in the full-dimensional space.

"Mobile" coordinates

The second set of collective large amplitude coordinates treated in this thesis and yielding the kinetic energy in a diagonal form is due to Hirschfelder and co-workers [94, 95, 96]. This set of coordinates is based on the "mobile model".

The mobile is constructed as follows: The coordinate \mathbf{S}_N is a vector joining the center of mass of the system to the origin of the space fixed system:

$$\mathbf{S}_N = M^{-1/2} \sum_{j=1}^N m_j \mathbf{R}_j \quad (3.74)$$

where \mathbf{R}_j is a position of the particle in a space fixed system, m_j is a mass of the j -th particle and M is the mass of the molecule $M = \sum_{j=1}^{N_{\text{at}}} m_j$. The other $(N_{\text{at}} - 1)$ coordinates

¹¹the projector has a form $\mathcal{R} = \sum_{i=1}^2 d_i^t d_i + \sum_{k=1}^{\tilde{n}} q_k^t q_k$

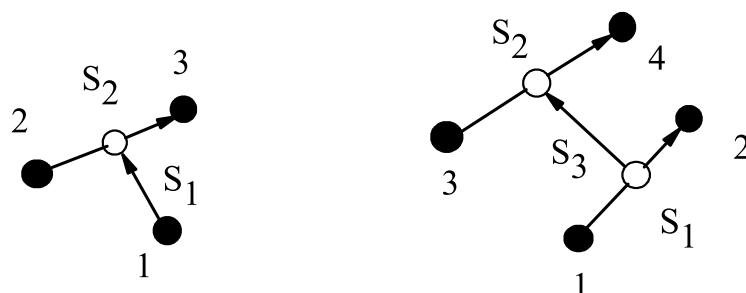


Figure 3.5: One possible mobile for a three and four particle system. The solid circles are particles, and open circles are center of mass for a group of particles.

are vectors joining together the center of mass of groups of particles. For instance, if $\mathbf{R}_c(A)$ is a center of mass and M_A is the mass of the particles in a group A

$$M_a = \sum_{\alpha \in A} m_\alpha, \quad \mathbf{R}_c(A) = \sum_{\alpha \in A} m_\alpha \mathbf{R}_\alpha / M_A \quad (3.75)$$

then the coordinate joining the group A to group B will be

$$\mathbf{S}_i = (M_A M_B / (M_A + M_B))^{1/2} [\mathbf{R}_c(A) - \mathbf{R}_c(B)] \quad (3.76)$$

If the group A consists of a single particle, then M_A and $\mathbf{R}_c(A)$ are just the mass and the coordinate of the particle A . One of many possible mobiles for a three and a four particle system is presented in Figure 3.5.

The coordinates \mathbf{S}_i yield the kinetic energy operator in the diagonal form. According to Ref. [96] new sets of coordinates $(\mathbf{S}'_1, \dots, \mathbf{S}'_{(N-1)}, \mathbf{S}'_N)$ can be generated by unitary transformations (rotations, reflections) of a given set of coordinates $(\mathbf{S}_1, \dots, \mathbf{S}_{(N-1)}, \mathbf{S}_N)$ obtained from the mobile. The derivation of tailored coordinates for treating HAT reactions will be given in section 4.3.3.

Chapter 4

Results and discussion

4.1 Electronic structure calculations

4.1.1 Acetylacetone

The potential energy surface for hydrogen atom transfer in acetylacetone was explored by using second and fourth order Moller-Plesset perturbation theory (MP2, MP4) and density functional theory (DFT) with the B3LYP [97] and the B1LYP [98] exchange-correlation functionals. The geometries relevant to the HAT reaction in ACAC were optimized and the harmonic vibrational analysis has been performed in order to classify each geometry as a minimum, a transition state or a higher order saddle point. Six stationary points that are relevant for the HAT dynamics in ACAC are shown in Figure 4.1. The minimum energy structure of ACAC in the gas phase is confirmed to be the *syn*-enol isomer of ACAC with the C_s point group symmetry (denoted as **SYN**) while the **TS3** structure is a first-order saddle point and represents the transition state for the intramolecular HAT reaction between the two equivalent *syn*-enol isomers. The barrier height for intramolecular HAT in ACAC (ΔE_1 in Table 4.1) was calculated as the energy difference between the energies of the **TS3** and **SYN** geometries optimized on various levels of theory. This was done in order to critically examine various quantum chemical methods and to identify the level of theory which would make the HAT dynamics investigation in ACAC possible by offering the best compromise between the reliability of the results and the computational time. The reference coupled cluster CCSD(T)/cc-pVTZ//MP2(FC)/cc-pVTZ barrier height was evaluated as 3.03 kcal mol⁻¹. Lower levels of theory predict the HAT barriers in the range between 2.15 kcal mol⁻¹ (B3LYP/6-311+G(2d,2p)) and 3.41 kcal mol⁻¹ (MP4/6-311+G(2d,2p)//MP2/6-311+G(2d,2p)). It has been shown that the B3LYP functional underestimate the HAT barrier for it overestimates the electron correlation effects, but that the B1LYP functional with a moderate 6-311G(d,p) basis set gives a barrier which is only 0.2 kcal mol⁻¹ lower than the

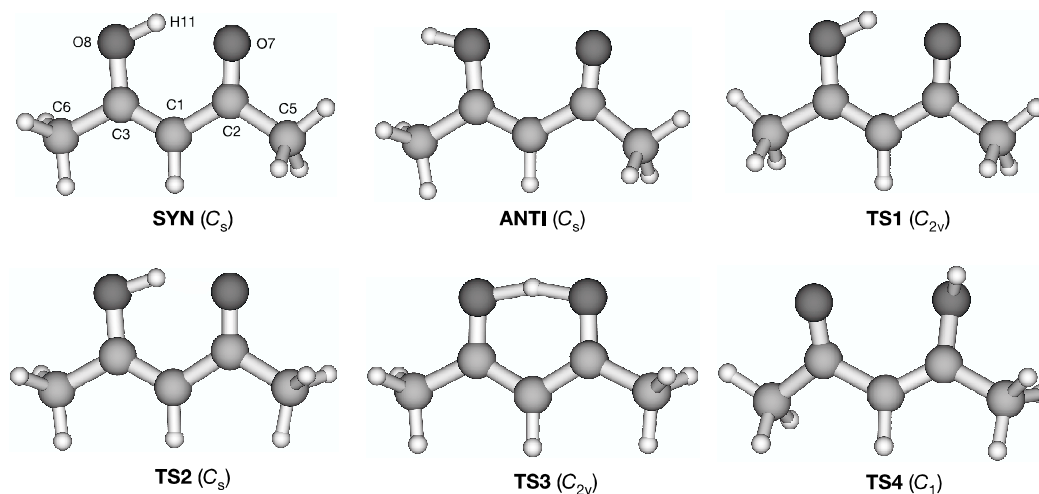


Figure 4.1: Structures relevant for the proton transfer dynamics in ACAC. Upper panel: the global minimum structure (**SYN**), the local minimum of the *anti*-enol ACAC (**ANTI**), and the transition state for the rotation of the proximal methyl group (**TS1**). Lower panel: the transition states for the rotation of the distal methyl group (**TS2**), HAT reaction (**TS3**) and *syn-anti* isomerization (**TS4**).

Table 4.1: Classical energy barriers for proton transfer (ΔE_1) and rotation of the distal methyl group (ΔE_2) calculated on various levels of theory.

Level of theory	ΔE_1 / kcal mol ⁻¹	ΔE_2 / kcal mol ⁻¹
B3LYP/6-311+G(2d,2p)	2.15	0.08
B1LYP/6-311G(d,p)	2.79	0.13
B1LYP/6-311+G(d,p)	2.79	0.09
B1LYP/6-311++G(d,p)	2.79	0.09
B1LYP/6-311+G(2d,2p)	2.62	0.11
B1LYP/6-311++G(2d,2p)	2.63	0.12
MP2(FC)/6-311G(d,p)	2.77	0.25
MP2(FC)/6-311+G(d,p)	2.64	0.26
MP4(FC)/6-311+G(d,p)	3.01	0.24
MP2(FC)/6-311G(2d,2p)	3.20	0.35
MP2(FC)/6-311+G(2d,2p)	2.91	0.27
MP2(FC)/6-311++G(2d,2p)	2.91	0.27
CCSD(T)/cc-pVTZ	3.03	0.27

CCSD(T) result. Hence, it represents the best candidate for the treatment of dynamics. The wide range of values for the barrier height seen in the Table 4.1 is typical for the HAT reactions and indicates how significant the proper inclusion of electron correlation effects is when reproducing the barriers for the HAT reactions [31].

One also notices that the **TS3** structure and the minimum energy structure **SYN** differ in the orientation of the methyl groups relative to the chelate ring. The internal rotation of the two methyl groups was investigated and as a result two first order saddle points on the ACAC PES (denoted as **TS1** and **TS2**) were located and identified as transition states for the rotation of the proximal and of the distal methyl group. The **TS2** structure is central for further investigations for it exhibits the same orientation of the methyl groups as the **TS3** transition state for the HAT reaction. The energies of the structure **TS2** relative to the minima structure **SYN** (barrier height for the rotation of the distal methyl group) at various level of theory are given in Table 4.1 as ΔE_2 . At the CCSD(T)/cc-pVTZ//MP2(FC)/cc-pVTZ level of theory the barrier height of 0.27 cm^{-1} was evaluated, while lower levels of theory give values in the range between $0.08 \text{ kcal mol}^{-1}$ (B3LYP/6-311+G(2d,2p)) and $0.27 \text{ kcal mol}^{-1}$ (MP4(FC)/6-311+G(2d,2p)//MP2(FC)/6-311+G(2d,2p)). The **TS1** structure represents the transition state for the rotation of the proximal methyl group. The barrier height for the rotation of the proximal methyl group is found to be $0.25 \text{ kcal mol}^{-1}$ at MP2(FC)/6-311G(d,p) level of theory. These results are consistent with the NMR spin lattice relaxation time measurements where the existence of two energetically distinct methyl groups with hindering potentials of the order of 180 and 590 K (equivalent to 0.35 and $1.17 \text{ kcal mol}^{-1}$) was established [33].

Table 4.2 confronts the structural parameters for the most relevant structures (conformations **SYN**, **TS1** and **TS2**) obtained at the MP2/6-311G(d,p) level of theory with the available X-ray [48] and electron diffraction data [46]. The difference in the experimental structures complicates the comparison with the theory. Yet, it can be concluded that the experimental minima structures resemble more the **TS2** than the **SYN** structure. For instance, the experimental oxygen-oxygen distance is 0.012 \AA shorter than the same distance calculated for the **SYN** structure, but only 0.004 \AA longer than the **TS2** oxygen-oxygen distance. Geometrical parameters for the **SYN** structure and **TS3** structure calculated on various levels of theory are confronted in Table 4.3. All methods predict the shortening of the O-O donor acceptor distance, the shortening of the C-O donor distance and the elongation of the C-O acceptor distance during the HAT reaction (transition from a **SYN** structure to **TS3** structure). When compared to the experimental structures in Table 4.2 one notices that the largest deviation from the experimental values occurs for the geometrical parameters of the O-H...O fragment. While the MP2

Table 4.2: Geometrical parameters of the *enol*-ACAC calculated at the MP2(FC)/6-311G(d,p) level of theory in comparison with experimental geometries [48, 46]. The distances are given in Å, and the angles are given in degrees.

Bond/Angle	SYN	TS2	TS1	X-ray	ED
O ₇ -O ₈	2.548	2.531	2.535	2.535	2.512
O ₈ -H ₁₁	0.996	1.000	1.000	1.030	1.049
C ₁ -C ₂	1.451	1.447	1.448	1.412	1.430
C ₁ -C ₃	1.370	1.372	1.372	1.338	1.382
C ₂ -C ₅	1.511	1.513	1.512	1.478	1.493
C ₃ -C ₆	1.495	1.495	1.502	1.554	1.525
C ₂ -O ₇	1.244	1.246	1.246	1.238	1.243
C ₃ -O ₈	1.328	1.325	1.323	1.331	1.319
C ₂ -C ₁ -C ₃	120.21	119.90	120.05	122.2	119.7
C ₁ -C ₂ -O ₇	121.90	121.86	121.91	120.5	123.0
C ₁ -C ₃ -O ₈	122.44	122.25	122.18	122.8	121.0
C ₁ -C ₂ -C ₅	117.98	119.21	123.56		118.1
C ₁ -C ₃ -C ₆	124.00	123.98	123.56		124.1
O ₇ -H ₁₁ -O ₈	151.14	151.77	151.75		
C ₃ -O ₈ -H ₁₁	104.47	104.32	104.36		
energy /kcal mol ⁻¹	0	0.25	1.45		

Table 4.3: The geometrical parameters of the minimum (asym) and of the transition structure **TS3** (sym). All the distance are given in Å.

Level of theory	OO _{asym}	OH _{asym}	COD _{asym}	COA _{asym}	OO _{sym}	CO _{sym}
B3LYP/6-311+G(2d,2p)	2.534	1.004	1.325	1.246	2.362	1.284
B1LYP/6-311G(d,p)	2.553	0.997	1.325	1.241	2.359	1.281
B1LYP/6-311+G(d,p)	2.556	0.997	1.326	1.242	2.358	1.283
B1LYP/6-311++G(d,p)	2.556	0.998	1.326	1.242	2.358	1.283
B1LYP/6-311+G(2d,2p)	2.545	0.998	1.325	1.242	2.359	1.282
B1LYP/6-311++G(2d,2p)	2.545	0.998	1.325	1.242	2.359	1.282
MP2(FC)/6-311G(d,p)	2.548	0.996	1.328	1.244	2.354	1.283
MP2(FC)/6-311+G(d,p)	2.547	0.998	1.330	1.247	2.354	1.285
MP2(FC)/6-311G(2d,2p)	2.553	0.995	1.330	1.246	2.361	1.285
MP2(FC)/6-311+G(2d,2p)	2.548	0.998	1.331	1.249	2.361	1.287
MP2(FC)/6-311++G(2d,2p)	2.548	0.998	1.331	1.249	2.361	1.287

and B1LYP structures are consistent, the B3LYP structure differs considerably and predicts an enol geometry closer to the solid state experimental value. Taking into account that the computations have been performed on isolated molecules and that the MP2 geometries are usually in good agreement with the gas phase experimental results, it is reasonable to consider the B3LYP results as less reliable.

During the geometrical optimization for large oxygen-oxygen distances the bridging hydrogen atoms moves out of the chelate ring plane and the *syn*-enol structure transforms into the *anti*-enol structure shown in Figure 4.1. The *anti*-enol isomer also has a planar structure with C_s point-group symmetry. The structure was determined at the MP2(FC)/6-311+G(d,p), MP4(FC)/6-311+G(d,p)//MP2(FC)/6-311+G(d,p) and at the B1LYP/6-311+G(d,p) levels of theory. The energy of an *anti*-enol structure relative to the *syn*-enol structure was evaluated to be 14.78 kcal mol⁻¹, 14.35 kcal mol⁻¹ and 16.21 kcal mol⁻¹ at the three levels of theory, respectively. The transition state for the *syn-anti* isomerization (**TS4**) with one imaginary frequency was determined at the same levels of theory. The structure was found to be a non-planar structure with C_1 point-group symmetry and a large isomerization barrier of 18.35, 17.71 and 20.57 kcal mol⁻¹ at the MP2(FC)/6-311+G(d,p), MP4(FC)/6-311+G(d,p)//MP2(FC)/6-311+G(d,p) and at the B1LYP/6-311+G(d,p) levels of theory was found. In the C_s symmetry subspace a second order saddle-point (**SOSP**) with two imaginary frequencies was located; one is an in plane A' mode (1324i cm⁻¹) while the other is out-of-plane A'' mode (1129i cm⁻¹). The result proves the non existence of a true transition state for *syn-anti* isomerization in the C_s symmetry subspace. The energy of the **SOSP** structure relative to the **SYN** structure is calculated as 44.82 kcal mol⁻¹ at the MP2(FC)/6-311G(d,p) level of theory.

The results presented here uncover the complexity of the PES of the ACAC. The full-dimensional PES of the enol-form is characterized by 18 equivalent but permutationally distinct global minima, **SYN** (for each of the two hydrogen H11 positions there are 9 cyclic permutation of the methyl group atoms), 36 **ANTI** structures, 18 **TS2** first order saddle points and 9 **TS3** saddle points.

Intrinsic reaction path calculations

Next, we consider the minimum energy paths in mass-weighted Cartesian coordinates (Intrinsic Reaction Path (IRP)) for the *syn-anti* isomerization, for the methyl rotation and for the intramolecular HAT reaction. They were found at the MP2(FC)/6-311G(d,p) level of theory using the Gonzales-Schlegel second order algorithm [90] as implemented in Gamess package [68]. The calculations are repeated by using DFT theory with the B1LYP and B3LYP functionals and consistent results were obtained.

The IRP for the *syn-anti* isomerization connects the *syn-enol* isomer (**SYN**) and the *anti-enol* isomer (**ANTI**) via the **TS4** structure as schematically illustrated in Figure 4.2. Two major geometrical changes occurring during the IRP involve the change of the $H_{11}O_8C_3C_1$ and $O_7C_2C_3O_8$ dihedral angles. During the IRP the dihedral angle $H_{11}O_8C_3C_1$ changes its value from 0° at the *syn-enol* structure via 106° at **TS4** to 180° at the *anti-enol* structure. The dihedral angle $O_7C_2C_3O_8$ changes its value from 0° at the minimum to 29.7° at **TS4**.

The IRP for the internal rotation of the distal methyl group connects two equivalent **SYN** structures of C_s symmetry (**SYN1** and **SYN1'** in Figure 4.3) over a first order saddle point **TS2** of C_s symmetry. All other non-stationary points on the IRP have C_1 symmetry. During the internal rotation the internuclear distances and bond angles in the enol cycle change no more than 0.017 \AA (O_7O_8 distance) and 0.63° ($O_7H_{11}O_8$ angle). It should also be stressed that as a result of a local C_{3v} symmetry of the methyl group, there are three equivalent minima on the methyl rotation reaction path and three corresponding transition structures [52].

The IRP for the hydrogen atom transfer reaction in ACAC connects the **SYN1** and **SYN2** structures as shown in Figure 4.2. Compared to the two previous cases it represents a much more complicated path. The IRP search always starts from a geometry slightly displaced from the transition state along the normal coordinate with imaginary frequency. In the case of ACAC the transition state for HAT (**TS3**) has a C_{2v} symmetry and the normal mode containing the imaginary frequency has a B_2 symmetry. Due to symmetry conservation [99, 100] the IRP starting from **TS3** in a direction parallel to the

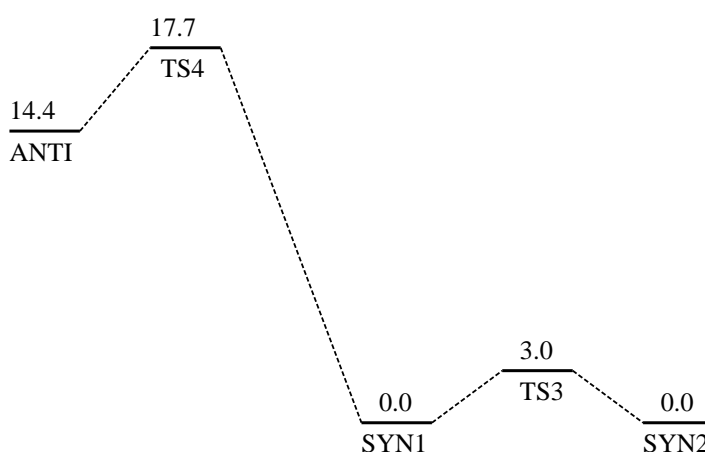


Figure 4.2: A schematic representation of reaction paths for the intramolecular HAT and *syn-anti* isomerization in ACAC. The relative energies are calculated at MP4/6-311+G(d,p)//MP2/6-311+G(d,p) level of theory.

B_2 mode ends in another transition state **TS2**, the one for the rotation of the distal methyl group (Figure 4.3). At **TS2** there is a branching possibility for the IRP giving two equivalent C_s structures (**SYN1** and **SYN1'**) (see solid line path in Figure 4.3). However, since the force constant corresponding to the methyl rotation has a positive sign at **TS3** and a negative sign at **TS2** there must be a point on IRP between the **TS3** and **TS2** where the sign change occurs. This point is called the valley-ridge inflection (**VRI**) point [101] and represents a point where an IRP changes its geometrical character on PES from a valley to a ridge (see Figure 4.3). Due to the presence of the **VRI** point the concept of the IRP breaks down and is substituted by the so-called "bifurcating reaction path" connecting the **VRI** and the **SYN1** and **SYN1'** structures [102, 103]. To trace the bifurcating reaction path the approach of Taketsugu et al. [100] was followed. The Gonzales-Schlegel algorithm as implemented in Gamess package was used with a step size of 0.01 bohr amu^{-1/2} and a cut-off for the norm of the mass weighted gradient tangent of 0.00005 E_h bohr⁻¹ amu^{1/2}. All other parameters were kept at their default values [68]. To locate the **VRI** point, the normal mode analysis along the IRP was performed. Prior to the frequency calculation all the structures were rotated in order to fulfil the Eckart conditions with respect to the reference C_{2v} structure. The **VRI** point was identified as a point where the eigenvalue of the Hessian orthogonal to the gradient direction has a zero eigenvalue and was located at $\mathbf{q}_2 = 1.34 a_0 \text{ amu}^{-1/2}$ (**TS2** structure being at $\mathbf{q}_2 = 1.5 a_0 \text{ amu}^{-1/2}$). The geometrical parameters of a **VRI** structure are presented in Table 4.4. By comparing them to the geometrical parameters of the **TS2** structure it can be concluded

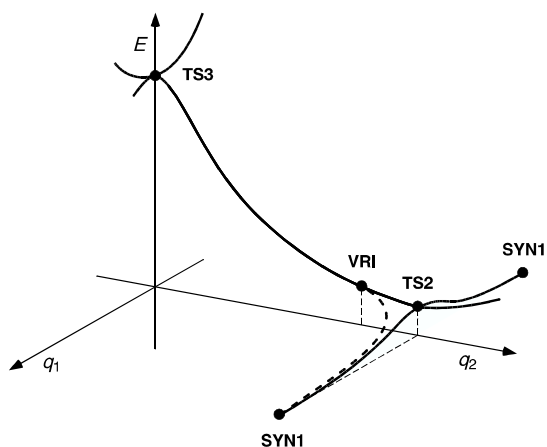


Figure 4.3: A sketch of the difference between the bifurcating reaction path (dotted line) and the IRP (solid line). The IRP calculation proceeds from **TS3** to **TS2** and from **TS2** to **SYN1**. The valley-ridge inflection point (**VRI**) is the point at which the two paths diverge.

Table 4.4: Geometrical parameters of the valley-ridge inflection point (**VRI**) calculated at the MP2(FC)/6-311G(d,p) level of theory. The distances are given in Å, and the angles are given in degrees. The energy difference, ΔE , is given with respect to the minimum *syn-enol* structure

Bond/Angle	VRI	Bond/Angle	VRI	Bond/Angle	VRI
O ₇ -O ₈	2.512	O ₈ -H ₁₁	1.003	C ₁ -C ₂	1.446
C ₁ -C ₃	1.373	C ₂ -C ₅	1.512	C ₃ -C ₆	1.495
C ₂ -O ₇	1.247	C ₃ -O ₈	1.324	C ₂ -C ₁ -C ₃	119.5
C ₁ -C ₂ -O ₇	121.80	C ₁ -C ₃ -O ₈	122.11	C ₁ -C ₂ -C ₅	119.61
C ₁ -C ₃ -C ₆	124.27	O ₇ -H ₁₁ -O ₈	152.45	C ₃ -O ₈ -H ₁₁	104.12
Energy/ E_h	-344.9394671	$\Delta E/\text{kcal mol}^{-1}$	0.28		

that these two structures are geometrically very close. At this stage the H-atom transfer has been completed (the O-H distance of **VRI** is 1.004 Å and at the minimum structure 0.996 Å) and the only difference is a shorter oxygen-oxygen distance in **VRI** (2.506 Å compared to 2.531 Å in **TS2**). The **VRI** and **TS2** structure are also energetically very close, the energy difference being only 0.06 kcal mol⁻¹. These findings indicate that the bifurcating path (dotted line in Figure 4.3) rapidly converges to the IRP for the rotation of the distal methyl group which connects the **TS2** and one of the **SYN** structures. Also, our analysis suggests that although the HAT reaction and the distal methyl rotation are coupled they are not synchronised. The HAT reaction is triggered only after the methyl groups have reached an eclipsed conformation.

The HAT reaction involves a large flow of electron density in the chelate ring, but the electron density on the methyl groups remains almost unchanged. In Figure 4.4 a contour plot of the correlated electron density in the **SYN** and **TS2** structures is presented.

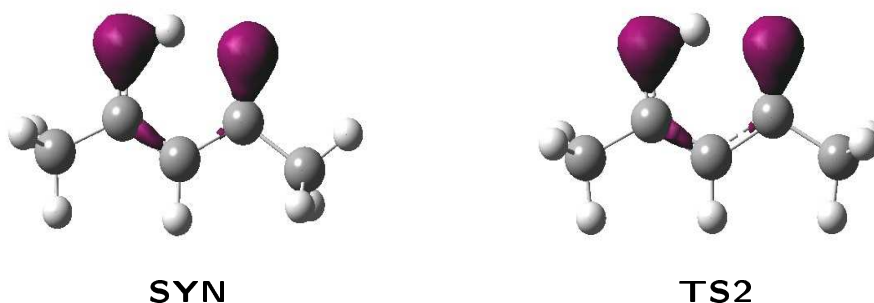


Figure 4.4: The electron density distributions in **SYN** and **TS2** conformers of ACAC at an isosurface value of 0.3 e Å⁻³. Calculated at the MP2/6-311G(d,p) level of theory.

During the rotation of the methyl groups, the charge density in the O-H...O region has been changed in a very limited extent. This is also consistent with the non-synchronous mechanism, while the synchronised mechanism would imply a large change of electron density in the HAT moiety. This findings allow to conclude that the HAT reaction in ACAC can be treated by fixing the methyl groups in one of the eclipsed conformations which in turn provides a remarkable simplification when treating the hydrogen atom tunneling dynamics.

4.1.2 The formic acid dimer

As in a case of ACAC, a number of quantum chemistry methods have been used for the description of electronic structure of FAD. These include second order Möller-Plesset perturbation theory (MP2), coupled cluster theory (CC) and density functional theory (DFT) with the B3LYP exchange-correlation functional [97]. These methods have been used to optimize the geometries of the FAD stationary points. It was confirmed that the structure of the global minima of FAD corresponds to a C_{2h} geometry while the transition state for the HAT in FAD has a D_{2h} symmetry [62, 59]. Table 4.5 compiles the geometrical parameters for the C_{2h} structure together with the barrier height for the HAT calculated as an energy difference between the D_{2h} and C_{2h} structures. The reference barrier was estimated at the CCSD(T)/aug-cc-pVTZ//MP2/aug-cc-pVTZ level of theory as $7.89 \text{ kcal mol}^{-1}$. At the MP2/aug-cc-pVXZ, X=2,3,4 level of theory one notices that the O...O and O-H distances at the minimum structure are shorter than the experimental values. Therefore, at these levels of theory, the strength of the H-bond has been overestimated which results in a barriers lower than the reference couple cluster value. In the second part of Table 4.5 the DFT results with the B3LYP functional and various basis sets are compiled. In particular, the performance of two basis sets, the B3LYP/6-31+G(d) and B3LYP/6-311++G(3df,3pd), were interesting since both sets have been used in previous quantum dynamical computations of the ground state tunneling splitting in FAD [18, 42]. There exists a large difference in the optimized geometries between these two sets. For instance, the two geometries differ in the O...O distance for 0.052 \AA and the corresponding barrier heights differ by more than $1.8 \text{ kcal mol}^{-1}$, being 8.37 and $6.51 \text{ kcal mol}^{-1}$ at the B3LYP/6-31+G(d) and B3LYP/6-311++G(3df,3pd) levels of theory. Interestingly, the B3LYP/6-31+G(d) value is very close to the reference coupled cluster barrier of $7.89 \text{ kcal mol}^{-1}$. However, taking into account the modest size of the basis set and an incomplete treatment of the electron correlation effects through the DFT functional such a good agreement with the coupled cluster result is most probable due to favourable cancellation of errors. The influence of a basis set superposition error (BSSE) on the DFT barriers and geometries was investigated by using the Boys and Bernardi counterpoise method [104, 105] as implemented in Gaussian package [67]. The values are presented in Table 4.5 and marked with an asterisk. Large basis set superposition errors (BSSE) have been found and shown to lower the energy barrier for 4.03 , 1.23 , 0.8 and 0.57 kcal/mol at the B3LYP/6-31G(d), 6-31+G(d), 6-31G(d,p) and 6-311++G(3df,3pd) levels, respectively. As expected the errors are larger in the case of small basis sets, and get smaller by using larger basis sets. Also, the corrected intramolecular distances (for instance O...O and O...H distances) are always longer than the corresponding uncorrected values. Once more, the difference is larger for small basis

Table 4.5: Comparison of calculated geometrical parameters (\AA and degrees) for FAD in the gas phase obtained at various levels of theory with experimental data [106, 107]. Energy barriers to HAT are given in kcal mol^{-1} . The values marked with an asterisk are the BSSE corrected values for the geometrical parameters and HAT barriers.

level of theory	O \cdots O	C-O _d	C-O _a	O-H	O \cdots H	O-C-O	C-O-H	O-H-O	ΔE
MP2/									
cc-pVDZ	2.677	1.318	1.228	1.001	1.676	126.8	108.4	179.9	7.38
cc-pVTZ	2.652	1.311	1.222	0.999	1.652	126.5	109.4	179.5	6.61
cc-pVQZ	2.659	1.309	1.219	0.997	1.662	126.4	109.6	179.9	6.94
aug-cc-pVDZ	2.685	1.326	1.233	1.001	1.683	126.3	109.2	179.7	7.76
aug-cc-pVTZ	2.660	1.313	1.224	1.000	1.660	126.3	109.5	179.9	6.71
aug-cc-pVQZ	2.660	1.310	1.220	0.998	1.662	126.3	109.6	179.6	6.88
6-311+G(d,p)	2.714	1.319	1.222	0.990	1.725	126.3	108.7	178.1	8.79
B3LYP/									
6-31 G(d)	2.698	1.314	1.224	1.005	1.694	126.8	110.2	178.7	7.71
*6-31 G(d)	2.728	1.318	1.222	1.003	1.726	126.5	109.7	179.1	3.68
6-31+G(d)	2.721	1.318	1.225	1.003	1.719	126.2	110.6	177.0	8.37
*6-31+G(d)	2.732	1.318	1.225	1.003	1.731	126.3	110.6	177.6	7.14
6-31 G(d,p)	2.650	1.310	1.226	1.007	1.642	126.7	110.5	178.9	5.41
*6-31 G(d,p)	2.679	1.314	1.227	1.005	1.675	126.2	110.9	177.9	4.61
6-311++G(3df,3pd)	2.669	1.308	1.217	1.001	1.668	126.3	110.9	178.4	6.51
*6-311++G(3df,3pd)	2.675	1.308	1.217	1.001	1.675	126.3	110.9	178.3	5.94
CCSD(T)/									
aug-cc-pVTZ	2.660	1.313	1.224	1.000	1.660	126.3	109.5	179.9	7.89
Exp.	2.696	1.320	1.217	1.033	1.72	126.2	108.8		

set. The intramolecular parameters are not affected by the BSSE.

Intrinsic reaction path calculation

The minimum energy path in mass-weighted Cartesian coordinates (Intrinsic Reaction Path (IRP)) for the intramolecular HAT reaction in FAD was traced at the B3LYP/6-31+G(d) and B3LYP/6-311++G(3df,3pd) levels of theory using the Gonzales-Schlegel second order algorithm [90] as implemented in Gamess package [68]. A step size of 0.1 bohr amu^{1/2} was used. The IRP connects the two equivalent C_{2h} structures a the D_{2h} structure. Figure 4.5 shows the variation of selected geometrical parameters along the IRP calculated at the B3LYP/6-311++G(3df,3pd) level of theory. As shown in Figure 4.5 the IRP could be divided in three fragments: in the first part ($-3.3 < s \leq -0.8$) the oxygen atoms move to bring the formic acid (FA) monomers closer together; in the second part ($-0.8 \leq s \leq 0.8$) the hydrogen atoms are transferred from the oxygen donors to oxygen acceptors. This part is also accompanied by exchange of the C-O donor to a C=O acceptor bonds and vice versa. In the third part ($0.8 \leq s < 3.3$) the formic acid (FA) monomers move apart. Furthermore, hydrogen transfer is accompanied with the wagging of the CO₂ groups in the FA monomers. In Figure 4.5 this is shown as a variation of an y coordinate of the FA monomer center of mass (y axis coincidence with

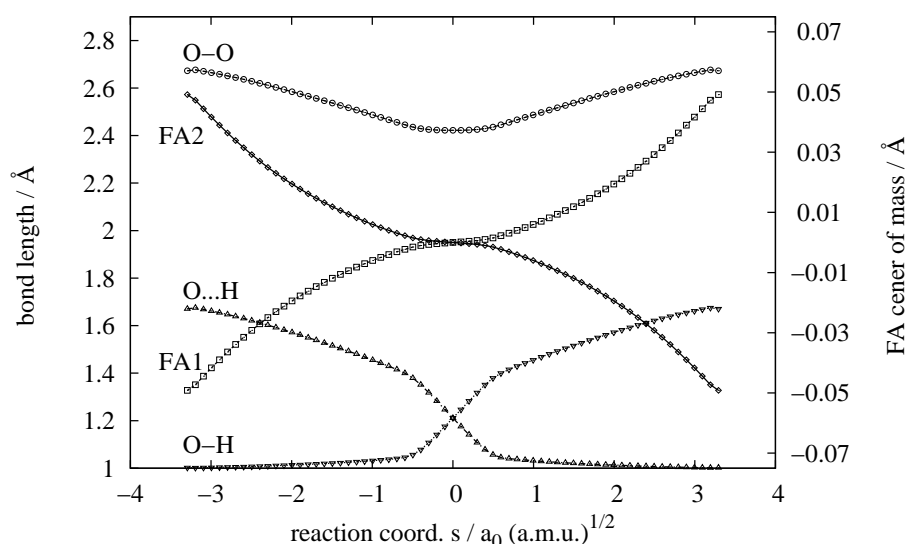


Figure 4.5: Left y axis: variations in geometrical parameters (in Å) along the IRP for the intramolecular H atom transfer in FAD (triangles and circles). Right y axis: variation in the center of mass of the formic acid (FA) fragments in the dimer (squares).

the b axis in Figure 3.1). At the transition state (D_{2h}) the y coordinate of the monomers center of mass is zero. Yet, during hydrogen transfer the monomers slide in opposite direction and the position of monomer center of mass changes for almost 0.05 \AA . These features of the IRP indicate that the HAT process in FAD can not be treated by a low dimensional dynamical model.

4.2 Normal mode based approaches

4.2.1 Acetylacetone

Perturbative approach

The harmonic frequencies of ACAC and its deuterated analogues calculated at MP2/6-311G(d,p) and B1LYP/6-311G(d,p) level of theory are presented in Tables 4.6 - 4.8. The anharmonic frequencies were calculated at the B1LYP/6-311G(d,p) level of theory by using the second-order perturbative approach of V. Barone [74, 75] as implemented in Gaussian 03 quantum chemical package [67] (see section 3.2.2). To the frequency with the highest intensity, a intensity of 100 has been assigned and all other intensities were expressed relative to it. To facilitate the comparison with previous studies, the assignment of the spectra according to the work of Tayyari et al. [29] was retained.

The largest anharmonicity in the IR spectrum of the **SYN**-ACAC conformer is observed for the OH-stretch fundamental. The harmonic frequency of the OH-stretch was calculated as 3192 cm^{-1} at the MP2/6-311G(d,p) level and as 3160 cm^{-1} at the B1LYP/6-311G(d,p) level of theory. The inclusion of anharmonic effects leads to a red shift of the OH-stretch frequency of 394 cm^{-1} i.e. to the value of 2766 cm^{-1} . The value of 2766 cm^{-1} is in good agreement with the experimental value of 2800 cm^{-1} for the OH band maximum. In the case of the ACAC deuterated analog in which the bridging hydrogen atom was deuterated (d2-ACAC in Table 4.7), the harmonic value of the OD stretching frequency was red shifted for 279 cm^{-1} to the value of 2027 cm^{-1} . Again, an excellent agreement with the experimental value is found. In the case of deuterated methyl hydrogens (d6-ACAC in Table 4.8) the anharmonic OH-stretch fundamental is located at 2680 cm^{-1} . This value is $\approx 80\text{ cm}^{-1}$ above the center of the experimental band. However, it should be noted that the OH-stretch band has a bandwidth of a few hundred wavenumbers and the experimental assignment of 2761 cm^{-1} is only approximative. On average, the deviation of the calculated anharmonic spectra from experiment is 0.96 % in the case of ACAC, 0.82 % in the case of d2-ACAC and 0.86 % in the case of d6-ACAC. Also, the presented harmonic intensities are comparable with the experimental values, the largest discrepancy being the one for the OH stretch fundamental in d6-ACAC.

The influence of the distal methyl group rotation on the vibrational spectra of ACAC was inspected by calculating the anharmonic vibrational frequencies of the **TS2** conformer of ACAC. The results are compiled in Table 4.9. The anharmonic OH stretch fundamental is red shifted from its harmonic value by more than 604 cm^{-1} and is located at 2487 cm^{-1} . The source of such a large anharmonic shift can be detected by inspection of the anharmonic correction matrix, χ_{ij} , (see Eq. (3.41)). Four modes mix strongly with

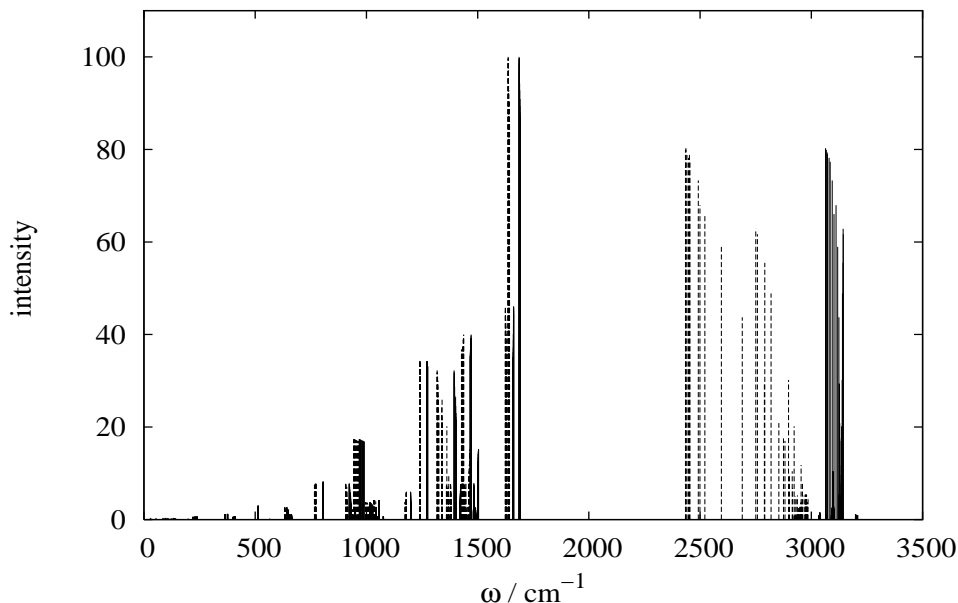


Figure 4.6: Harmonic (solid line) and anharmonic (dotted line) vibrational spectra of ACAC for various structures on the IRP for the distal methyl rotation.

the OH stretch (ν_6) and contribute to the red shift of the OH stretch fundamental. These are the C=C-C=O stretch + OH bend mode (ν_9) characterized by $\chi_{6,9}^{\text{TS2}} = -27.5 \text{ cm}^{-1}$, the C=O stretch + OH bend mode (ν_{10}) with $\chi_{6,10}^{\text{TS2}} = -33.8 \text{ cm}^{-1}$, the C=O stretch + C=C-C=O stretch + OH bend mode (ν_{18}) with $\chi_{6,18}^{\text{TS2}} = -52.8 \text{ cm}^{-1}$ and one low frequency mode the O...O stretching (ν_{34}) with $\chi_{6,34}^{\text{TS2}} = -10.0 \text{ cm}^{-1}$. Compared to the corresponding anharmonic frequency of the **SYN** conformer the anharmonic OH stretch fundamental of the **TS2** conformer is red shifted by 280 cm^{-1} . This large difference suggests that the extreme broadness of the OH stretching band may be caused by rotation of the distal methyl group and the coexistence of the different conformers of ACAC in the gas phase. In Figure 4.6 the harmonic (solid lines) and the anharmonic (dotted line) fundamental transitions of ACAC calculated for the **SYN**, **TS2** conformers and for a number of non-stationary points on the IRP for the rotation of the distal methyl group are shown. The intensities corresponding to different structures are scaled according to the Boltzmann distribution at 298.15 K. The inclusion of the anharmonic effects lead to the red shift of the OH stretch band by more than a 500 cm^{-1} . More importantly, the perturbational approach to the anharmonic spectra reproduced to a large extent the experimental bandwidth of the OH stretch. At this point it must be emphasized that a great care must be taken when interpreting the results of a perturbational approach. Namely, a large value for an anharmonic correction matrix element indicates a strong anharmonic coupling between a corresponding vibrational modes. In this case an approach in which a potential is approximated with the Taylor expansion which is truncated after the fourth order

is inadequate. However, a direct solution of the vibrational Schrödinger equation on a potential spanned by the corresponding normal modes could overcome the deficiency of a perturbational approach. The results of a reduced dimensionality approach and the comparison with the results of the perturbative approach will be given in the next section.

Next, the focus is on the 1700-1000 cm^{-1} region of the ACAC spectrum. As mentioned previously, it is the region of the enol ring modes. The harmonic analysis predicts five modes in this region made up from C=O, C-O, C=C, C-C stretchings and the OH in plane bending. In the C=O and C=C stretch region of the IR spectra of ACAC and d6-ACAC in the gas and liquid phase only a single band has been reported at $\approx 1620 \text{ cm}^{-1}$. However, two transitions are observed in the deconvoluted IR spectra of ACAC and d6-ACAC which were attributed to a superposition of (i) an asymmetric C=C-C=O stretch and OH in-plane bending at 1642 cm^{-1} and (ii) the C=O stretching coupled to OH in-plane bending at 1624 cm^{-1} (Table 4.6). At low temperatures the infrared spectrum of ACAC shows three distinct bands [56] (see also Figure 2.3) while only two components can be seen in the d2-ACAC spectrum at all temperatures. Based on their harmonic mode analysis Tayyari et al. [29] attributed these transitions to the coexistence of **TS2** and **SYN** conformers of ACAC. Namely, they attributed two higher frequency modes (at 1635 cm^{-1} and 1600 cm^{-1}) to the asymmetric C=C-C=O stretch + OH in plane bend of **SYN** and **TS2** conformers of ACAC and a lower frequency component (1575 cm^{-1}) to the C=O + O-H in-plane bending in both conformers. They also concluded that upon deuteration of the bridging hydrogen atom the position of the band at $\approx 1620 \text{ cm}^{-1}$ does not change considerably, while the band at around ≈ 1600 disappeared and a stronger band appeared at $\approx 1535 \text{ cm}^{-1}$. However, our anharmonic mode calculations reveal in this range two normal modes, the C=C-C=O stretch + OH in plane bend at 1650 cm^{-1} and C=O + O-H in-plane bend at 1625 cm^{-1} in **SYN** conformer, while in the **TS2** conformer the corresponding transitions have frequencies of 1644 cm^{-1} and 1628 cm^{-1} , respectively. The difference of only few wavenumbers in the corresponding transitions in two conformers is too small to explain the three maxima structure of the band. No other modes are close to this range, and combination bands are expected to be much weaker. Furthermore, at low temperatures the **TS1** conformer can also be disregarded. The provided pieces of information are difficult to reconcile with previous assignments and the three-maxima shape of the C=O stretch band will be further investigated using an approach which goes beyond the normal mode analysis and takes into account the large-amplitude motion of the transferring hydrogen.

The assignment of the frequencies in the 1200-1300 cm^{-1} region presents another problem. There are two bands in this region, one at $\approx 1300 \text{ cm}^{-1}$ which is strong in Ra-

man and weak in the infrared, and the other at 1250 cm^{-1} which is strong in the infrared and weak in Raman. Upon deuteration of the transferring hydrogen, the intensity of the band at $\approx 1300\text{ cm}^{-1}$ diminishes and a new band appears in the Raman spectrum of d2-ACAC. This band has not been observed in the liquid phase due to the overlap with one of the keto bands and was recognized after the deconvolution as a band at 1302 cm^{-1} . Also it has been observed in the rare gas matrices at 1288 cm^{-1} [55]. The strong Raman band was omitted from the normal mode analysis of ACAC spectra by Ogoshi and Nakamoto [28] and was assigned by Chiavassa et al. [55] to the C-O + C=O stretch and OH in-plane bend. Tayyari et al. [29] explained the strong Raman intensity of the band by attributing it to the symmetric O-C=C-O and C=O stretch which is strongly coupled to the OH in-plane bending mode. Our anharmonic calculation yielded a transition at 1345 cm^{-1} for the **SYN** conformer of ACAC (ν_{17} in Table 4.6) and 1318 cm^{-1} for the **TS2** conformer (ν_{18} in Table 4.9). Taking into account that transitions in the rare gas matrices are shifted downward in the comparison with the gas phase, the strong Raman line can be attributed to the O-C=C-O and C=O stretch + OH in-plane bend of the **TS2** conformer. In d2-ACAC this band disappears and a new band with a diminished Raman intensity appears at 1080 cm^{-1} . The band is attributed by Tayyari et al. [29] to the C=C stretch and in-plane OD bending which agrees well with our anharmonic calculations. The anharmonic frequency of the band in Table 4.6 is calculated as 1102 cm^{-1} . The band at 1250 cm^{-1} which is very strong in the infrared but weak in Raman is assigned by Ogoshi and Nakamoto to the C-C + C=C stretch [28] and by Chiavassa et al. to the C-C, C=C stretch and OH bend [55]. Our anharmonic results are in agreement with the conclusion of Tayyari et al. [29] that the band has a complicated character and was attributed to the symmetric C-C=C + symmetric C-CH₃ stretch and OH bend. The anharmonic frequency in both conformers is calculated as 1242 cm^{-1} which is in good agreement with the experimental value. Upon deuteration of the CH₃ groups the frequency of the band is blue shifted to 1260 cm^{-1} .

In conclusion, the perturbative approach to the vibrational spectroscopy succeeded in answering some of the main questions regarding the ACAC spectrum. The main features of the OH band, the assignments in the enol ring deformation region, and the nature of the band at 1250 cm^{-1} are well reproduced. What remains to be done is to understand additional broadening mechanisms of the OH band and the nature of the intermode couplings triggered by the hydrogen bond formation. These issues are investigated in detail in the next section.

-

Table 4.6: Vibrational frequencies (in cm^{-1}) of the SYN-ACAC conformer at the MP2/6-311G(d,p) and B1LYP/6-311G(d,p) levels of theory. Exp. data are taken from Ref. [29].

	Exp ^s	Int.	MP2 ^h	B1LYP ^h	Int.	B1LYP ^a	Mode
1	-	-	3258	3217	2	3101	ν CH _{olefi nic}
2	2800	br	3192	3160	85	2766	ν OH
3	3017	10	3206	3151	2	2991	ν_a CH ₃
4	3017	10	3202	3144	19	2935	ν_a CH ₃
5	2976	6	3166	3101	3	2961	ν_a CH ₃
6	2976	6	3164	3098	3	2988	ν_a CH ₃
7	2941	7	3085	3048	2	2944	ν_s CH ₃
8	2941	7	3080	3043	1	2952	ν_s CH ₃
9	1642	19	1716	1700	96	1650	ν_a C=C-C=O + δ OH
10	1624	77	1687	1660	100	1625	ν C=O + δ OH
11	1464	10	1512	1501	14	1464	δ_a CH ₃
12	-	-	1494	1485	2	1471	δ_a CH ₃
13	-	-	1491	1480	3	1460	δ_a CH ₃
14	-	-	1488	1479	3	1438	δ_a CH ₃
15	1427	17	1478	1468	47	1443	ν_a CC=CO + δ CH + δ OH + ν C-CH ₃
16	-	-	1416	1424	11	1380	δ_s CH ₃ + δ OH
17	-	-	1443	1402	29	1345	δ OH + ν C=O + ν_s C-C=C-O
18	1365	10	1397	1394	11	1369	δ_s CH ₃ + δ OH
19	1250	17	1292	1275	46	1243	ν_s C-C=C + δ OH + ν C-CH ₃
20	1171	6	1198	1199	5	1183	δ CH _{olefi nic}
21	-	-	1069	1072	1	1048	π CH ₃
22	-	-	1048	1052	3	1043	π CH ₃
23	1025	1	1043	1041	3	1023	ρ CH ₃
24	1000	4	1018	1013	4	1017	ρ CH ₃
25	952	10	962	968	25	954	γ OH
26	-	-	951	947	1	937	δ C-C=C + ν C-C + ρ CH ₃
27	913	9	929	921	11	922	ν C-CH ₃ + ν C-O
28	768	40	777	799	11	766	γ CH _{olefi nic}
29	-	-	627	653	-	653	Γ_{ring}
30	636	9	655	650	4	634	Δ_{ring}
31	-	-	537	556	-	566	Γ_{ring}
32	508	20	509	512	4	513	Δ_{ring}
33	397	s	393	398	1	412	Δ_{ring}
34	362	s	365	371	2	368	ν O...O
35	210	w	225	230	1	238	Γ_{ring} + γ C-CH ₃
36	-	-	183	182	-	177	Γ_{ring} τ CH ₃
37	-	-	150	154	-	152	τ CH ₃
38	120	w	113	121	1	125	τ CH ₃
39	-	-	51	23	-	not converged	τ CH ₃

Table 4.7: B1LYP/6-311G(d,p) vibrational frequencies (in cm^{-1}) of the d2-ACAC SYN conformer.

	Exp ^s	Int.	B1LYP ^h	Int.	B1LYP ^a	Mode
1	3018	w	3152	3	3015	ν_a CH ₃ (in-plane)
2	3018		3147	3	3000	ν_a CH ₃ (in-plane)
3	2970	w	3101	2	2961	ν_a CH ₃ (out-of-plane)
4	2970		3098	3	2988	ν_a CH ₃ (out-of-plane)
5	2940	w	3048	2	2943	ν_s CH ₃
6	2940		3043	1	2951	ν_s CH ₃
7	2300	w	2378	1	2299	ν CD _{olefi nic}
8	2027		2306	54	2027	ν OD
9	1633	vs	1689	63	1645	ν_a C=C-C=O
10	1544	vs	1582	100	1531	ν_s C=C-C=O + δ OD
11	1448		1488	21	1447	δ_a CH ₃ (in-plane)
12	-		1485	2	1472	δ_a CH ₃ (out-of-plane)
13	-		1479	2	1443	δ_a CH ₃ (out-of-plane)
14	1448	s	1474	9	1462	δ_a CH ₃ (in-plane)
15	1408	br	1433	9	1399	ν_a C-C=C-O
16	1365	s	1411	5	1383	δ_s CH ₃
17	1365		1391	13	1372	δ_s CH ₃
18	1273	vs	1308	32	1274	ν_s C-C=C-O
19	1082	m	1128	15	1102	δ OD + ν C=C + ρ CH ₃
20	-		1071	1	1047	π CH ₃
21	1025	m	1052	2	1043	π CH ₃
22	1025		1051	10	1038	ρ CH ₃ + δ OD
23	-		1013	2	1013	ρ CH ₃
24	936	m	949	6	940	ν C-CH ₃ + ρ CH ₃ + δ CD _{olefi nic}
25	880	w	893	4	891	ν C-O + δ C-C=C + ρ CH ₃
26	-		850	-	843	δ CD _{olefi nic}
27	707	ms	730	12	724	γ OD
28			654	-	640	Γ_{ring}
29	631	m	644	3	631	Δ_{ring}
30	-		573	5	565	γ CD _{olefi nic}
31	-		554	-	563	Γ_{ring}
32	498	m	503	3	504	Δ_{ring}
33	397	s	391	1	403	Δ_{ring}
34	362	s	364	2	364	ν O \cdots O
35	220	br	226	1	234	ν O \cdots O + δ C-CH ₃
36	-		180	-	175	Γ_{ring}
37	-		153	-	149	Γ_{ring}
38	120	br	119	1	126	τ CH ₃
39	-		23	-	not converged	τ CH ₃

Table 4.8: B1LYP/6-311G(d,p) vibrational frequencies (in cm^{-1}) of the d6-ACAC SYN conformer.

	Exp ^s	Int.	B1LYP ^h	Int.	B1LYP ^a	Mode
1	3098	-	3217	1	3090	ν CH _{olefi nic}
2	2761	4	3156	95	2680	ν OH
3	2265	2	2337	2	2260	ν_a CD ₃ (in-plane)
4	2265	2	2332	2	2250	ν_a CD ₃ (in-plane)
5	-	-	2294	2	2220	ν_a CD ₃ (out-of-plane)
6	-	-	2292	2	2229	ν_a CD ₃ (out-of-plane)
7	2103	-	2192	1	2108	ν_s CD ₃
8	2103	-	2187	-	2182	ν_s CD ₃
9	1628	100	1692	100	1645	ν_a C=C-C=O + δ OH
10	1606	100	1654	100	1611	ν C=O + δ OH
11	1446	36	1474	48	1447	ν_a C=C-C=O + δ OH + δ_s CH
12	1294	15	1406	32	1326	ν_s C=C-C=O + δ OH + ν C-O
13	1265	59	1287	56	1260	ν_s C-CD ₃ + ν_s C-C=C + δ OH
14	1185	21	1209	14	1194	δ CH _{olefi nic}
15	1075	2	1107	2	1090	δ CH _{olefi nic} + δ_a CD ₃
16	1051	-	1086	1	1073	δ_a CD ₃
17	1051	-	1071	1	1058	δ_s CD ₃
18	-	-	1068	4	1044	δ_a CD ₃
19	-	-	1066	2	1047	δ_a CD ₃
20	1036	2	1059	2	1050	δ_a CD ₃
21	952	3	970	28	953	γ OH
22	931	4	959	1	946	ν C-O + δ C-C=C + δ OH
23	-	-	925	1	911	ρ CD ₃
24	914	1	912	1	898	ρ CD ₃
25	904	3	889	1	875	ν_a C-CD ₃
26	812	5	828	3	817	ρ CD ₃
27	803	10	792	9	797	ρ CD ₃
28	763	3	793	4	759	γ CH _{olefi nic}
29	585	5	592	4	586	Δ_{ring}
30	-	-	573	-	574	Γ_{ring} + ρ CD ₃
31	492	3	489	-	495	Γ_{ring} + ρ CD ₃
32	477	10	480	4	480	Δ_{ring} + ρ CD ₃
33	360		361	1	372	Δ_{ring} + ρ CD ₃
34	337		350	2	341	ν O...O
35	212		208	1	213	Δ_{ring} + ρ CD ₃
36	-		167	-	166	Γ_{ring} + ρ CD ₃
37	-		136	-	140	Γ_{ring} + ρ CD ₃
38	-		95	-	87	τ CD ₃
39	-		17	-	not converged	τ CD ₃

Table 4.9: B1LYP/6-311G(d,p) vibrational frequencies (in cm^{-1}) of the TS2-ACAC conformer.

	B1LYP ^h	Int.	B1LYP ^a	Mode
1	3225	1	3098	ν CH _{olef nic}
2	3148	4	2997	ν_a CH ₃
3	3137	7	2987	ν_a CH ₃
4	3112	2	2984	ν_a CH ₃
5	3101	2	2961	ν_a CH ₃
6	3091	90	2487	ν OH
7	3051	1	2951	ν_s CH ₃
8	3048	1	2943	ν_s CH ₃
9	1691	100	1644	ν_a C=C-C=O + δ OH
10	1656	80	1628	ν C=O + δ OH
11	1506	15	1466	δ_a CH ₃
12	1492	1	1447	δ_a CH ₃
13	1482	3	1443	δ_a CH ₃
14	1479	2	1438	δ_a CH ₃
15	1470	44	1437	ν_a C-C=C-O + δ CH + δ OH + ν C-CH ₃
16	1421	5	1380	δ_s CH ₃ + δ OH
17	1402	9	1371	δ_s CH ₃ + δ OH
18	1393	37	1318	δ OH + ν C=O + ν_s C-C=C-O
19	1273	43	1242	ν_s C-C=C + δ OH + ν C-CH ₃
20	1199	7	1178	δ CH _{olef nic}
21	1073	1	1048	π CH ₃
22	1053	5	1031	π CH ₃
23	1040	2	1022	ρ CH ₃
24	1026	3	1008	ρ CH ₃
25	987	22	965	γ OH
26	953	2	939	δ C-C=C + ν C-C + ρ CH ₃
27	933	4	916	ν C-CH ₃ + ν C-O
28	799	9	758	γ CH _{olef nic}
29	665	-	657	Γ_{ring}
30	641	4	635	Δ_{ring}
31	562	-	561	Γ_{ring}
32	510	4	511	Δ_{ring}
33	406	1	405	Δ_{ring}
34	373	2	363	ν O...O
35	235	1	224	Γ_{ring} + γ C-CH ₃
36	182	-	176	Γ_{ring} τ CH ₃
37	153	-	146	τ CH ₃
38	122	-	106	τ CH ₃
39	54.492i	-	32.501i	τ CH ₃

Reduced dimensionality approach

The infrared spectrum of ACAC related to the OH \cdots O fragment was further investigated by using the normal mode representation of the Hamiltonian given by Eq (3.42) at the B1LYP/6-311G(d,p) level of theory. It was assumed that there is no total angular momentum and the Coriolis coupling present in the Watson Hamiltonian Eq. (3.21) was neglected. Four normal modes related to the OH \cdots O fragment of the **SYN** conformer ($\{Q_i^{\text{SYN}}\}$) and three corresponding normal modes of the **TS2** conformer ($\{Q_i^{\text{TS2}}\}$) were selected to span the PESs relevant for the O-H \cdots O fragment dynamics. Previous perturbative calculation confirmed the prediction that due to the low barrier to the distal methyl group rotation both conformers (**SYN** and **TS2**) leave a characteristic imprint in the IR spectrum of ACAC. For the **SYN** conformer the following modes were selected: the OH stretching $\nu_{\text{OH}}^{\text{SYN}}$ (ν_2 in Table 4.6 with the harmonic frequency of 3159 cm^{-1}), the in-plane bending mode $\delta_{\text{OH}}^{\text{SYN}}$ ($\nu_{17} = 1402\text{ cm}^{-1}$) and two low-frequency skeleton modes $\nu_{\text{O}\cdots\text{O}}^{\text{SYN}}$ ($\nu_{34} = 371\text{ cm}^{-1}$) and $\nu_{\text{OH}\cdots\text{O}}^{\text{SYN}}$ ($\nu_{35} = 230\text{ cm}^{-1}$). In Figure 4.7 the displacements of

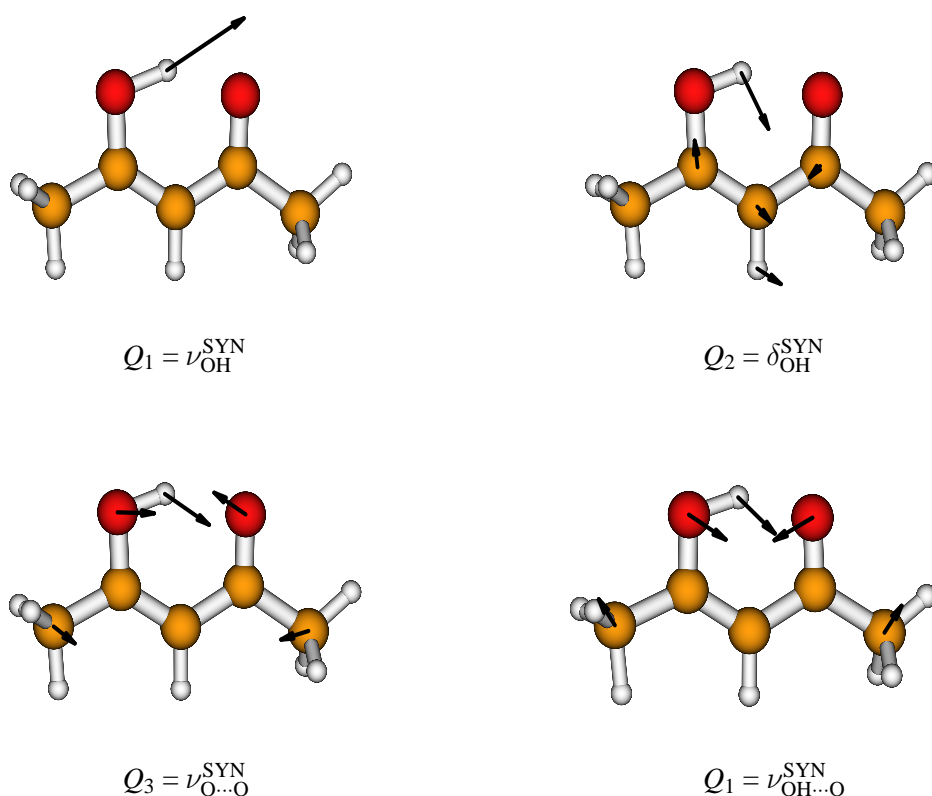


Figure 4.7: Normal mode displacement vectors of the **SYN** conformer. The four normal modes which span the 4D PES are: the OH stretching $\nu_{\text{OH}}^{\text{SYN}}$, the in-plane bending modes $\delta_{\text{OH}}^{\text{SYN}}$, and two low-frequency skeleton modes $\nu_{\text{O}\cdots\text{O}}^{\text{SYN}}$ and $\nu_{\text{OH}\cdots\text{O}}^{\text{SYN}}$.

the selected normal modes of the **SYN** conformer are shown. For the **TS2** conformer three normal modes were considered: the OH stretching $\nu_{\text{OH}}^{\text{TS2}}$ (ν_6 in Table 4.9 with the harmonic frequency of 3091 cm^{-1}), the in-plane bending mode $\delta_{\text{OH}}^{\text{TS2}}$ ($\nu_{18} = 1393 \text{ cm}^{-1}$) and the low-frequency mode $\nu_{\text{O}\dots\text{O}}^{\text{TS2}}$ ($\nu_{34} = 373 \text{ cm}^{-1}$).

The potential energy and dipole moment surfaces for the **SYN** and **TS2** conformers were calculated at the B1LYP/6-311G(d,p) level of theory on a $Q_1 \times Q_2 \times Q_3$ grid with the size $16 \times 12 \times 11$. For the **SYN** conformer the range was $-0.4 \text{ \AA} \leq Q_1^{\text{SYN}} \leq 0.75 \text{ \AA}$, $-0.7 \text{ \AA} \leq Q_2^{\text{SYN}} \leq 0.7 \text{ \AA}$ and $-1.6 \text{ \AA} \leq Q_3^{\text{SYN}} \leq 1.6 \text{ \AA}$. In the case of the **TS2** conformer the 3D surface was calculated in the range $-0.8 \text{ \AA} \leq Q_1^{\text{TS2}} \leq 0.4 \text{ \AA}$, $-0.6 \text{ \AA} \leq Q_2^{\text{TS2}} \leq 0.6 \text{ \AA}$ and $-1.5 \text{ \AA} \leq Q_3^{\text{TS2}} \leq 1.3 \text{ \AA}$. To construct the 4D surface for the **SYN** conformer the 3D surface was recalculated for 15 additional values in the Q_4^{SYN} direction. Depending on the shape of the potential, a variable step size of 0.02 and 0.04 \AA was used resulting in a computation of 31680 symmetry unique points. The large number of computed points allowed us to circumvent complicated analytical fits in favour of more accurate interpolation schemes. The calculated potential and dipole moment surfaces were interpolated using the weighted Shepard interpolation scheme as implemented by Renka [108] on a $16(32) \times 16 \times 16 \times 16$ grid in the case of the **SYN** conformer and on a $32 \times 32 \times 32$ grid in the case of a **TS2** conformer.

Figure 4.8 presents six different two-dimensional cuts of the 4D **SYN** and 3D **TS2** PES. In both PESs the strong anharmonicity of the potential in the direction of the OH stretching mode is visible. Also, in both cases the OH stretching mode mixes strongly with the low frequency modes. In the **TS2** conformer there is also a pronounced coupling with the bending mode.

The vibrational Schrödinger equation for the fully coupled potentials was solved using the Fourier grid Hamiltonian approach [83] combined with the implicitly restarted Lanczos diagonalization method [109] implemented in the ARPACK suits of programs [110, 111]. To construct the Hamiltonian in Eq. (3.42) the following reduced masses in atomic units were used: $\mu_{Q_1}^{\text{SYN}} = 0.928$, $\mu_{Q_2}^{\text{SYN}} = 0.540$, $\mu_{Q_3}^{\text{SYN}} = 0.2473$, $\mu_{Q_4}^{\text{SYN}} = 0.302$ and $\mu_{Q_1}^{\text{TS2}} = 0.932$, $\mu_{Q_2}^{\text{TS2}} = 0.417$, $\mu_{Q_3}^{\text{TS2}} = 0.25$. These values were obtained from the *ab initio* calculations according to the normalization factors defined in the Eq. (3.43).

The IR absorption spectrum from an initial state Ψ_i to a final state Ψ_f was calculated as [112]:

$$I_i(\omega) = \sum_{\alpha=x,y,z} \sum_f \omega_{fi} \left| \int d\mathbf{Q} \Psi_f(\mathbf{Q}) d^\alpha(\mathbf{Q}) \Psi_i(\mathbf{q}) \right|^2 \delta(\omega - \omega_{fi}), \quad (4.1)$$

where $\omega = \omega_{fi}$ is the transition frequency and $d^\alpha(\mathbf{Q})$ are the Cartesian components of the dipole moment operator. The system is in the x - y plane, and the z -axis is perpendicular.

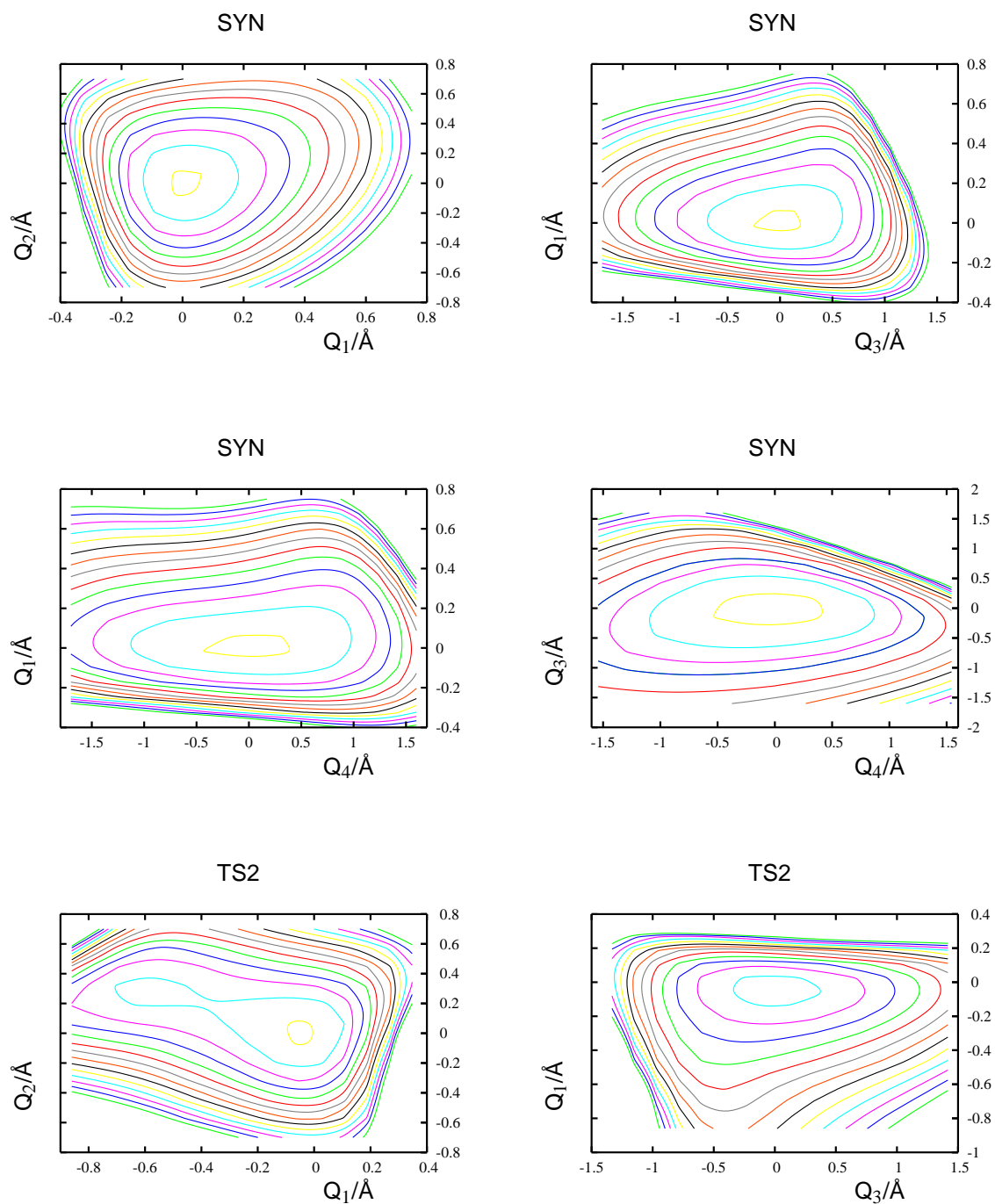


Figure 4.8: 2D projections of the potential energy surfaces (PESs) of **SYN** and **TS2**. The contours are spaced by 1600 cm^{-1} , and the most inner contour corresponds to an energy value of 800 cm^{-1} above the minimum.

Obviously, the spectrum has no contribution in the z -direction for none of the out-of-plane modes were included.

Figure 4.9 displays the spectra calculated using the reduced space normal mode approach on the 4D $V(Q_1, \dots, Q_4)$ PES for the **SYN** conformer and on the 3D $V(Q_1, Q_2, Q_3)$ PES for the **TS2** conformer. The upper panel shows the computed spectrum of the **SYN** conformer and the lower panel shows the spectrum of the **TS2** conformer. The transitions from the ground state (I_0) are shown in black, while hot transitions, i.e. those starting from the vibrationally excited $\nu_{\text{OH}\dots\text{O}}$ and $\nu_{\text{O}\dots\text{O}}$ modes are shown by dashed lines. A temperature of 297 K was assumed. The assignment of the spectra in terms of uncoupled modes were performed according to the Eq. (3.45). The frequencies of the transitions together with the coefficients for the decomposition in terms of zero-order states are compiled in Table 4.10.

By inspecting the coefficients of the zero order states in Table 4.10, one can conclude that the lines at 227 and 363 cm^{-1} correspond to the $\nu_{\text{OH}\dots\text{O}}^{\text{SYN}}$ and $\nu_{\text{O}\dots\text{O}}^{\text{SYN}}$ modes. Both fundamentals are in very good agreement with the observed in-plane ring deformation modes at 230 and 364 cm^{-1} . The calculated $\nu_{\text{O}\dots\text{O}}^{\text{TS2}}$ frequency is 349 cm^{-1} , but compared

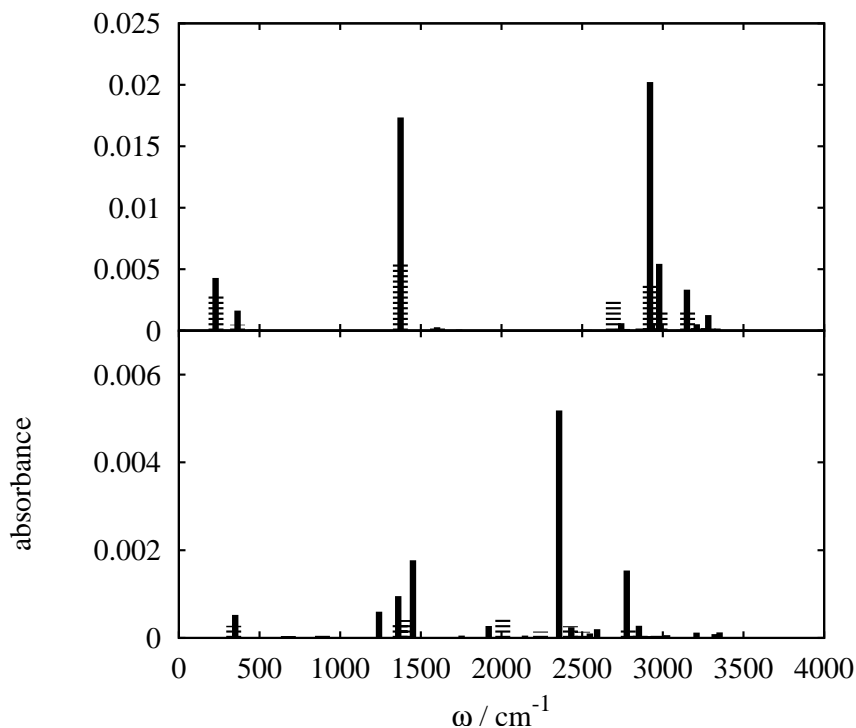


Figure 4.9: IR stick spectra of ACAC **SYN** (upper panel) and **TS2** (lower panel) conformers at $T=297$ K. Transitions from the ground state are shown in black, hot transitions from $\nu_{\text{OH}\dots\text{O}}$ and $\nu_{\text{O}\dots\text{O}}$ are shown in grey.

Table 4.10: Coefficients of the zero order states (Eq. (3.45)) of those states corresponding to the strongest transitions in the OH-stretch bands of the **SYN** and **TS2** ACAC. The results are obtained in the normal mode representation.

SYN							TS2					
f	ω/cm^{-1}	N_{Q1}	N_{Q2}	N_{Q3}	N_{Q4}	c_{if}	f	ω/cm^{-1}	N_{Q1}	N_{Q2}	N_{Q3}	c_{if}
1	228	0	0	0	1	0.947	1	349	0	0	1	-0.867
2	364	0	0	1	0	0.959	4	1240	0	1	0	0.632
16	1375	0	1	0	0	-0.958			0	0	3	0.328
		0	1	0	1	0.213			0	1	1	0.292
63	2742	0	2	0	0	-0.914	5	1360	0	1	0	-0.433
		0	2	0	1	0.260			0	0	3	0.559
70	2920	1	0	0	0	0.614			0	0	4	0.399
		1	0	0	1	-0.412			0	0	5	0.299
		1	0	0	2	0.216	6	1451	0	1	0	-0.549
		0	2	0	0	0.275			0	0	4	-0.453
		0	2	0	1	0.275			0	0	5	-0.262
		1	0	1	0	-0.249	9	1920	0	0	5	0.403
74	2977	0	2	0	0	-0.207			0	1	2	-0.314
		0	2	0	1	-0.792			0	1	3	-0.252
		0	2	0	2	0.304	12	2357	1	0	0	0.539
		1	0	0	0	0.356			1	0	1	0.418
83	3149	1	0	0	0	-0.431			1	0	2	0.230
		1	0	0	1	-0.355	16	2776	0	2	0	0.680
		1	0	0	2	0.419			0	2	1	0.290
		1	0	0	3	-0.252						
		0	2	0	1	-0.216						
		0	2	0	2	-0.253						
89	3210	0	2	0	1	-0.300						
		0	2	0	2	-0.720						
		0	2	0	3	0.294						
		1	0	0	0	0.205						
		1	0	0	1	0.289						
		1	0	0	2	-0.212						
91	3281	0	2	1	0	-0.241						
		0	2	1	1	-0.251						
		1	0	0	0	-0.321						
		1	0	1	0	-0.485						
		1	0	1	1	0.344						
		1	0	2	0	0.307						
		1	0	2	1	-0.206						

to $\nu_{O\dots O}^{SYN}$ it has a negligible intensity¹.

The fundamental transition of the in-plane bending mode of the **SYN** conformer, δ_{OH}^{SYN} , is located at 1375 cm^{-1} . The value is red shifted from the harmonic frequency (1402 cm^{-1}) by only 27 cm^{-1} . Compared to the anharmonic frequency resulting from the perturbative approach the frequency value of 1375 cm^{-1} is larger than the perturbative value for 30 cm^{-1} . The difference can be explained by inspection of the anharmonic correction matrix elements, χ_{ij} (Eq. (3.41)). Indeed, the δ_{OH}^{SYN} strongly couples with the ν_{OH}^{SYN} mode ($\chi_{2,17}^{SYN} = -24.03\text{ cm}^{-1}$) and this coupling was included in the treatment. But additionally, it couples with the other in-plane and out-of-plane bending modes ν_9 (OH-bend + C=C-C=O stretch), ν_{10} (OH bend + C=O stretch), ν_{18} (OH bend + CH₃ bend) and ν_{25} (OH out-of-plane bend) and the inclusion of these modes in the reduced dimensionality treatment would induce further red shift of the frequency which would result in a better agreement with the observed value. Concerning the in-plane OH bending mode of the **TS2** conformer, the fundamental transition is located at 1360 cm^{-1} . It can be seen that the transition gains in intensity and develops a double-maxima structure due to a resonance with the $\nu_{O\dots O}^{SYN}$ overtone. The remaining $\approx 50\text{ cm}^{-1}$ discrepancy between the calculated and observed δ_{OH} (1298 cm^{-1}) cannot be, obviously, attributed to the couplings triggered by the hydrogen bond formation. The δ_{OH}^{TS2} anharmonic frequency of 1318 cm^{-1} (see Table 4.9) calculated using the perturbative treatment is in good agreement with the experiment and the anharmonic correction matrix (χ_{ij}) again reveals the source of the anharmonicity shift. Again, the δ_{OH}^{TS2} couples strongly with the ν_{OH}^{TS2} mode ($\chi_{6,18} = -52.8\text{ cm}^{-1}$). Furthermore, the additional red shift of the δ_{OH}^{TS2} mode is due to the mixing with two other modes containing the OH bending contribution: the OH-bend/asymmetric C=C-C=O stretch mode (ν_9) characterized with $\chi_{18,9}^{TS2} = -10.0\text{ cm}^{-1}$ and the OH-bend/symmetric C=O stretch (ν_{10}) with $\chi_{18,10}^{TS2} = -15.0\text{ cm}^{-1}$. Consequently, the assignation of the transition at 1298 cm^{-1} to the δ_{OH}^{TS2} mode, made on the basis of the perturbative approach is confirmed.

In the following, the focus will be on the OH stretch region of the ACAC spectrum. According to the Table 4.10 the most relevant transitions in the ν_{OH} stretching region, i.e. between 2900 and 3500 cm^{-1} , decompose into *all* zero-order states for both conformers. Therefore, it is not possible to identify any transition of the ν_{OH} band as a fundamental transition. The fact that the ν_{OH}^{SYN} and ν_{OH}^{TS2} fundamentals are distributed in several states of the OH-stretch band leads to well know difficulties in assignments of the OH-stretch band. This is an important consequence of the strong anharmonic mode mixing induced by the hydrogen bond formation. Another consequence is the break-down of the vibrational selection rule which implies a change of the vibrational quantum numbers by

¹For the low frequency part of the experimental spectrum refer to the article of Ogoshi et al.[28].

one. For example, a hot transition of the in plane bending mode starting from the $\nu_{O\dots O}$ mode $((0,0,0,1) \rightarrow (0,1,0,1))$ occurs at the same frequency as the fundamental transition $((0,0,0,0) \rightarrow (0,1,0,0))$, but in the OH stretch region the transitions starting from $(0,0,0,1)$ (grey bars) are shifted by the amount of the initial excitation.

The OH stretch band in the **SYN** conformer is dominated by a closely spaced doublet located at 2920 cm^{-1} and 2977 cm^{-1} with resonance enhanced intensities (see the experimental spectrum in Figure 4.10). Inspecting the coefficients of the zero order states from Table 4.10, one can conclude that the underlying dynamics is more complex than what a Fermi resonance would suggest. For instance, the transition at 2977 cm^{-1} contains the excitation of the OH-bending and OH-stretching modes, but at the same time a noticeable excitation in the low frequency $\nu_{O\dots O}$ mode. The same is valid for the Franck-Condon type vibrational progression observed within the ν_{OH}^{SYN} band. Although the energy differences between the transitions with the frequencies 3149 and 2920 cm^{-1} and between the transition with the frequencies 3281 and 2920 cm^{-1} (Table 4.10) match exactly the frequencies of the $\nu_{OH\dots O}^{SYN}$ and $\nu_{O\dots O}^{SYN}$ modes, the zero order states analysis reveals a much more complicated dynamics. Consequently, an interpretation in terms of combination transitions like $\delta_{OH} + N\delta_{O\dots O} + M\delta_{OH\dots O}$ is an oversimplified view of O-H \cdots O fragment dynamics.

The strongest transition in the OH stretch region of the **TS2** conformer is located at 2357 cm^{-1} . Compared to the corresponding transition of the **SYN** conformer, it is red shifted by more than a 500 cm^{-1} . The transition is also red shifted by 130 cm^{-1} with respect to the anharmonic value calculated by using the perturbative approach (Table 4.9). These observations confirm the previous conclusion that both enol conformers of ACAC (**SYN** and **TS2**) contribute to the formation of the broad OH stretch band. Due to the particular choice of normal modes which span the 3D PES, there is no evidence for Fermi resonance interactions in the OH stretch band. Namely, for consistency reasons the 4D and 3D PESs of the **SYN** and **TS2** conformers were spanned by an analogous set of modes, but in **TS2** the frequency difference between δ_{OH}^{TS2} and ν_{OH}^{TS2} prevents a resonance interaction. Instead, inspection of the Table 4.9 reveals a possible Fermi resonance of the OH stretch with ν_{19} mode (OH bend + C-C=C stretch) at 1242 cm^{-1} which will contribute to build up intensities around 2500 cm^{-1} .

Finally, Figure 4.10 displays the experimental gas phase IR spectrum [32] in comparison with the summed up spectrum of the **SYN** and **TS2** conformers. The IR intensities of the calculated spectra were rescaled in order to facilitate the comparison with the experimental spectrum [32]. By comparing the computed and the experimental spectra, one can see that the two computed maxima coincide within few wavenumbers with the experimental peaks. In addition the structure of the band is well reproduced. However,

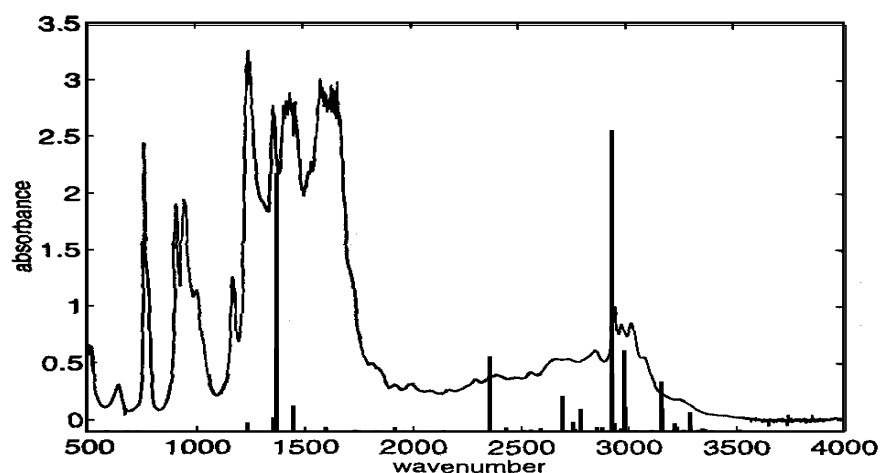


Figure 4.10: The computed IR spectrum of both conformers at $T=297$ K superimposed on the experimental gas phase spectrum (courtesy of J. Mavri and J. Grdadolnik) [32]. The computed intensities have been rescaled in order to facilitate comparison with experiment.

an important difference lies in the intensities and in the width of the bands. Namely, the IR spectrum of ACAC displays a very broad ν_{OH} band starting from 1800 cm^{-1} while the computed spectrum does not contain transitions of noticeable intensity below 2357 cm^{-1} . This could be improved by the extension of the model 4D system, for example by including the symmetric and asymmetric C=O stretch motion which will increase the number of transitions and, to a certain extent, will modify the band shape. However, examination of the energies of the C=O fundamentals given in Table 4.9 indicates that changes are expected on the high frequency side of the band, i.e., in the region where the Fermi resonance condition is fulfilled.

The spectrum of the *enol*-ACAC shown in Figure 4.9 represents the best result achieved under the single well, normal mode approximation. The overall agreement with experiment appears to be quite satisfactory, yet the inclusion of the hydrogen atom tunneling motion is needed since the double well hydrogen motion should leave a mark in the IR spectrum of the molecule. Evidence of tunneling, according to the reaction path calculations, are most likely to show up in the spectrum of **TS2** conformer as the HAT reaction takes place only after the methyl groups have reached an eclipsed conformation. Therefore, a large amplitude treatment will be further employed to investigate the spectrum of the **TS2** conformer.

4.2.2 The formic acid dimer

This subsection explores the most intriguing feature of the IR spectrum of FAD by combining a perturbative treatment in full dimensionality and a non-perturbative treatment in reduced dimensionality. The antisymmetric OH stretching band (b_u) in FAD is the dominant feature in the spectrum for it spreads over more than 500 cm^{-1} around its maximum which is located at 3110 cm^{-1} [113]. The band also exhibits a rich substructure that reflects strong anharmonic couplings. Much of the earlier theoretical work was concerned with the source of the antisymmetric OH stretch band broadening and its rich sub-structure in carboxylic acid dimers like FAD or parent acetic acid dimer (AAD) and benzoic acid dimer (BAD) [114, 25, 115]. Recently, Blaise et al. [114] proposed a general theoretical approach for treating the ν_{OH} line shape and applied it to the cyclic dimers $(\text{CD}_3\text{CO}_2\text{H})_2$ and $(\text{CD}_3\text{CO}_2\text{D})_2$ in the gas phase. In their model the adiabatic approximation which allows to separate the fast O-H motion and the slow O-H...O motion was used. Subsequently, a nonadiabatic correction is introduced via a resonant exchange between the excited states of the monomer fast modes. Using a restricted number of fitted parameters the authors could reproduce the experimental ν_{OH} line shape. Florio et al. [25] calculated the spectra of FAD and BAD allowing for the cubic couplings between the interdimer stretch, antisymmetric OH stretch and symmetric and antisymmetric OH bend. For FAD a calculation of the vibrational spectrum using the full cubic force field was also done. While for BAD the agreement with the experiment was very good, for FAD only a semiquantitative agreement was obtained pointing to possible differences in the couplings that shape the OH band in the two compounds. Dreyer [115] used the sixth order force field to explain the line shape of the O-H stretching band in AAD. Anharmonic couplings of the OH stretch mode to low frequency modes and mid-infrared fingerprint modes were included resulting in a eleven-dimensional model. The results were in agreement with the experiment, but the OH stretching frequency had to be scaled by factor 0.98 to account for the global red shift of the band. Unfortunately, in both numerical works the interaction with the IR inactive symmetric OH stretch, i.e., the mode leading to the Davydov coupling put forward by Blaise et al. was not taken into account.

Perturbative approach

The harmonic frequencies for the C_{2h} structure of FAD were calculated using the B3LYP functional with different basis sets. The corresponding anharmonic frequencies were computed at the same level of theory using the second order perturbative approach [74, 75] as implemented in the Gaussian 03 quantum chemical package [67]. The

Table 4.11: Experimental data taken from Ref. [25] and theoretical, harmonic and anharmonic frequencies (in cm^{-1}) for three basis sets. For easier comparison the numeration of Ref. [25] is retained.

			B3LYP		B3LYP		B3LYP		
Mode			Exp.	6-31G(d)	6-31+G(d)	6-31 G(d,p)			
1	b_u	νOH	3110	3218	2925	3245	2964	3157	2777
2	a_g	νCH	2949	3113	2891	3118	2934	3092	2921
3	b_u	νCH	2957	3098	2917	3113	2931	3075	2879
4	a_g	νOH	-	3100	2815	3153	2843	3013	2593
5	b_u	$\nu\text{C=O}$	1754	1814	1773	1785	1746	1807	1765
6	a_g	$\nu\text{C=O}$	1670	1744	1694	1721	1675	1727	1670
7	a_g	δOH	1415	1490	1448	1459	1417	1503	1449
8	b_u	δOH	-	1456	1415	1441	1398	1459	1443
9	a_g	δCH	1375	1424	1389	1404	1370	1421	1388
10	b_u	δCH	1362	1417	1383	1397	1361	1417	1387
11	b_u	$\nu\text{C-O}$	1218	1270	1247	1255	1226	1283	1263
12	a_g	$\nu\text{C-O}$	1214	1271	1244	1254	1225	1284	1260
13	a_u	γCH	1060	1098	1070	1090	1055	1110	1080
14	b_g	γCH	1050	1075	1054	1070	1044	1080	1058
15	a_u	πOH	917	976	947	983	947	1004	979
16	b_g	πOH	-	955	921	956	910	991	963
17	b_u	δCO_2	699	718	712	703	696	728	725
18	a_g	δCO_2	677	686	677	677	672	690	683
19	b_u	dimer in-plane rock	248	285	278	269	258	288	291
20	b_g	dimer out-of-plane rock	230	275	264	257	241	281	271
21	a_g	dimer stretch	190	217	204	210	199	210	201
22	a_u	dimer out-of-plane wag	163	182	180	182	169	190	187
23	a_g	dimer in-plane rock	137	178	170	170	162	179	172
24	a_u	dimer twist	68	76	72	77	73	79	75

resulting harmonic and anharmonic normal mode frequencies are compiled in Table 4.11. The deviation of the calculated anharmonic frequencies in the middle and the high frequency part of the spectrum from the experimental values is below 0.5 % at the B3LYP/6-31+G(d) level of theory, 1.5 % at the B3LYP/6-31G(d) and 2 % at the B3LYP/6-31G(d,p) level. The best agreement with the experiment is found for the 6-31+G(d) basis set. In the middle part of the spectrum, the largest deviation from the experimental values is found for the antisymmetric out-of-plane bending (π_{OH}) having a discrepancy of more than 3% in all the three cases. The harmonic π_{OH} frequencies of 976, 983 and 1004 cm^{-1} obtained for the three small basis sets compare well with the values computed with larger basis sets. For instance, at the B3LYP/aug-cc-pVTZ the π_{OH} fundamental is found at 1002 cm^{-1} and at the MP2/aug-cc-pVTZ at the 995 cm^{-1} . Although it is expected that the anharmonic frequencies converge much faster than the harmonic value, the harmonic frequencies indicate that the discrepancy between the experimental value of 917 cm^{-1} and the computed anharmonic frequencies cannot be attributed to basis set effects. Inspection of the anharmonic correction matrix reveals coupling to four vibration modes: the dimer out-of-plane rock, $\chi_{15,20} = -7.0 \text{ cm}^{-1}$, and the dimer stretch, $\chi_{15,21} = -9.0 \text{ cm}^{-1}$ induce red-shifts of the π_{OH} frequency, while the two OH stretching modes coupled by $\chi_{15,1} = 17.8 \text{ cm}^{-1}$ and $\chi_{15,4} = 26.8 \text{ cm}^{-1}$ induce blue-shifts of the mode frequency. An analysis beyond the second order perturbation treatment for this modes is therefore needed in order to obtain a better insight in their couplings and to reproduce the better agreement with the experimental value.

The jet-cooled IR spectrum reveals that the maximum of the b_u antisymmetric OH stretching band (ν_{OH}) is at 3110 cm^{-1} [113]. The anharmonic ν_{OH} (b_u) frequency is red shifted by 293, 281 and 380 cm^{-1} from its harmonic value at the B3LYP/6-31G(d), B3LYP/6-31+G(d) and B3LYP/6-31G(d,p) levels of theory, respectively. For the OH stretching band such large red-shift is expected, but compared to the observed band center frequency the anharmonic results are clearly too red-shifted. One may argue that the harmonic frequencies obtained with such small basis sets are not converged and the MP2/aug-cc-pVTZ harmonic frequency of 3305 cm^{-1} supports this observation. However one should also take into account that the second order perturbative approach does not account for the wholeness of interactions shaping the ν_{OH} (b_u) band. Inspection of the anharmonic correction matrix (χ_{ij}) reveals that the dominant contribution to the shift of the ν_{OH} band comes from the coupling of the antisymmetric OH stretching to the symmetric IR inactive OH stretching. The interaction is characterized by anharmonic constants of $\chi_{1,2} = -221, -345, -407 \text{ cm}^{-1}$ with the 6-31G(d), 6-31+G(d) and 6-31G(d,p) basis sets, respectively. Diagonal anharmonic terms are smaller and range between -89 and -99 cm^{-1} . Couplings to low frequency modes are also small, but positive. The

largest coupling is found for the dimer stretch, $\chi_{1,21}$, ranging between 34 and 54 cm^{-1} . The interactions with the fingerprint modes $\nu_{\text{C=O}}$, δ_{OH} , and $\nu_{\text{C-O}}$ are even smaller, negative for $\nu_{\text{C=O}}$, and positive for the other four combinations.

According to Eq. (3.41) the perturbative approach approximates the potential by a truncated Taylor expansion which takes into account the diagonal and semi-diagonal quartic force constants. This approximation is inadequate for strong anharmonicities [79] as it is the case with the interactions that shape the antisymmetric OH stretch band in FAD. However, the direct solution of the vibrational Schrödinger equation on a potential spanned by the chosen normal modes could overcome the insufficiencies posed by the perturbative approach and allow to identify the hierarchy of interactions that shape the OH stretch band.

Reduced dimensionality approach

The ν_{OH} stretch band of the FAD was further investigated by using two and three-dimensional PESs spanned by combinations of several normal modes. All the constructed potentials included the antisymmetric O-H stretching, $\nu_{\text{OH}}(b_u)$ and one or two of the following modes: the symmetric O-H stretch, $\nu_{\text{OH}}(a_g)$, the symmetric and antisymmetric C=O and C-O stretches $\nu_{\text{C=O}}(a_g)$, $\nu_{\text{C=O}}(b_u)$, $\nu_{\text{C-O}}(a_g)$, $\nu_{\text{C-O}}(b_u)$ and two in-plane bendings, $\delta_{\text{OH}}(a_g)$ and $\delta_{\text{OH}}(b_u)$. In the low frequency part of the spectrum the dimer stretch (a_g) and the symmetric and antisymmetric in-plane rocks were included. The potential and dipole moment surfaces were calculated at the B3LYP/6-31+G(d) level of theory on a direct product grid with spacings 0.05 Å for ν_{OH} and $\nu_{\text{C=O}}$, 0.1 Å for δ_{OH} and $\nu_{\text{C-O}}$ and 0.2 Å for the low frequency modes. The calculated potential and dipole moment surfaces were further interpolated using the weighted Shepard interpolation scheme as implemented by Renka [108] on 81×81 and $45 \times 81 \times 81$ grids. The vibrational Schrödinger equation for the fully coupled potentials was solved using the Fourier grid Hamiltonian approach [83] combined with the implicitly restarted Lanczos diagonalization method [109] implemented in the ARPACK suits of programs [110, 111]. The procedure is analogue to the one described in the section 4.2.1 for ACAC. To construct the Hamiltonian (Eq. (3.42)) reduced masses in atomic units μ as given in Table 4.12 were used. The values were obtained from the Gaussian normal mode analysis.

According to perturbation theory, the dominant contribution to the red shift of the $\nu_{\text{OH}}(b_u)$ band arises from the coupling between the antisymmetric OH-stretch (Q_1) and symmetric OH-stretch (Q_2). The 2D potential spanned by the antisymmetric and symmetric OH-stretch were computed at the B3LYP/6-31+G(d), B3LYP/6-31G(d) and B3LYP/6-31G(d,p) levels of theory and the corresponding time-independent equations were solved. Figure 4.11 shows the $V(Q_1, Q_2)$ potential calculated at the B3LYP/6-31+G(d) level of

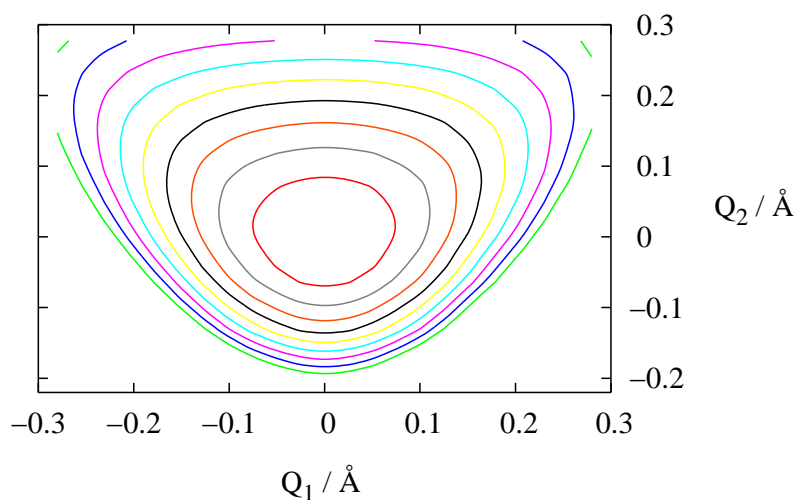


Figure 4.11: Two-dimensional potential energy surface spanned by the antisymmetric (Q_1) and symmetric (Q_2) OH stretching vibrations of FAD computed at B3LYP/6-31+G(d) level of theory. The contour spacing is 1000 cm^{-1} .

theory. The isoenergy contours are spaced by 1000 cm^{-1} . The triangular shape of the potential clearly shows the strong anharmonic coupling between the antisymmetric and symmetric OH-stretch and in the same time indicates that the stretchings of individual O-H bonds are energetically favourable. This type of interaction is known as the Davydov coupling and indicates a strong resonance interaction between two degenerate OH stretching vibrations of the monomer units (q_1, q_2) that couple and split into two OH stretching normal modes of the dimer (Q_1, Q_2) (see also Figure 4.12):

$$Q_1 = \frac{1}{\sqrt{2}}(q_1 - q_2); \quad Q_2 = \frac{1}{\sqrt{2}}(q_1 + q_2)$$

Using the 2D potential calculated at the B3LYP/6-31+G(d) level of theory the frequencies of the symmetric $\nu_{\text{OH}}(a_g)$ and antisymmetric $\nu_{\text{OH}}(b_u)$ modes were calculated as 3076

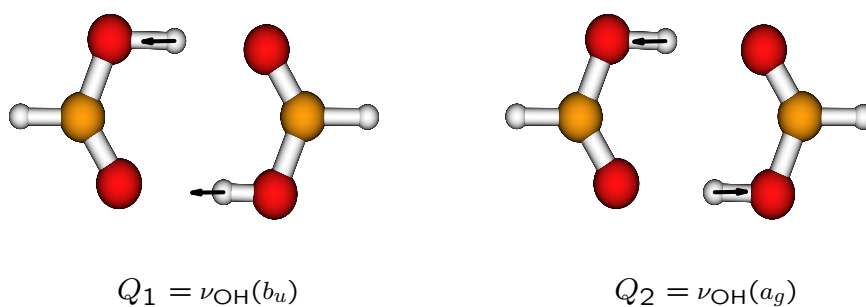


Figure 4.12: Antisymmetric (Q_1) and symmetric (Q_2) OH stretching mode of the formic acid dimer. Only the most relevant displacements are shown.

cm^{-1} and 3090 cm^{-1} , resulting in a splitting of only 14 cm^{-1} . The calculated $\nu_{\text{OH}}(b_u)$ frequency is red shifted by 169 cm^{-1} from its harmonic value. The symmetric $\nu_{\text{OH}}(a_g)$ band is IR inactive which is reflected in the intensity of the calculated fundamental transition that is for two orders of magnitude smaller than the intensity for the $\nu_{\text{OH}}(b_u)$ fundamental. At the B3LYP/6-31G(d) level of theory the two corresponding transitions are found at 3134 cm^{-1} and 3139 cm^{-1} , and at the B3LYP/6-31G(d,p) level of theory at 2957 cm^{-1} and 3009 cm^{-1} . The frequency splitting between the two OH stretch transitions are 5 cm^{-1} and 50 cm^{-1} at the B3LYP/6-31G(d) and B3LYP/6-31G(d,p) level of theory indicating the large difference in the barrier height for the HAT at three levels of theory. At the B3LYP/6-31G(d,p) level of theory the lowest barrier height is obtained ($\Delta E = 5.41 \text{ kcal mol}^{-1}$ in Table 4.5) and correspondingly the largest interaction of the two OH stretching modes is found, and the largest difference between the OH stretchings is obtained.

To investigate other possible interactions that shape the $\nu_{\text{OH}}(b_u)$ band, like Fermi resonances with fingerprint vibrations and couplings with low frequency modes, a series of three-dimensional potentials were generated and the corresponding eigenvalue problems were solved. The results are compiled in Table 4.12. From the value of the $\nu_{\text{OH}}(b_u)$ frequency in Table 4.12 it can be seen that none of the interactions with the $\nu_{\text{OH}}(b_u)$ mode alone lead to the red shift. On the contrary, the interaction of the $\nu_{\text{OH}}(b_u)$ mode with the bending OH modes δ_{OH} , C=O stretching $\nu_{\text{C=O}}$ mode or the low frequency modes alone leads to a blue shift of the anharmonic frequency compared to the harmonic value of 3245 cm^{-1} . Furthermore, because of the frequency mismatch between the overtones of $\delta_{\text{OH}}(b_u) + \delta_{\text{OH}}(a_g)$ at 2888 cm^{-1} and $\delta_{\text{OH}}(b_u) + \nu_{\text{C=O}}(a_g)$ at 3154 cm^{-1} , and $\nu_{\text{OH}}(b_u)$ at $3349/3352 \text{ cm}^{-1}$ there is also no increase in the intensities of the bending or stretching overtones. Hence, only upon the inclusion of the symmetric $\nu_{\text{OH}}(a_g)$ mode in the model the red shift of the antisymmetric OH stretch band appears. Fermi resonances with the combination bands can then contribute to the shape of the $\nu_{\text{OH}}(b_u)$ band. In addition, within the $\nu_{\text{OH}}(b_u)$ band Frank-Condon type vibrational progression are observed. Namely, computations performed on the potentials including the low frequency modes indicate that the $\nu_{\text{OH}}(b_u)$ fundamental transition is accompanied with additional transitions whose difference with the $\nu_{\text{OH}}(b_u)$ frequency matches exactly the frequencies of the stretching and rocking modes of the dimer. In other words, once the Davydov interaction is taken into account, the scenery of the OH stretch band broadening encountered in ACAC is repeated.

Table 4.12: Two and three-dimensional vibrational analysis of the $\nu_{OH}(b_u)$ band calculated at the B3LYP/6-31+G(d) level of theory. Only transitions with significant IR intensities are listed.

Dim.	Coordinate	μ a.m.u.	Anharm. cm^{-1}	Intensity a.u.	Assignment
2D	$\nu_{OH}(a_g)$	1.074	3076	0.006	
	$\nu_{OH}(b_u)$	1.068	3090	0.263	$\nu_{OH}(b_u)$
3D	$\delta_{OH}(b_u)$	1.177			
	$\delta_{OH}(a_g)$	1.293	2888	0.003	$\delta_{OH}(b_u) + \delta_{OH}(a_g)$
	$\nu_{OH}(b_u)$	1.068	3349	0.208	$\nu_{OH}(b_u)$
	$\delta_{OH}(b_u)$	1.177			
	$\nu_{C=O}(a_g)$	5.969	3154	0.002	$\delta_{OH}(b_u) + \nu_{C=O}(a_g)$
	$\nu_{OH}(b_u)$	1.068	3352	0.205	$\nu_{OH}(b_u)$
	dimer stretch (a_g)	9.748	3315	0.214	$\nu_{OH}(b_u)$
	in-plane rock (a_g)	8.609			
	$\nu_{OH}(b_u)$	1.068			
	$\delta_{OH}(b_u)$	1.177	3040	0.270	$\nu_{OH}(b_u)$
	$\nu_{OH}(a_g)$	1.074			
	$\nu_{OH}(b_u)$	1.068			
	dimer stretch (a_g)	9.748	2995	0.280	$\nu_{OH}(b_u)$
	$\nu_{OH}(a_g)$	1.074	3213	0.014	$\nu_{OH}(b_u) + \text{dimer stretch } (a_g)$
	$\nu_{OH}(b_u)$	1.068			
in-plane rock (a_g)	8.609	2997	0.270	$\nu_{OH}(b_u)$	
$\nu_{OH}(a_g)$	1.074	3177	0.017	$\nu_{OH}(b_u) + \text{dimer rock } (a_g)$	
$\nu_{OH}(b_u)$	1.068				

4.3 Large amplitude approaches

This section is concerned with methods tailored to quantitatively describe the hydrogen large amplitude motion (LAM) in H-bonded systems. In the first approach, the HAT reaction in FAD and ACAC is described using internal coordinates. This approach results in a complicated form of a kinetic energy operator and one has to consider kinetic coupling terms as well as variable, coordinate dependent reduced masses. The other two approaches are aimed at constructing a set of LAM coordinates which diagonalize the kinetic energy of the N particles relative motion. These approaches are used to treat the mode specific tunneling dynamics in FAD. As already mentioned, there had been a controversy concerning the splittings for the FAD vibrational ground and asymmetric C-O stretch excited state observed in the VRT experiments [14, 45]. The LAM methods will be used to calculate the observed splittings.

4.3.1 Internal coordinates

Acetylacetone

To gain new insight into the hydrogen atom tunneling dynamics in ACAC, the spectrum of the enol form was further investigated by using a set of internal, large amplitude coordinates. Three symmetry adapted coordinates were used to span a three dimensional surface of ACAC (Figure 4.13):

$$\begin{aligned}\rho_1 &= r_1 + r_2 \\ \rho_2 &= r_1 - r_2 \\ \rho_3 &= \theta\end{aligned}\tag{4.2}$$

where r_1 is the distance from the bridging hydrogen atom to the donor oxygen atom, r_2 is the distance from the bridging hydrogen atom to the acceptor oxygen atom, and θ

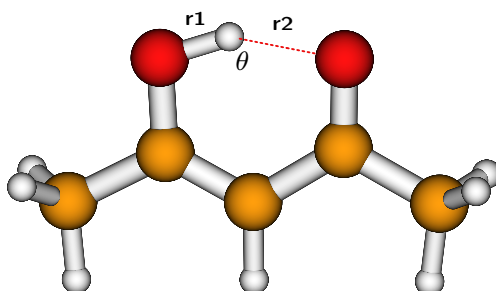


Figure 4.13: Internal coordinates used in the calculation of ACAC IR spectra

is the OHO angle. A related set of coordinates has been used by Shida and Almlöf for treating proton tunneling in malonaldehyde (MA) [39]. To span the 3D reaction surface of MA they used the internal coordinates r_1 and r_2 , and in addition the distance between the oxygen acceptor and oxygen donor, R . Almost identical coordinates to ρ_1 , ρ_2 and ρ_3 have been recently used by Špirko et al. in a reduced dimensionality study of the hydrogen atom transfer reaction in formimidol [116]. The symmetry adapted internal coordinates from Eq. (4.2) are designed to capture some basic features of the O-H \cdots O moiety in systems with hydrogen atom transfer. The coordinates ρ_1 and ρ_2 describe the symmetric and asymmetric hydrogen atom motion, while ρ_3 accounts for the distance between the two oxygen atoms.

The potential and the dipole moment surfaces were calculated on a variable grid with fixed ρ_1 , ρ_2 and ρ_3 values, while all other degrees of freedom were optimized. For $\rho_3 = 107^\circ$ the $\rho_1 \times \rho_2$ grid size was 15×16 , while for $\rho_3 = 187^\circ$ the size was 10×10 . Furthermore, during the optimization, the planarity of the chelate ring was enforced and the methyl groups were fixed in the eclipsed conformation which enhances hydrogen atom tunneling. In fact, the full optimization of the PES was attempted, but because of the extreme floppiness of the methyl groups rotational potential the calculation turned out to be numerically prohibitive. Nevertheless, the assumption of the ring planarity can be justified because of the large barrier height for *syn-anti* isomerization (16.2 kcal mol $^{-1}$ at the B1LYP/6-311G(d,p) level of theory) and the lower barrier to hydrogen atom transfer in ACAC compared to MA. These are indications that the in-plane motion of

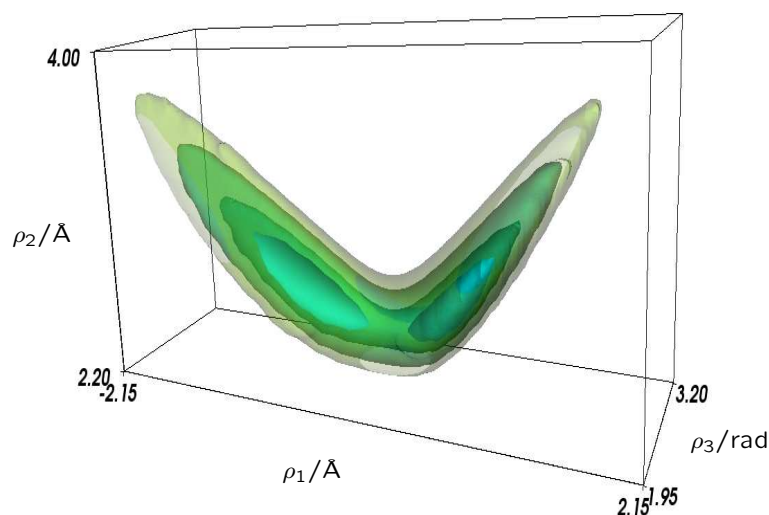


Figure 4.14: Three dimensional potential for ACAC spanned by the internal coordinates ρ_1 , ρ_2 and ρ_3 . Isosurfaces are spaced by 800 cm^{-1} , and the most inner isosurface corresponds to an energy of value 800 cm^{-1} above minimum.

the bridging hydrogen atom is strongly favoured. The three dimensional potential for ACAC is shown in Figure 4.14. The potential clearly displays a double well shape characteristic for the HAT systems.

To deal with a pure vibrational problem all structures resulting from the $\delta\rho_i$ displacements were rotated and translated in order to satisfy the center of mass and Eckart conditions (see Appendix A). The reference geometry to which each conformation was rotated and translated was the C_{2v} structure of the transition state for HAT reaction (TS3).

To construct the vibrational problem, the elements of Wilson G-matrix G^{rs} , $r = 1, 3$; $s = 1, 3$ for each ρ_1 , ρ_2 and ρ_3 value were calculated. Following the work of Alexandrov et al. [117] and J. Stare and G. Balint-Kurti [85], first the elements of the inverse of the G-matrix, G_{rs} elements were calculated as

$$G_{rs} = \sum_{i=1}^{3N} \frac{1}{m_i} \frac{\partial x_i}{\partial \rho_r} \frac{\partial x_i}{\partial \rho_s} \quad (4.3)$$

The evaluation of the elements $\partial x_i/\partial \rho_r$ is essential in order to incorporate the effect of Cartesian-internal coordinate coupling that originates from the imposed Eckart constraints. While evaluating the derivatives $\partial \rho_r/\partial x_i$, one should first variate the Cartesian coordinate, impose the Eckart condition and then calculate the resulting change in internal coordinate. As the Eckart frame constrains affect only the Cartesian coordinates, but leaves the internal coordinates intact, non-zero derivatives $\partial \rho_r/\partial x_i$ would then arise only when the definition of the internal coordinate ρ_r involves the Cartesian coordinate x_i . On the other hand, when calculating the $\partial x_i/\partial \rho_r$ derivatives, in general, all the $\partial x_i/\partial \rho_r$ elements should have non-zero values for the variation of the internal coordinate affects all of the Cartesian coordinates through the imposed Eckart conditions. After calculating the G_{rs} elements for each value ρ_1 , ρ_2 and ρ_3 , the G^{rs} elements were obtained by inverting the corresponding 3×3 G_{rs} matrices. The evaluation of the G_{rs} elements requires the knowledge of the mutual dependence between all Cartesian and all internal coordinates. As there are 45 Cartesian coordinates in ACAC, 45 3D surfaces which represent the change of a particular Cartesian coordinate on the PES had to be analyzed. For example, to evaluate the derivatives $\partial x_i/\partial \rho_1$ at each grid point and for each possible value of ρ_2 and ρ_3 , the selected atomic Cartesian coordinate x_i was 1D spline interpolated along ρ_1 and then the $\partial x_i/\partial \rho_1$ value was evaluated for each value of ρ_1 . The same procedure was repeated twice with interchanged roles between the ρ_1 , ρ_2 and ρ_3 to get the $\partial x_i/\partial \rho_2$ and $\partial x_i/\partial \rho_3$ derivatives, respectively. All together, 15 000 1D spline interpolations have been done. Figure 4.15 displays selected results of the G^{rs} matrix calculation. 2D cuts (ρ_3 set to 187°) of G-matrix elements surfaces are presented. All G-matrix elements display a considerable coordinate dependence but the G^{22} term varies at most, in the

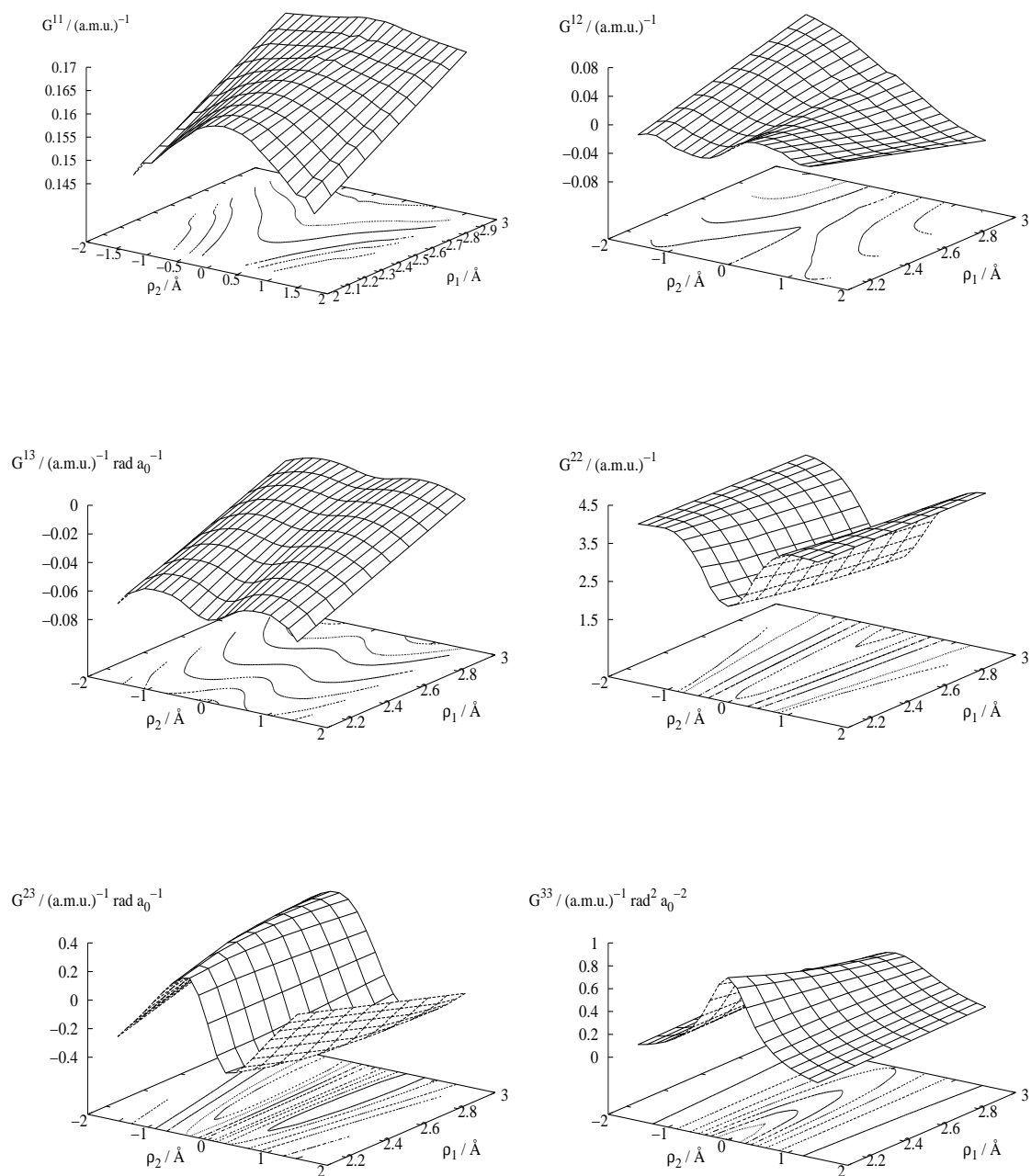


Figure 4.15: 2D projections of the G-matrix elements for $q_3 = 187^\circ$ for the SYN conformer of ACAC.

range between 1.7 and 4.3 (a.m.u.)⁻¹. For the particular choice of internal coordinates given in Eq. (4.2) the coupling terms: $-0.08 \leq G^{12} \leq 0.08$, $-0.07 \leq G^{13} \leq 0$ and $-0.4 \leq G^{23} \leq 0.04$ are small when compared to the diagonal ones. The coordinate dependence of the G-matrix elements has a great importance for in this way the coupling of the 3D subspace of internal degrees of freedom to other degrees of freedom of the molecule is taken into account, at least in the approximative way.

Further, the 3D potential, dipole moment surfaces and the six symmetry unique G^{rs} surfaces were interpolated by using the weighted Shepard interpolation scheme as implemented by Renka [108] on a $25 \times 25 \times 25$ direct product grid in the range $2.15 \text{ \AA} \leq \rho_1 \leq 4.05 \text{ \AA}$, $-2.0 \text{ \AA} \leq \rho_2 \leq 2.0 \text{ \AA}$ and $107^\circ \leq \rho_3 \leq 187^\circ$. The eigenvalues $E_{l,m,n}$ and eigenfunctions $\Psi_{l,m,n}$ of the vibrational Schrödinger equation

$$\left[\hat{T}_\rho + V(\rho_1, \rho_2, \rho_3) \right] \Psi_{l,m,n}(\rho_1, \rho_2, \rho_3) = E_{l,m,n} \Psi_{l,m,n}(\rho_1, \rho_2, \rho_3) \quad (4.4)$$

were obtained using the Fourier grid Hamiltonian method in internal coordinates [85] (see also the Appendix B). As previously, for the diagonalization of the matrix representation of the Hamiltonian the implicitly restarted Lanczos method [109] implemented in the ARPACK package [110, 111] was used.

Various approximations to the vibrational problem were investigated by solving the vibrational problem with kinetic energy operators \hat{T}_ρ given in Eqs. (3.48), (3.49) and (3.50). However, already the coordinate dependence of the G matrix elements shown in Figure 4.15 provided important information about the strength of the coupling between the vibrations of the O-H···O moiety and the remaining degrees of freedom. Accordingly, assumptions concerning the accuracy of the various approximations given in Eq. (3.48)-(3.50) could be made. For instance, for the chosen set of internal coordinates, the coupling terms G^{12} , G^{13} and G^{23} are small compared to the diagonal elements, and one could expect that Eq. (3.49) would provide a more accurate description of hydrogen bond dynamics than Eq. (3.50).

After the vibrational eigenvalues and eigenfunctions on the $V(\rho_1, \rho_2, \rho_3)$ potential were obtained, the tunneling splitting of the ground state, i.e., the vibrational transition frequency from the symmetric, 0(+), to the asymmetric ground state, 0(-), was simply calculated as the difference between the two lowest eigenvalues.

$$\omega(0(+) \rightarrow 0(-)) = E_{100} - E_{000} \quad (4.5)$$

By analogy the vibrational transition frequencies of the O-O stretching doublet are $\omega(0(+) \rightarrow 1(-)) = E_{101} - E_{000}$ and $\omega(0(+) \rightarrow 1(-)) = E_{001} - E_{000}$. Since the relationship between the OH stretching mode and the selected internal coordinates is not easy to establish an assignment was based on the comparison between IR intensities, $I_0(\omega)$, obtained from the d^x and d^y components of the dipole moment separately (see Eq. (4.1)).

Table 4.13: Vibrational transition frequencies and intensities for the **TS2** conformer of ACAC obtained from fully coupled calculations (Eq. (3.48)), "no kinetic coupling" approximation (Eq. (3.49) and "constant G -matrix" approximation Eq. (3.50)).

	Eq. (3.48)		Eq. (3.49)		Eq. (3.50)	
	freq/cm ⁻¹	Int.	freq/cm ⁻¹	Int.	freq/cm ⁻¹	Int.
ground state						
0(+) → 0(-)	116	0.1321	89	0.1480	208	0.1058
O-O mode						
0(+) → 1(-)	523	0.00075	555	0.00013	632	0.00366
0(-) → 1(+)	224	0.0339	284	0.0308	191	0.0332
O-H stretching						
0(+) → 1(-)	2683	0.0030	2539	0.0032	2816	0.0020
0(-) → 1(+)	1830	0.0041	1734	0.0027	1706	0.0020

Table 4.13 compiles the vibrational transition frequencies and the intensities for the **TS2** conformer obtained by employing Eq. (3.48), (3.49), (3.50). The fully coupled calculation gave a ground state tunneling splitting of 116 cm⁻¹. By neglecting the mixed derivative terms (equivalent to neglecting the off diagonal elements of G -matrix) one obtains a tunneling splitting of 88 cm⁻¹. A different situation is encountered in the constant G matrix approximation where the tunneling splitting is greatly overestimated and a value of 207 cm⁻¹ is obtained. These results confirm the prediction that the constant G -matrix approximation of Eq. (3.50) is inadequate to describe the large amplitude hydrogen motion. Obviously, the hydrogen atom transfer induces a rearrangement of the whole molecular frame and the corresponding geometrical changes have to be accounted both in the potential and in the kinetic energy operator via accurate kinematic couplings.

In contrast to the normal mode description, where the line assignments in terms of zero-order states were quite straightforward, here the assignments, based on inspection of the wave functions plots, are more difficult. Valuable additional insight into the nature of the transitions is obtained by considering separately the contributions from the d^x and d^y vector components of the dipole moment. As the interest was in the stretching transitions, the focus was on the component of the dipole moment that changes mostly during the stretching motion i.e. the x component of the dipole moment. For the O-O stretching doublet the calculation yielded the transitions on 224 cm⁻¹ and 523 cm⁻¹. The two frequencies find good correspondence to the observed modes at 220 cm⁻¹ ($\nu_{\text{O-H}\cdots\text{O}}$ mode [28]) and 508 cm⁻¹ (in plane ring deformation mode, ν_{32} in the Table 4.6).

Figure 4.16 displays the calculated stick spectrum in the frequency range 500-4000

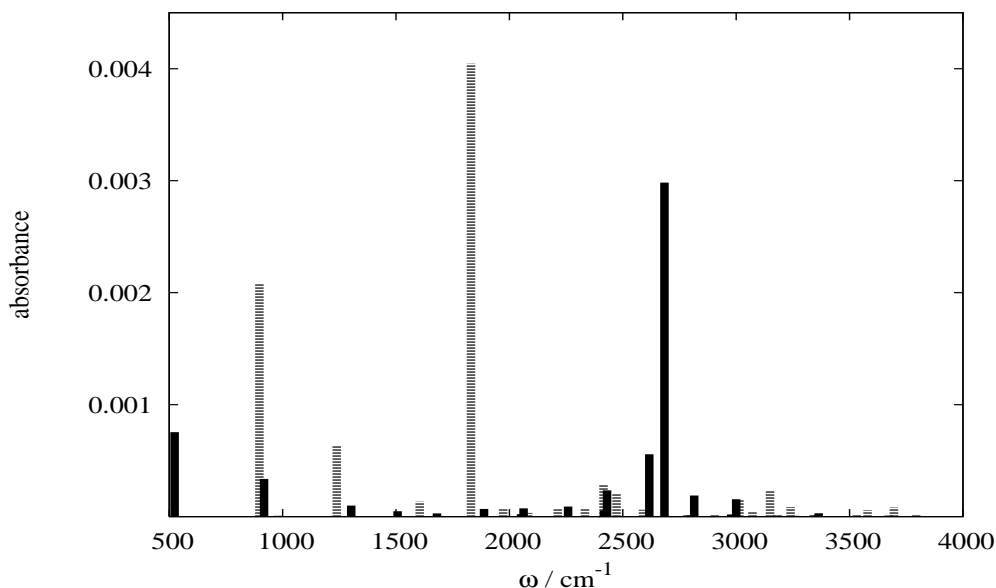


Figure 4.16: IR stick spectrum of the ACAC **TS2** conformer at $T=297$ K in the $500\text{-}4000$ cm^{-1} frequency range obtained in the internal coordinate representation. Transitions from the symmetric (solid black bars) and asymmetric (open dashed bars) ground states are shown on the same plot.

cm^{-1} . The transitions from the symmetric $0(+)$ ground state are shown in black and these from the asymmetric state $0(-)$ are in grey. The peak at 2683 cm^{-1} is assigned to a transition from the symmetric ground state to a vibration with an antisymmetric OH stretch character, and the peak at the 1830 cm^{-1} is assigned to a transition from the antisymmetric ground state to a vibration with the symmetric OH stretch character. As a result, the tunneling induced splitting in the OH stretch mode is calculated to be 853 cm^{-1} in the fully coupled case. Due to the strong promoting character of the OH stretching mode such large tunneling splitting was expected. The uncoupled Hamiltonian given in Eq. (3.49) yields the value of 806 cm^{-1} . The constant G -approximation again provided a larger splitting of 1100 cm^{-1} . Comparison with the normal modes calculation shows a blue shift of the $0(+)$ \rightarrow OH, $1(-)$ transition by about 300 cm^{-1} and a red shift of the $0(-)$ \rightarrow OH, $1(+)$ transitions by more than 500 cm^{-1} (compare to Table 4.10). The results are given with respect to the **TS2** most intense transition at 2350 cm^{-1} . It should be noted that the calculations were performed under the assumption of the planarity of the molecular ring, and it is reasonable to expect that the frequencies of the excited vibrational states could be overestimated. On the basis of the previous work on malonaldehyde [118] which compared planar and non-planar PES, the value of the OH-stretch vibrational energy level would be lower by as much as $100\text{-}200$ cm^{-1} . However a much smaller error is expected to occur for the splittings.

The red shifted $0(-) \rightarrow OH,1(+)$ transition falls into the C=O stretch band region. As already mentioned, the C=O stretch band has an interesting, still unexplained, three maxima peak structure. The temperature dependent experiments by B. Cohen and S. Weiss showed that only the intensity of the middle component at 1630 cm^{-1} changes with the temperature [56]. Also, only two components are observed at all temperatures in the spectra of the deuterated compound (d2-ACAC). Based on the previous perturbative and reduced dimensionality studies, it can be concluded that this results can not be explained just by the coexistence of two, energetically low laying ACAC conformers as in the work of Tayyari et al. [29]. According to the presented results the middle component of the C=O stretch band could be assigned to the $0(-) \rightarrow OH,1(+)$ transition. Indeed, due to the ground state tunneling splitting of 116 cm^{-1} , the intensity of the $0(-) \rightarrow OH,1(+)$ transition ought to be temperature dependent. Also, the position of the transition would change strongly in the deuterated molecules. However, for a more definitive assignment, an extension of the dimensionality of the model and the full optimization of the PES are required.

The formic acid dimer

For FAD two symmetry adapted internal coordinates were used to describe the synchronous double hydrogen transfer (Figure 3.4). There are:

$$\rho_1 = r_1 - r_3 + r_2 - r_4, \quad \rho_2 = R_1 + R_2$$

where r_1 and r_2 denote the distances from the hydrogen atom to the donor oxygen atoms and the r_3 and r_4 distances from the hydrogen atom to the acceptor oxygen atoms. R_1 and R_2 are the distances between the oxygen atoms in two monomers. This set is analogous to the set of coordinates used by N. Shida et al. to span the reaction surface for FAD [39]. The chosen coordinates incorporate the basic features of the double HAT reaction in FAD, i.e., the ρ_1 coordinate describes the simultaneous symmetric H atom transfer process while ρ_2 accounts for the distance between the two FA monomers.

The potential is constructed on a variable grid in the ρ_1 and ρ_2 direction at the B3LYP/6-311++G(3df,3pd) level of theory. This basis set was chosen in order to directly compare our results to previously calculated ground state tunneling splitting using the instanton approach [42]. Namely, upon the inclusion of the CCSD(T) energy correction using this basis set, Mil'nikov et al. obtained the ground state tunneling splitting of 0.0038 cm^{-1} which is very close to the assignment of F. Madeja [14].

To construct the potential all together 240 *ab initio* points were calculated on a $-4.0 \text{ \AA} < \rho_1 < 4.0 \text{ \AA}$ and $4.43 \text{ \AA} < \rho_2 < 7.13 \text{ \AA}$ grid. All other degrees of freedom were optimized. The 2D potential and the three symmetry unique G^{rs} matrices were interpolated using the weighted Shepard interpolation scheme to a 41×33 regular grid [108].

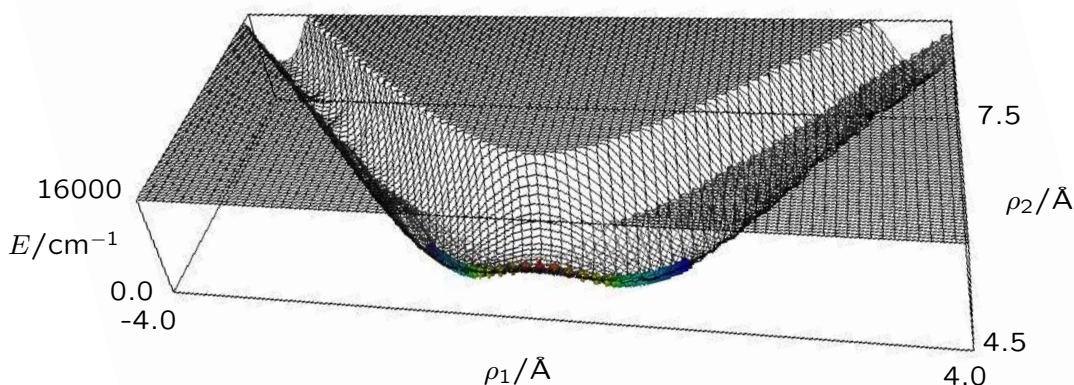


Figure 4.17: 2D potential of FAD spanned by internal coordinates ρ_1 and ρ_2 . The coloured points denote the IRP for HAT reaction connecting two minima (blue points) via a transition state (red point).

The 2D potential is displayed in Figure 4.17. The chosen coordinates reproduce the FAD double well shape of the potential where the two potential minima correspond to the two C_{2h} structures of FAD in Figure 2.4. The potential also reveals features characteristic for large amplitude motion in double well potentials: at short intermonomer distances (small ρ_2 value) the bridging hydrogen atom experiences a single well potential while increasing the intermonomer distance (increasing the ρ_2 value) the barrier to the hydrogen atom transfer rises and hydrogen tunneling sets in.

Figure 4.18 displays the coordinate dependence of the G^{11} , G^{12} and G^{22} matrix elements for the geometries with energy lower than $16\,000\text{ cm}^{-1}$. The G -matrix elements were calculated using the same procedure as described in section 4.3.1 for ACAC. On the basis of the earlier results it was concluded that the general geometrical changes triggered by the hydrogen transfer have to be included via an accurate kinematic coupling. The coordinate dependence of the G -matrix elements approximately takes into account the coupling of the 2D subspace spanned by the ρ_1 and ρ_2 directions to other, geometrically optimized degrees of freedom of the molecule. It can be seen that all the elements display a considerable coordinate dependence with the G^{11} term varying between 0.3 and 6.0 (a.m.u.)^{-1} . As in the case of ACAC, the off-diagonal coupling term G^{12} is small compared to the diagonal ones. The Schrödinger equation

$$[\hat{T}_q + V(\rho_1, \rho_2)]\Psi_{m,n}(\rho_1, \rho_2) = E_{m,n}\Psi_{m,n}(\rho_1, \rho_2) \quad (4.6)$$

with the kinetic energy operator \hat{T}_q given in Eqs. (3.48), (3.49) and (3.50) was solved using the Fourier grid Hamiltonian method in internal coordinates [85]. As previously, for the diagonalization, the Lanczos method was used [109]. The ground state splitting ($0(+) \rightarrow 0(-)$) was determined as the energy difference between the two lowest eigenstates. The full form of the kinetic energy operator yielded a ground state tunneling splitting of 0.0121 cm^{-1} . By neglecting the mixed derivative term and retaining the G -matrix coordinate dependence a tunnelling splitting of 0.007 cm^{-1} was obtained. The constant G -matrix approximation overestimates the splitting giving the value of 13.84 cm^{-1} . As in the case of ACAC neglecting the effect of geometry relaxation in a kinetic energy operator leads to a completely unrealistic representation of the HAT reaction overestimating the ground state splitting by orders of magnitude. The effect of the geometry relaxation on the tunneling dynamics in FAD was also investigated by D. Lauckaus [18]. He performed fully coupled ro-vibrational calculations up to six dimensions for FAD with and without geometry relaxation. On the potential with the barrier height of 2930 cm^{-1} ground state tunneling splittings in the range from 0.17 to 0.0088 cm^{-1} were obtained for the flexible model depending on the dimensions of the problem and the choice of explicitly treated internal coordinates. The realistic values

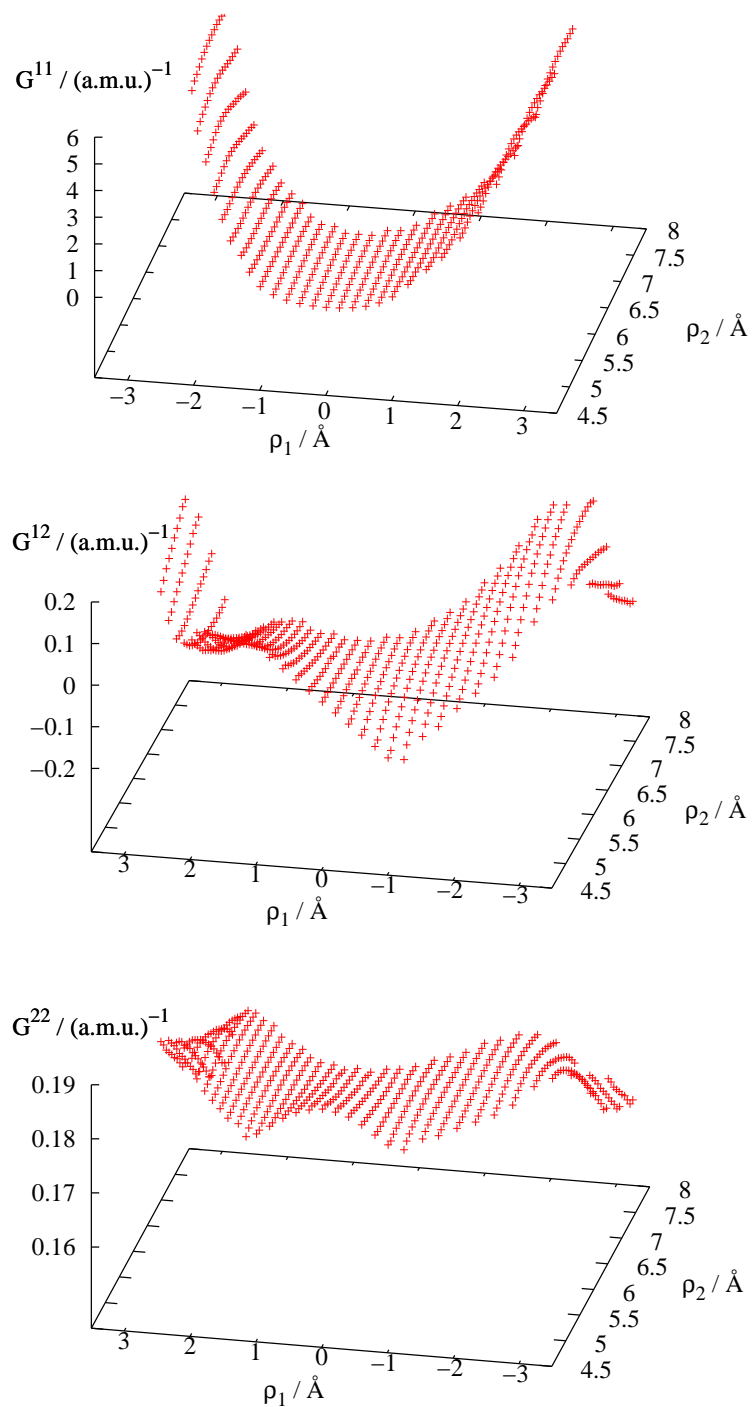


Figure 4.18: Coordinate dependence of the G^{11} , G^{12} and G^{22} matrix elements in $(\text{a.m.u.})^{-1}$ for the geometries of the FAD with the energy lower than $16\,000\text{ cm}^{-1}$.

Table 4.14: The ground state tunnelling splittings for FAD calculated at the B3LYP/6-311++G(3df,3pd) and CCSD(T)/cc-pVTZ//B3LYP/6-311++G(3df,3pd) level of theory using the internal coordinates ρ_1 , ρ_2 for a fully coupled calculation (Eq. (3.48)), "no kinetic coupling" approximation (Eq. (3.49)) and "constant G -matrix" approximation (Eq. (3.50)).

	Eq. (3.48) freq/cm ⁻¹	Eq. (3.49) freq/cm ⁻¹	Eq. (3.50) freq/cm ⁻¹
DFT			
0(+) \rightarrow 0(-)	0.0121	0.007	13.8
with CCSD(T) correction			
0(+) \rightarrow 0(-)	0.0111	0.009	14.3

for the rigid model are obtained only if all the major heavy atom motion of the HAT process are explicitly included in the treatment. In FAD at least four internal coordinates had to be included. D. Luckhaus [18] has shown that a converged ground state splitting can be obtained in a five dimensional model yielding the splitting of 0.0013 cm⁻¹ for (DCOOH)₂. Furthermore, Mil'nikov et al. used the instanton WKB theory on the B3LYP/6-311++G(3df,3dp) potential and obtained the value of 0.17 cm⁻¹ for the ground state tunneling splitting in FAD [42]. Taking into account the CCSD(T) corrections the ground state splitting of 0.0038 cm⁻¹ was obtained. A large change of the barrier height from 2280 cm⁻¹ (at the DFT/6-311++G(3df,3dp) level) to 2837 cm⁻¹ (the CCSD(T) correction) induced a large change in the splitting due to the differences in instanton trajectories. On the other hand the inclusion of the CCSD(T) correction to the DFT $V(\rho_1, \rho_2)$ potential introduces a small change of the ground state splitting. Namely, on the CCSD(T)/cc-pVTZ//B3LYP/6-311++G(3df,3dp) potential the ground state splitting of 0.01108 cm⁻¹ was obtained (Table 4.14). The difference between the DFT and CCSD(T) calculation is negligible compared to the CPU time needed for the calculation of the correction (around 120 single point calculation at the CCSD(T)/cc-pVTZ level was needed in order to calculate the correction). Such a negligible change is obviously a consequence of the fact that couple cluster corrections were calculated for frozen DFT geometries. It can be expected that the geometry relaxation on the CCSD(T) level would effect the HAT dynamics mainly through the change of the coordinate dependence of G -matrix elements since the DFT results both in the case of ACAC and FAD have proven the dominance of this effect. However, such calculations at the CCSD(T)/cc-pVTZ level for the molecule like FAD are still computationally prohibitive.

4.3.2 Reaction Space Hamiltonian approach

Large amplitude coordinates

In this section the reaction space Hamiltonian (RSH) method is used to describe the mode specific tunneling dynamics in FAD. Following the approach in Ref. [19] two collective large amplitude coordinates \mathbf{d}_1 and \mathbf{d}_2 were constructed as given by Eqs. (3.59) and (3.60). Mass weighted coordinates for the right-hand (\mathbf{X}_R), left-hand (\mathbf{X}_L) minimum and the transition state for the HAT (\mathbf{X}_{TS}) calculated at the B3LYP/6-311++G(3df,3pd) level of theory have been used. It is important to notice that the geometries \mathbf{X}_R and \mathbf{X}_L are unique only up to an arbitrary rotation. To remove this arbitrariness, two geometries of the minima as well as all the geometries on the IRP were rotated with respect to the \mathbf{X}_{TS} in order to satisfy the Eckart conditions. The atomic displacements corresponding to the \mathbf{d}_1 and \mathbf{d}_2 vectors are shown in Figure 4.19. It can be seen that the coordinate \mathbf{d}_1 corresponds to the double hydrogen atom transfer motion while \mathbf{d}_2 accounts for the distance between the two FA monomers. As suggested in Ref. [19] to inspect part of the potential spanned by vectors \mathbf{d}_1 and \mathbf{d}_2 , the IRP connecting the \mathbf{X}_{TS} structure with the minima structures \mathbf{X}_R and \mathbf{X}_L , was projected onto the reaction plane ($\mathbf{d}_1, \mathbf{d}_2$). The projected geometries are calculated as

$$\bar{\mathbf{X}}(s) = \mathbf{X}_{TS} + \sum_{i=1}^2 [(\mathbf{X}(s) - \mathbf{X}_{TS}) \cdot \mathbf{d}_i] \mathbf{d}_i \quad (4.7)$$

and the difference respect to the corresponding geometries on the IRP was expressed as the root-mean squared (RMS) difference:

$$\sigma^2 = \frac{1}{\sqrt{N_{\text{at}}}} \sqrt{(\bar{\mathbf{x}}(s) - \mathbf{x}(s))^2} \quad (4.8)$$

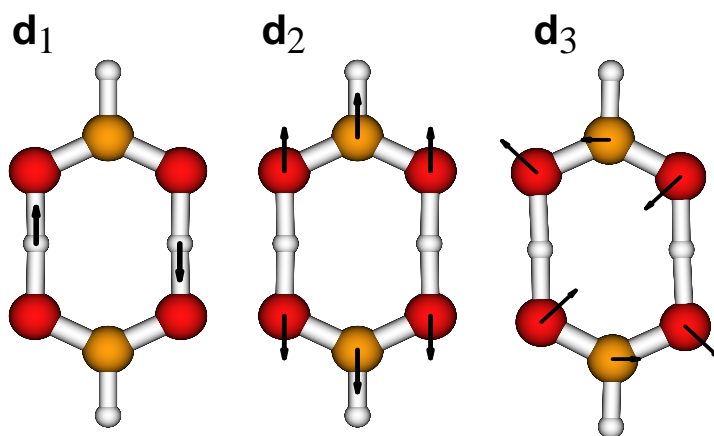


Figure 4.19: Displacements along the vectors \mathbf{d}_1 , \mathbf{d}_2 and \mathbf{d}_3 . Only the most important displacements are shown.

where the lower case letters refer to non-mass weighted geometries. The results are displayed in Figure 4.20. The upper panel shows the energy profile of the IRP (solid squares) and its projection on the $(\mathbf{d}_1, \mathbf{d}_2)$ plane (crosses) while the lower panel displays the RMS difference between the corresponding geometries (crosses). By definition, the RMS difference vanishes at the transition state ($s = 0 \text{ a}_0 (\text{a.m.u.})^{-1/2}$) and at the minima

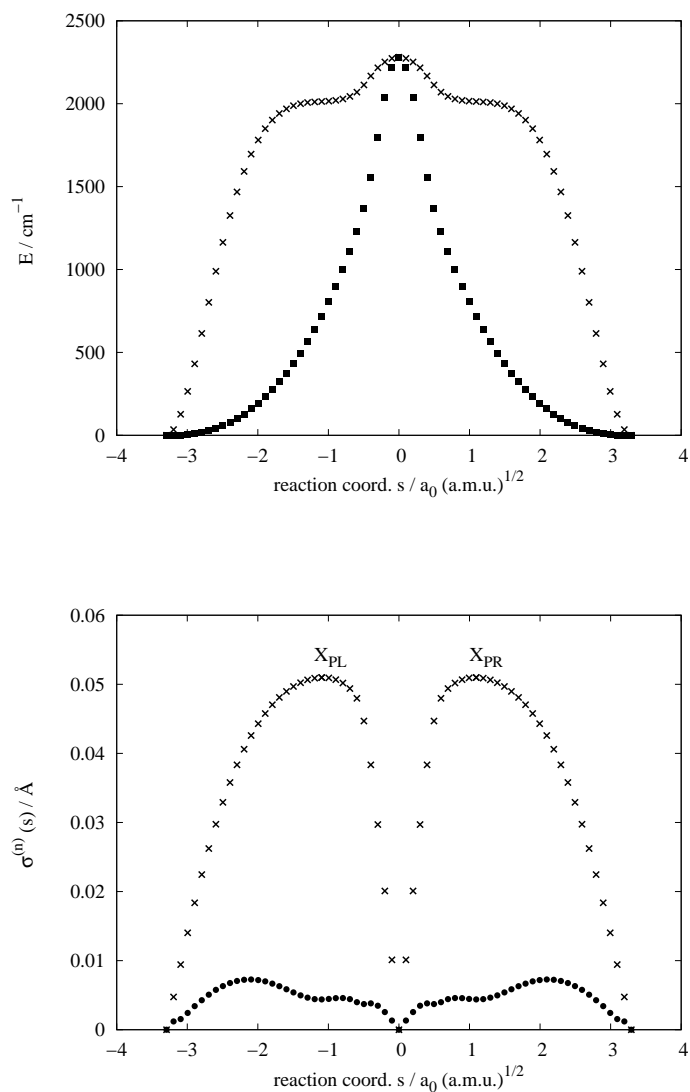


Figure 4.20: Upper panel: Energy profile along the IRP (solid squares) and the energy difference between the IRP geometries and their projections on a reaction plane spanned by vectors \mathbf{d}_1 and \mathbf{d}_2 (crosses). Lower panel: Crosses - RMS difference between the IRP geometries and their projection on the plane spanned by \mathbf{d}_1 and \mathbf{d}_2 . Solid dots - RMS difference between the IRP geometries and their projection on the reaction space spanned by $\mathbf{d}_1, \mathbf{d}_2$ and \mathbf{d}_3 vectors

($s = 3.3 \text{ a}_0 \text{ (a.m.u.)}^{-1/2}$, $s = -3.3 \text{ a}_0 \text{ (a.m.u.)}^{-1/2}$). It reaches its maximum of $5.1 \cdot 10^{-2} \text{ \AA}$ at $s = 1.1 \text{ a}_0 \text{ (a.m.u.)}^{-1/2}$ (Figure 4.20) with an energy difference of more than 1600 cm^{-1} . Because of the large deviation of the IRC geometries from the reaction plane spanned by the vectors \mathbf{d}_1 and \mathbf{d}_2 one concludes that the reaction plane represents a poor start for a Taylor expansion of the full-dimensional potential of FAD. To build up a configurational subspace closer to the IRP a third vector \mathbf{d}_3 was introduced. The vector was constructed using the two symmetrically related geometries \mathbf{X}_{PL} and \mathbf{X}_{PR} for which the $(\mathbf{d}_1, \mathbf{d}_2)$ RMS difference $\sigma^{(2)}(s)$ in Figure 4.20 has its maximum. It was defined as

$$\mathbf{d}_3 = \frac{\mathbf{X}_{\text{PL}} - \mathbf{X}_{\text{PR}}}{|\mathbf{X}_{\text{PL}} - \mathbf{X}_{\text{PR}}|} \quad (4.9)$$

and Gram-Schmidt orthogonalized with respect to the \mathbf{d}_1 and \mathbf{d}_2 vectors. The three dimensional space spanned by \mathbf{d}_1 , \mathbf{d}_2 and \mathbf{d}_3 vectors will be called *reaction space*. According to the molecular symmetry transformation \mathcal{T} (permutation of atoms and rotation which transforms \mathbf{X}_{L} to \mathbf{X}_{R} and vice versa) the \mathbf{d}_3 vector transforms as

$$\mathcal{T} \mathbf{d}_3 = -\mathbf{d}_3$$

The atomic displacements corresponding to the \mathbf{d}_3 vector are shown in Figure 4.19. These involve a wagging motion of the formic acid monomer accompanying double hydrogen transfer. At this point it should be emphasized that the construction of the \mathbf{d}_1 and \mathbf{d}_2 vectors is general [16, 19, 93] but the inclusion of the other large amplitude vectors depends on the system in hand. For instance, the change of the FAD geometrical parameters along the IRP displayed in Figure 4.5 already indicated a kind of wagging motion of FA monomers during the HAT. This motion had to be incorporated in the treatment via a third LAM coordinate in order to construct the configurational subspace which confines the IRP. The RMS difference between the IRP geometries and their projections on the reaction space, $\sigma^{(3)}(s)$ is shown in a lower panel of Figure 4.20 (solid dots). One can see that the IRP lies approximately in the reaction space. Namely, in the 3D case the RMS difference has a maxima of only $0.73 \cdot 10^{-2} \text{ \AA}$ at $s = \pm 2.1 \text{ a}_0 \text{ (a.m.u.)}^{1/2}$ (Figure 4.20) which corresponds to an energy difference of around 25 cm^{-1} . The energy profile of the IRP in the reaction space spanned by \mathbf{d}_1 , \mathbf{d}_2 and \mathbf{d}_3 vectors is shown in Figure 4.21. The red squares in the IRP correspond to the geometries with the highest energy (starting from the transition state) and the blue colour corresponds to the geometries with the lowest energy on the IRP (ending in two minima). On the sides, the projection of the IRP on the reaction planes spanned by the $\mathbf{d}_1/\mathbf{d}_2$ (red), $\mathbf{d}_1/\mathbf{d}_3$ (green) and $\mathbf{d}_2/\mathbf{d}_3$ vectors (blue) are shown.

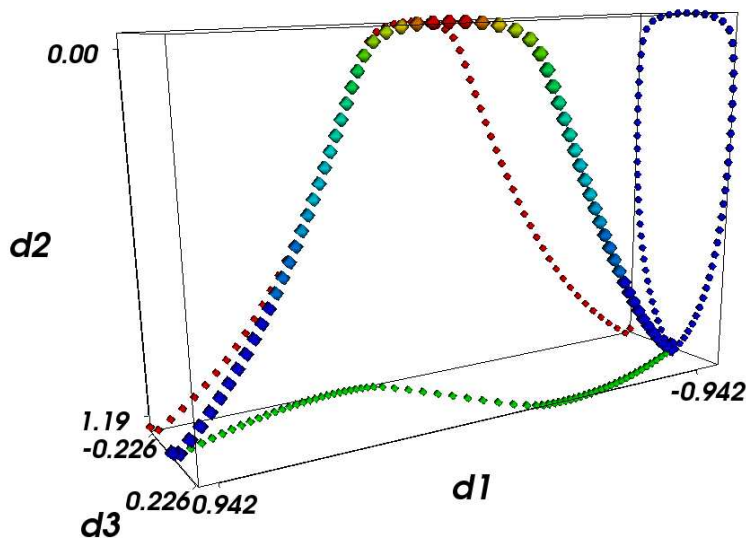


Figure 4.21: The energy profile of the IRP in the reaction space spanned by \mathbf{d}_1 , \mathbf{d}_2 and \mathbf{d}_3 vectors. On the sides, the projection of the IRP on the reaction planes spanned by the $\mathbf{d}_1/\mathbf{d}_2$ (red), $\mathbf{d}_1/\mathbf{d}_3$ (green) and $\mathbf{d}_3/\mathbf{d}_3$ vectors (blue) are shown.

The form of the reaction space Hamiltonian for FAD

The full-dimensional potential for FAD can be constructed as a harmonic approximation around the reaction space spanned by the three reactive degrees of freedom as given in Eq. (3.64). As explained in Chapter 3, section 3.3.3 the harmonically treated degrees of freedom, $\{\mathbf{Q}_i\}$ are obtained by diagonalizing the mass-weighted force constant matrix at the transition state with symmetry D_{2h} ($\mathbf{K}^{(t)}(\mathbf{X}_{\text{TS}})$) from which the \mathbf{d}_1 , \mathbf{d}_2 and \mathbf{d}_3 vectors as well as the rotational and translational directions were projected out. Note that the rigorous separation of the rotational motion would require rotation of all reaction space geometries in order to satisfy the Eckart conditions. However, this would destroy the orthogonal form of the Hamiltonian given in Eq. (4.11). For that reason the rotation is approximatively eliminated from the reaction space by imposing the Eckart conditions for the minima and the IRP geometries and from the "bath" by expressing the remaining DOF in terms of the eigenfunctions Q_i of the *projected* force constant matrix at the transition state geometry:

$$\mathbf{K}^{\mathcal{P}}(\mathbf{X}_{\text{TS}}) = (\mathbf{1} - \mathcal{P})\mathbf{K}^{(t)}(\mathbf{X}_{\text{TS}})(\mathbf{1} - \mathcal{P}) \quad (4.10)$$

Diagonalization of the $\mathbf{K}^{\mathcal{P}}(\mathbf{X}_{\text{TS}})$ matrix yields $3N_{\text{at}} - 9 = 21$ normal mode Q_i with non-vanishing eigenvalues (ω_i^2). The projector \mathcal{P} was defined in Eq. (3.67). All of these modes can be characterized according to the transformation \mathcal{T} as symmetric (+) or anti-

symmetric (-). In passing, it should be noted that projecting out the \mathbf{d}_1 , \mathbf{d}_2 and \mathbf{d}_3 vectors from the force constant matrix at the transition state corresponds to projecting out the O-H stretching mode with the harmonic frequency $1265i \text{ cm}^{-1}$ and symmetry b_{3g} , O...O stretching mode (symmetry a_g) with the frequency of 505 cm^{-1} and the CO₂ rocking mode, (symmetry b_{3g}) with the frequency of 232 cm^{-1} . Thus one concludes that these three motions are incorporated in the treatment via three LAM coordinates.

The difference between the IRP and its projection ($\mathbf{X}(s) - \bar{\mathbf{X}}(s)$) can be further analyzed by expressing it in terms of the displacements of the modes ΔQ_i relative to a variance δ_i of a corresponding ground state harmonic oscillator wave function (a Gaussian). These are shown in Figure 4.22. The relation between the δ_i in $a_0 \text{ (a.m.u.)}^{-1/2}$ and the frequency of the mode ω_i is calculated as

$$\delta_i = \sqrt{\frac{\hbar}{\omega_i}}$$

For all modes the displacement ΔQ_i is smaller than 15 % of the variance δ_i . For a Gaussian like function $\exp(-x^2/2\delta^2)$ at the position $x = 0.15\delta$ the value of the function drops to 99 % of its maximum. This indicates that all the displacements are small compared to the extend of a ground state wave function of the corresponding mode and that further improvements of the reaction space would have a negligible effect on a proper description of the IRP.

Very recently, the high resolution spectra in the region of the C-O asymmetric stretch in (HCOOH)₂ has been recorded and the resulting rotational-vibrational transitions have

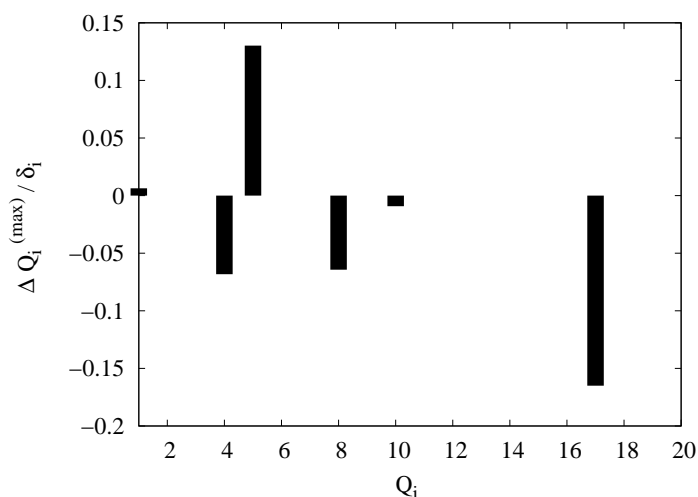


Figure 4.22: Maximum displacements ΔQ_i of the modes orthogonal to the reaction path along the IRP relative to variance δ_i of a ground state harmonic oscillator wave function with the eigenfrequency ω_i .

been assigned [45]. Denoting the set of normal modes at one of the FAD minima as $\{Y_k^{(f)}\}$ the asymmetric C-O stretch corresponds to the $Y_{11}^{(f)}$ mode with a harmonic frequency of 1260 cm^{-1} at the B3LYP/6-311++G(3df,3pd) level. To include the C-O stretching mode in the full dimensional Hamiltonian (see section 3.3.3), the overlap of the $Y_{11}^{(f)}$ mode with a set of $\{Q_i\}$ modes was inspected. The absolute values of the overlaps $|Y_{11}^{(f)} \cdot Q_i|$ are shown in Figure 4.23. Appreciable overlaps of the $Y_{11}^{(f)}$ mode exist with the:

- (i) symmetric modes of b_{1u} symmetry: Q_9 , (harmonic frequency $\nu = 1397 \text{ cm}^{-1}$), Q_{13} ($\nu = 1235 \text{ cm}^{-1}$) and Q_{16} ($\nu = 804 \text{ cm}^{-1}$)
- (ii) asymmetric modes of b_{2u} symmetry: Q_3 ($\nu = 1725 \text{ cm}^{-1}$), Q_6 ($\nu = 1566 \text{ cm}^{-1}$), Q_7 ($\nu = 1403 \text{ cm}^{-1}$)

On the basis of these overlaps and by exploring the fact that any linear combination of Q_i modes is equivalent, two new modes were defined: the q_a mode as a linear combination of antisymmetric Q_i modes and the q_s mode as a linear combination of symmetric Q_i modes. The modes are constructed in such a way that the coefficients in the linear combination reproduce the overlap $|Y_{11}^{(f)} \cdot Q_i|$. Specifically the combinations $\mathbf{q}_a = \sqrt{2/5}Q_3 + \sqrt{1/5}Q_6 + \sqrt{2/5}Q_7$ and $\mathbf{q}_s = \sqrt{9/11}Q_9 - \sqrt{1/11}Q_{13} + \sqrt{1/11}Q_{16}$ were used. The new coordinates transform as:

$$\mathcal{T} \mathbf{q}_s = \mathbf{q}_s, \quad \mathcal{T} \mathbf{q}_a = -\mathbf{q}_a$$

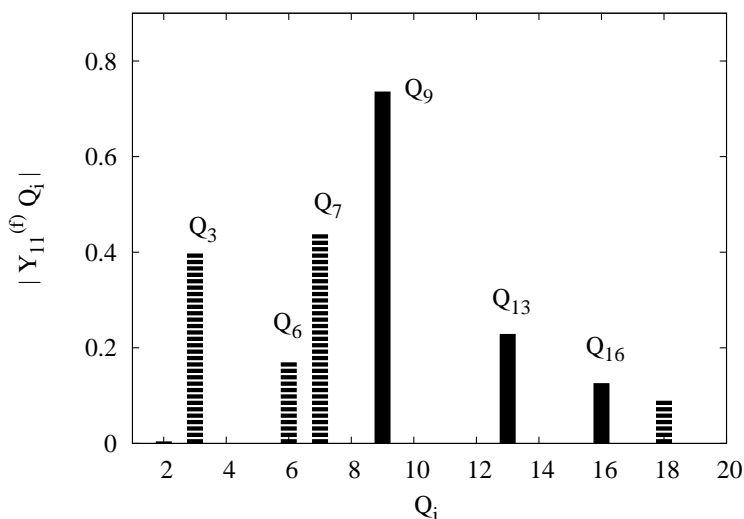


Figure 4.23: Absolute values of the overlaps $|Y_{11}^{(f)} \cdot Q_i|$ where $Y_{11}^{(f)}$ denotes the CO asymmetric stretching mode. Overlaps with the symmetric modes Q_i are shown as solid bars and with the asymmetric modes Q_i as dashed bars.

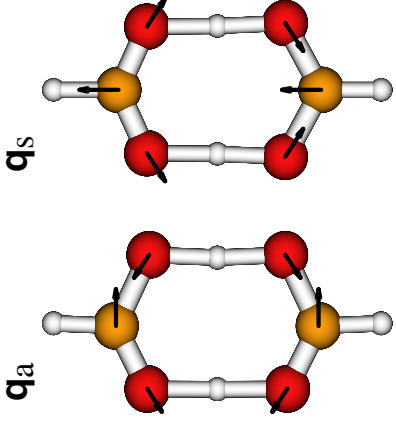


Figure 4.24: Atomic displacements along the vectors \mathbf{q}_a , \mathbf{q}_s . Only the most important displacements are shown.

and their atomic displacements are shown in Figure 4.24.

As explained in section 3.3.3. to analyze the $(\mathbf{d}_1, \mathbf{d}_2, \mathbf{d}_3, \mathbf{q}_s)$ and $(\mathbf{d}_1, \mathbf{d}_2, \mathbf{d}_3, \mathbf{q}_a)$ subspaces it is convenient to introduce the notion of reduced normal modes of the corresponding subspaces at the minima. The reduced normal modes will be denoted as $\{Y_k^{(\tilde{n}D)}\}$ where \tilde{n} is the dimensionality of the reduced space. The computations were performed for the structures $(\mathbf{X}_{R,L})$ and the $\{Y_k^{(4D)}\}$ at \mathbf{X}_R and \mathbf{X}_L are connected via symmetry transformation \mathcal{T} . The matrix that transforms the $(\mathbf{d}_1, \mathbf{d}_2, \mathbf{d}_3, \mathbf{q}_s)$ and $(\mathbf{d}_1, \mathbf{d}_2, \mathbf{d}_3, \mathbf{q}_a)$ sets to the corresponding reduced normal modes $\{Y_k^{(4D)}\}$ are presented in Table 4.15.

Table 4.15: Matrix which transforms the $(\mathbf{d}_1, \mathbf{d}_2, \mathbf{d}_3, \mathbf{q}_s)$ and $(\mathbf{d}_1, \mathbf{d}_2, \mathbf{d}_3, \mathbf{q}_a)$ vectors to a 4D reduced normal modes of the minimum, $\mathbf{Y}_k^{(4D)}$.

mode	ω / cm^{-1}	\mathbf{d}_1	\mathbf{d}_2	\mathbf{d}_3	\mathbf{q}_a
$\mathbf{Y}_1^{(4D)}$	2709	-0.54	0.19	0.82	≈ 0
$\mathbf{Y}_2^{(4D)}$	1527	≈ 0	≈ 0	≈ 0	0.998
$\mathbf{Y}_3^{(4D)}$	299	0.63	-0.55	0.54	≈ 0
$\mathbf{Y}_4^{(4D)}$	190	-0.56	0.81	0.18	≈ 0
mode	ω / cm^{-1}	\mathbf{d}_1	\mathbf{d}_2	\mathbf{d}_3	\mathbf{q}_s
$\mathbf{Y}_1^{(4D)}$	2709	-0.54	0.19	0.82	≈ 0
$\mathbf{Y}_2^{(4D)}$	1297	≈ 0	≈ 0	≈ 0	0.998
$\mathbf{Y}_3^{(4D)}$	299	0.63	-0.55	0.54	≈ 0
$\mathbf{Y}_4^{(4D)}$	190	-0.56	0.81	0.18	≈ 0

It can be seen that for both sets, the reduced mode $\mathbf{Y}_2^{(4D)}$ exclusively involves only one mode \mathbf{q}_a or \mathbf{q}_s while the $\mathbf{Y}_1^{(4D)}$, $\mathbf{Y}_3^{(4D)}$ and $\mathbf{Y}_4^{(4D)}$ reduced modes involve linear combination of all reaction space vectors \mathbf{d}_1 , \mathbf{d}_2 and \mathbf{d}_3 . Namely, in the harmonic approximation the coupling of the \mathbf{q}_a and \mathbf{q}_s modes and the \mathbf{d}_1 , \mathbf{d}_2 and \mathbf{d}_3 modes is forbidden by symmetry ($b_{1u} \otimes b_{3g} \neq a_g$ or $b_{2u} \otimes b_{3g} \neq a_g$).

The reduced normal modes ($\mathbf{Y}_k^{(4D)}$) are further analyzed by inspecting their overlaps (p_{jk}) with the full normal modes of the minimum ($\mathbf{Y}_k^{(f)}$). For that reason, the $3N_{\text{at}} \times 5$ matrix \mathbf{B} (Eq. (3.73)) which transforms between the reduced space and the full dimensional space was formed. The overlaps are calculated according to the Eq. (3.72) and compiled in Table 4.16 for both sets. The reduced mode $\mathbf{Y}_1^{(4D)}$ has a largest overlap with the OH stretching mode of the minimum (full normal mode $\mathbf{Y}_4^{(f)}$) with a harmonic

Table 4.16: Overlaps p_{jk} between the reduced normal modes $\mathbf{Y}_k^{(4D)}$ from Table 4.15 with the full normal modes of the minimum $\mathbf{Y}_k^{(f)}$. Harmonic frequencies of the full normal modes at the minimum are calculated at the B3LYP/6-311++G(3df,3pd) level of theory.

mode	ω / cm^{-1}	mode	ω / cm^{-1}	p_{jk}
$\mathbf{Y}_1^{(4D)}$	2709	$\mathbf{Y}_2^{(f)}$	3071	0.31
		$\mathbf{Y}_4^{(f)}$	3050	-0.78
		$\mathbf{Y}_6^{(f)}$	1698	-0.46
		$\mathbf{Y}_9^{(f)}$	1403	-0.25
$\mathbf{Y}_2^{(4D)}$	1527	$\mathbf{Y}_5^{(f)}$	1770	0.64
		$\mathbf{Y}_8^{(f)}$	1452	-0.24
		$\mathbf{Y}_{10}^{(f)}$	1403	0.41
		$\mathbf{Y}_{11}^{(f)}$	1259	-0.59
$\mathbf{Y}_2^{(4D)}$	1297	$\mathbf{Y}_5^{(f)}$	1770	-0.39
		$\mathbf{Y}_{10}^{(f)}$	1403	-0.33
		$\mathbf{Y}_{11}^{(f)}$	1259	0.75
		$\mathbf{Y}_{17}^{(f)}$	725	0.41
$\mathbf{Y}_3^{(4D)}$	299	$\mathbf{Y}_{21}^{(f)}$	207	0.83
		$\mathbf{Y}_{23}^{(f)}$	176	0.53
$\mathbf{Y}_4^{(4D)}$	190	$\mathbf{Y}_{21}^{(f)}$	207	-0.54
		$\mathbf{Y}_{23}^{(f)}$	176	0.84

frequency of a 2709 cm^{-1} . The reduced modes $\mathbf{Y}_3^{(4D)}$ and $\mathbf{Y}_4^{(4D)}$ have the largest overlap with the low frequency skeletal vibrations (full normal modes $\mathbf{Y}_{21}^{(f)}$ and $\mathbf{Y}_{23}^{(f)}$) which are the O...O stretching mode with a frequency of 207 cm^{-1} and the CO_2 rocking mode with a frequency of 190 cm^{-1} at the minimum. From the Table 4.16 it can be seen that neither the reduced mode $\mathbf{Y}_2^{(4D)}$ (1527 cm^{-1}) nor the reduced mode $\mathbf{Y}_2^{(4D)}$ (1297 cm^{-1}) can reproduce the C-O stretching mode of the minimum ($\mathbf{Y}_{11}^{(f)}$). They both include the anti-symmetric C-O (full normal mode $\mathbf{Y}_{11}^{(f)}$) and antisymmetric C=O stretching mode (full normal mode $\mathbf{Y}_5^{(f)}$). This could be expected since vectors \mathbf{q}_a and \mathbf{q}_s are both constructed from the eigenvectors of the projected force constant matrix at the transition state of D_{2h} symmetry for which the difference between the C-O(donor) and C=O(acceptor) bond does not exist. Therefore, to reproduce the asymmetric C-O stretching mode of the minimum both modes have to be included in the calculation, which leads to a 5D

Table 4.17: Matrix which transforms the directions ($\mathbf{d}_1, \mathbf{d}_2, \mathbf{d}_3, \mathbf{q}_s, \mathbf{q}_a$) to a 5D space of the reduced normal modes.

mode	ω / cm^{-1}	\mathbf{d}_1	\mathbf{d}_2	\mathbf{d}_3	\mathbf{q}_s	\mathbf{q}_a
$\mathbf{Y}_1^{(5D)}$	2709	0.54	-0.19	-0.82	≈ 0	≈ 0
$\mathbf{Y}_2^{(5D)}$	1616	≈ 0	≈ 0	≈ 0	0.51	-0.86
$\mathbf{Y}_3^{(5D)}$	1245	≈ 0	≈ 0	≈ 0	-0.86	-0.51
$\mathbf{Y}_4^{(5D)}$	299	0.63	-0.55	0.54	≈ 0	≈ 0
$\mathbf{Y}_5^{(5D)}$	190	-0.56	-0.81	-0.18	≈ 0	≈ 0

Table 4.18: Overlaps p_{jk} between the reduced normal modes $\mathbf{Y}_2^{(5D)}$ and $\mathbf{Y}_3^{(5D)}$ from Table 4.17 with the full normal modes $\mathbf{Y}_k^{(f)}$ of the minimum. It can be seen that the mode $\mathbf{Y}_3^{(5D)}$ represents the antisymmetric CO stretching mode.

mode	ω / cm^{-1}	mode	ω / cm^{-1}	p_{jk}
$\mathbf{Y}_2^{(5D)}$	1616	$\mathbf{Y}_5^{(f)}$	1770	-0.74
		$\mathbf{Y}_8^{(f)}$	1452	0.23
		$\mathbf{Y}_{10}^{(f)}$	1403	-0.54
		$\mathbf{Y}_{11}^{(f)}$	1259	0.11
		$\mathbf{Y}_{17}^{(f)}$	725	0.23
$\mathbf{Y}_3^{(5D)}$	1245 cm^{-1}	$\mathbf{Y}_{10}^{(f)}$	1403	0.11
		$\mathbf{Y}_{11}^{(f)}$	1259	0.97
		$\mathbf{Y}_{17}^{(f)}$	725	-0.18

problem.

In Table 4.17 the decomposition of the 5D $(d_1, d_2, d_3, q_a, q_s)$ space into the corresponding reduced normal modes at the minimum are given. The overlaps of the two most relevant reduced modes $\mathbf{Y}_k^{(5D)}$ and the full normal modes of the minimum are compiled in Table 4.18. Again the harmonic modes \mathbf{q}_s and \mathbf{q}_a do not mix with the reaction space vectors. Also from Tables 4.17 and 4.18 it can be seen that the linear combination of the \mathbf{q}_a and \mathbf{q}_s modes forming the reduced mode $\mathbf{Y}_3^{(5D)} = -0.86\mathbf{q}_s - 0.51\mathbf{q}_a$ has a 97% overlap with the target mode $\mathbf{Y}_{11}^{(f)}$. Thus one concludes that the defined 5D space fully encompasses the asymmetric C-O stretching mode observed in the high resolution experiment.

By defining the $(\mathbf{d}_1, \mathbf{d}_2, \mathbf{d}_3, \mathbf{q}_s, \mathbf{q}_a)$ set of coordinates, the following reaction space Hamiltonian ($\mathbf{q} = (q_a, q_s)$) has been obtained:

$$\begin{aligned} \hat{H} = & -\frac{1}{2} \sum_{i=1}^3 \frac{\partial^2}{\partial d_i^2} - \frac{1}{2} \sum_{k=1}^n \frac{\partial^2}{\partial q_k^2} + V(d_1, d_2, d_3, \mathbf{q} = 0) + \sum_{i=1}^2 \frac{\partial V(d_1, d_2, d_3, \mathbf{q})}{\partial q_i} \Big|_{q=0} q_i \\ & + \frac{1}{2} \sum_{i,j=1}^2 \frac{\partial^2 V(d_1, d_2, d_3, \mathbf{q})}{\partial q_i \partial q_j} \Big|_{q=0} q_i q_j \end{aligned} \quad (4.11)$$

where all other harmonic displacements are set to zero. The eigenvalue problem with the Hamiltonian given in Eq. (4.11) has been solved for the 5D case, but also for the 4D and 3D cases. For the construction of the PES all together 1500 single point energies, gradients and Hessians were calculated on the (d_1, d_2, d_3) grid at the B3LYP/6-311++G(3df,3pd) level of theory. The Modified Shepard method was used for the interpolation of the PES in all directions [19]. The grid parameters for the 3D (d_1, d_2, d_3) , 4D (d_1, d_2, d_3, q_s) , 4D (d_1, d_2, d_3, q_a) and the 5D $(d_1, d_2, d_3, q_s, q_a)$ calculations are given in Table 4.19. The interpolated potential at a general point \mathbf{X} is given by the weighted

Table 4.19: Grid parameters for the eigenvalue calculation on the 3D (d_1, d_2, d_3) , 4D (d_1, d_2, d_3, q_s) , 4D (d_1, d_2, d_3, q_a) and 5D $(d_1, d_2, d_3, q_s, q_a)$ PESs. For every DOF, the grid extends from q_{min} to q_{max} with n points.

no.	coor.	n	q_{min} [a_0 (a.m.u.) ^{1/2}]	q_{max} [a_0 (a.m.u.) ^{1/2}]
1	d_1	35	-3.5	3.5
2	d_2	31	-0.6	5.0
3	d_3	23	-1.4	1.4
4	q_a	21	-0.38	0.38
5	q_s	21	-0.42	0.42

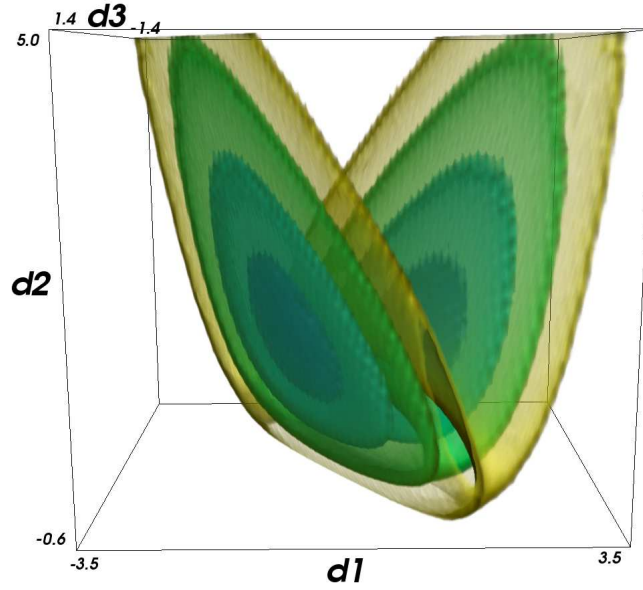


Figure 4.25: Three dimensional PES spanned by the large amplitude coordinates d_1, d_2, d_3 . Isosurfaces corresponding to the energy of 800 cm^{-1} , 2000 cm^{-1} , 4000 cm^{-1} and 6000 cm^{-1} are shown.

sum over all *ab initio* points j [119]:

$$V(\mathbf{X}) \approx \sum_j W_j(\mathbf{X}) V_j(\mathbf{X}) \quad (4.12)$$

where the weights are given by

$$\begin{aligned} W_j(\mathbf{X}) &= \frac{w_j(\mathbf{X})}{\sum_k w_k(\mathbf{X})} \\ w_j(\mathbf{X}) &= \left[(\mathbf{X} - \mathbf{X}^{(j)})^2 \right]^{-p} \end{aligned} \quad (4.13)$$

and $\mathbf{X}^{(j)}$ represents the *ab initio* point. The parameter p controls the smoothness of the interpolation (the value of 21 was taken). The contribution of each *ab initio* point to the potential at the point \mathbf{X} is given as

$$V_j(\mathbf{X}) = V^{(j)} + \mathbf{G}^{(j)} \cdot (\mathbf{X} - \mathbf{X}^{(j)}) + \frac{1}{2} (\mathbf{X} - \mathbf{X}^{(j)}) \mathbf{K}^{(j)} (\mathbf{X} - \mathbf{X}^{(j)}) \quad (4.14)$$

where $V^{(j)}$, $\mathbf{G}^{(j)}$ and $\mathbf{K}^{(j)}$ correspond to the energy, gradient and the force constant matrix at the *ab initio* point $\mathbf{X}^{(j)}$. The 3D potential $V(d_1, d_2, d_3)$ interpolated using the Modified Shepard method is given in Figure 4.25. The isosurfaces corresponding to 800 cm^{-1} , 2000 cm^{-1} , 4000 cm^{-1} and 6000 cm^{-1} are shown.

The eigenvalues and the eigenvectors of the 3D and 4D problems (Eq. 4.11) were obtained using the Fourier Grid Hamiltonian method [83]. For the diagonalization the

Lanczos method was used [109]. The eigenvalues and the eigenvectors of the 5D Hamiltonian (Eq. 4.11) were obtained by expressing the 5D eigenvectors in the basis of the three and two dimensional eigenvectors:

$$\Psi_k^{(5D)}(d_1, d_2, d_3, q_a, q_s) = \sum_{ij} c_{ijk} \phi_i^{(3D)}(d_1, d_2, d_3) \phi_j^{(2D)}(q_a, q_s) \quad (4.15)$$

Here $\phi_i^{(3D)}(d_1, d_2, d_3) (i = 0(\pm), 1(\pm), \dots)$ and $\phi_j^{(2D)}(q_a, q_s) (j = (N_a, N_s); N_a = 0, 1, \dots, N_s = 0, 1, \dots)$ represent the eigenvectors of a 3D and a 2D problem with the potentials $V(d_1, d_2, d_3, \mathbf{q} = 0)$ and $V(\mathbf{d} = 0, q_a, q_s)$. To obtain the convergence of the eigenvalues only the lowest 12 eigenfunctions from each set were needed.

Ground and vibrationally-excited state tunneling splittings in FAD

The frequency splittings obtained by using the PESs of increased dimensionality are compiled in Table 4.20. Only the transition frequencies are given, the IR intensities of the transition were not calculated. The appropriate dipole moment surfaces could not be

Table 4.20: Ground state and excited state tunnelling splittings calculated on various potentials for which the grid parameters are given in Table 4.19.

model	transition	$\omega_{ij} / \text{cm}^{-1}$	$\Delta_i / \text{cm}^{-1}$
3D (d_1, d_2, d_3)			
ground state	$\Psi_{0(+)}^{(3D)} \rightarrow \Psi_{0(-)}^{(3D)}$		0.197
4D (d_1, d_2, d_3, q_a)			
ground state	$\Psi_{0(+)}^{(4D)} \rightarrow \Psi_{0(-)}^{(4D)}$		0.162
$q_4^{(a)}$ mode	$\Psi_{0(+)}^{(4D)} \rightarrow \Psi_{1(-)}^{(4D)}$	1571.60134	0.112
	$\Psi_{0(+)}^{(4D)} \rightarrow \Psi_{1(+)}^{(4D)}$	1571.71362	
4D (d_1, d_2, d_3, q_s)			
ground state	$\Psi_{0(+)}^{(4D)} \rightarrow \Psi_{0(-)}^{(4D)}$		0.197
$q_4^{(s)}$ mode	$\Psi_{0(+)}^{(4D)} \rightarrow \Psi_{1(-)}^{(4D)}$	1373.4417	0.199
	$\Psi_{0(+)}^{(4D)} \rightarrow \Psi_{1(+)}^{(4D)}$	1373.64039	
5D (d_1, d_2, d_3, q_s, q_a)			
ground state	$\Psi_{0(+)}^{(5D)} \rightarrow \Psi_{0(-)}^{(5D)}$		0.155
$q_4^{(s)}$ mode	$\Psi_{0(+)}^{(5D)} \rightarrow \Psi_{1(+)}^{(5D)}$	1284.68851	0.0655
	$\Psi_{0(+)}^{(5D)} \rightarrow \Psi_{1(-)}^{(5D)}$	1284.75401	

obtained from the *ab initio* calculations on the (d_1, d_2, d_3) grid because the motion along the reaction space directions does not change the dipole moment of the molecule, i.e., $\mu^\alpha(d_1, d_2, d_3) = 0$ for $\alpha = x, y, z$. The ground state tunnelling splitting i.e. the vibrational transition frequency from the symmetric (+) to the antisymmetric (-) ground state is determined as the difference between the two lowest eigenvalues of the Hamiltonian (Eq. (4.11)). For the 3D case, a ground state tunneling splitting of 0.197 cm^{-1} was obtained. Upon the inclusion of the \mathbf{q}_s vector in the treatment the ground state tunneling is almost unchanged (0.197 cm^{-1}). However, the 4D model in which the \mathbf{q}_a vector is included gives the reduced value of 0.162 cm^{-1} indicating an anharmonic coupling of the \mathbf{q}_a mode to the large amplitude coordinates which can not be seen from the harmonic analysis in Table 4.16. In the 5D model in which both modes \mathbf{q}_a and \mathbf{q}_s modes were included the ground state tunneling splitting is further reduced to the value of 0.155 cm^{-1} . It is only in this model that the fundamental frequency and the splitting of the C-O stretching mode can be reproduced since here the modes \mathbf{q}_a and \mathbf{q}_s can mix giving the correct symmetry at the minimum. The frequency of the fundamental transition calculated as 1285 cm^{-1} is for a 60 cm^{-1} larger than the experimental value of 1225 cm^{-1} [45]. It should be noted however that no scaling accounting for the deficiencies of the DFT was introduced. Further discrepancy can be explained by the limitation of the RSH method which cannot account for the vibration-rotation coupling.

The assignment of a CO stretching fundamental transition was obtained by inspecting the 2D projections of the 5D wavefunctions:

$$\phi_k^{(2D)}(q_i, q_j) = \int \Psi_k^{(5D)*} \Psi_k^{(5D)} dq_{l \neq \{i, j\}} \quad (4.16)$$

The resulting 2D projections of the $\Psi_{1(\pm)}^{(5D)}$ wave functions are shown in Figure 4.26. The splitting in the asymmetric C-O stretching mode was evaluated as 0.066 cm^{-1} which is a 2.4 times *smaller* value than the splitting in the ground state (0.155 cm^{-1}). This implies that the asymmetric C-O stretching mode of FAD is not a promoting mode as suggested by the first experimental assignment for $(\text{DCOOH})_2$ [14]. On the contrary, it can be concluded that the excitation of the C-O stretching vibrational mode suppresses the tunneling in FAD. This finding is consistent with the results of Z. Smedarchina et al. who presented the only theoretical prediction of both, ground state and vibrationally excited splitting in $(\text{DCOOH})_2$ so far [43]. In their approximate instanton approach third order anharmonic couplings of the tunneling coordinate to two transition state modes (roughly corresponding to \mathbf{q}_a and \mathbf{q}_s) increase the effective mass of the tunneling particle as well as the barrier height thus leading to a reduced value of the splitting in the vibrationally excited state. However, in the present 5D RSH approach the reduced

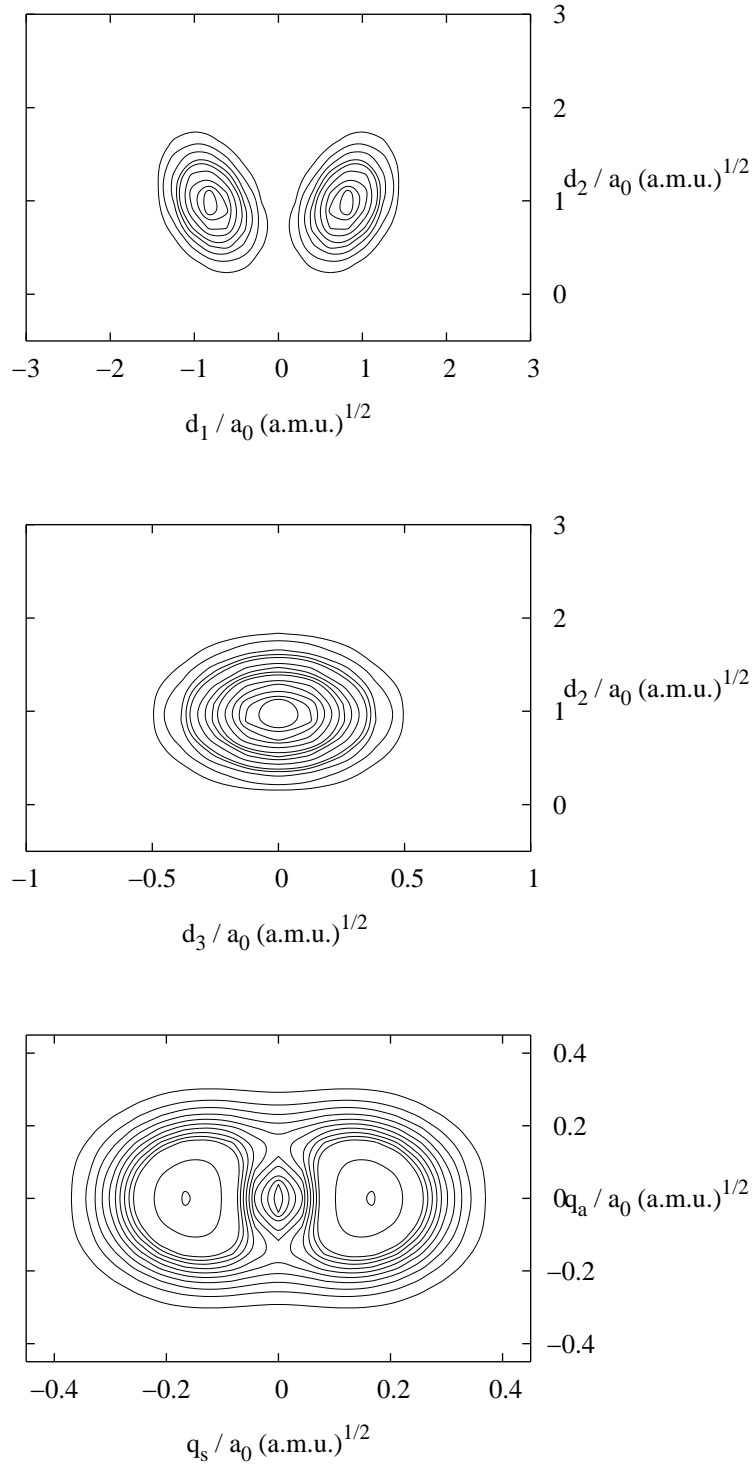


Figure 4.26: 2D projections $\phi_{1(\pm)}^{(2D)}(d_1, d_2)$, $\phi_{1(\pm)}^{(2D)}(d_3, d_2)$, $\phi_{1(\pm)}^{(2D)}(q_a, q_s)$ of the $\Psi_{1(\pm)}^{(5D)}$ wave function calculated according to Eq. (4.16).

splitting of the asymmetric C-O stretching mode is a consequence of a mixing between the 3D reaction space and 2D space spanned by the \mathbf{q}_a and \mathbf{q}_s modes. Namely, by inspecting the expansion coefficients in Eq. (4.15) it can be concluded that the excited state 5D wave function represents the combination of the \mathbf{q}_a and \mathbf{q}_s fundamental excitation, but also contains the contribution from the reaction space wave function ($\phi_{0(\mp)}^{(3D)}(d_1, d_2, d_3)$):

$$\Psi_{1(\pm)}^{(5D)} = [0.87\phi_{0(\pm)}^{(3D)} + 0.1\phi_{1(\pm)}^{(3D)}]\phi_{01}^{(2D)} + [0.47\phi_{0(\mp)}^{(3D)} + 0.08\phi_{1(\mp)}^{(3D)}]\phi_{10}^{(2D)} \quad (4.17)$$

By inspecting the $\phi_{0(\mp)}^{(3D)}(d_1, d_2, d_3)$ wave function it was found that it involves an excitation in the d_1 and d_2 directions. This would correspond to the $d_1 d_2 q_a q_s$ anharmonic coupling model from Ref. [43] which is indeed allowed by symmetry ($b_{3g} \otimes a_g \otimes b_{2u} \otimes b_{1u} = a_g$).

The absolute value of the splittings obtained in the 5D model (ground state = 0.155 cm^{-1} , excited state = 0.065 cm^{-1}) is for an order of magnitude larger than the experimental values obtained for $(\text{HCOOH})_2$ in Ref. [45] (ground state = 0.0158(3) cm^{-1} , excited state = 0.0100(3) cm^{-1}). The large discrepancy can be attributed to the deficiencies in the chosen DFT level of theory which cannot accurately predict the reaction barrier. In Ref. [42] the ground state tunneling splitting of 0.17 cm^{-1} was obtained at the B3LYP/6-311++G(3df,3pd) level of theory which is in agreement with the value of 0.155 cm^{-1} . By including the CCSD(T) correction to the electronic energy the barrier increases from 2280 cm^{-1} to 2837 cm^{-1} and the instanton tunneling splitting drops to the value of 0.0038 cm^{-1} which is slightly below the experimental value [42]. For this reason the effect of the chosen quantum chemistry level on the absolute value of tunneling splittings in FAD was further investigated by using the DFT/B3LYP functional with the 6-31+G(d) basis set. At the B3LYP/6-31+G(d) level of theory the ground state tunneling splitting of 0.0032 cm^{-1} was obtained and the splitting in the asymmetric C-O stretching was calculated as 0.0012 cm^{-1} . These values are for an order of magnitude smaller than the experimental values which can be mostly attributed to a larger barrier height compared to the B3LYP/6-311++G(3df,3pd) barrier (2933 cm^{-1} compared to 2280 cm^{-1}). However, the value of 0.0032 cm^{-1} is close to the ground state tunneling splitting of 0.0013 cm^{-1} obtained at the B3LYP/6-31+G(d) level of theory using the 5D reduced dimensionality approach by D. Luckhaus [18]. Also, it is close to the instanton value of 0.0077 cm^{-1} obtained for $(\text{DCOOH})_2$ by Mil'nikov et al. [42]. From the latter calculation one concludes that the B3LYP/6-31+G(d) quantum chemical method could lead to serious cancellation of errors. Namely, by including the CCSD(T) correction to the DFT/6-31+G(d) potential the barrier height increases to 4515 cm^{-1} leading to the tunneling splitting of $6 \cdot 10^{-5}$. In the light of the provided information one concludes that the use of the 6-311++G(3df,3pd) basis set is better justified although it gives too large

absolute numbers. Nevertheless, what is most important both quantum chemistry methods gave similar relative value for the splittings, i.e., the ground state tunneling splitting is 2.4 (2.7) times *larger* than the splitting in the asymmetric CO stretching mode. This in turn finds good agreement with the experimental ratio of splitting of 1.58 [45].

4.3.3 Generalized approximation to the reaction path

Following the approach of Hirschfelder and co-workers [94, 95, 96] a set of collective large amplitude coordinates based on a "mobile model" are constructed. Their ability to span the configurational space relevant for HAT reactions is investigated. In addition the rovibrational Hamiltonian in terms of a new coordinates is obtained.

Large amplitude coordinates

Let N_{at} denote the number of particles, $\tilde{\mathbf{R}}_j = (\tilde{R}_{jx}, \tilde{R}_{jy}, \tilde{R}_{jz})$ the Cartesian coordinates of an j -th particle in a space fixed system and m_j its mass. A set of coordinates $\mathbf{Z}_i = (Z_{ix}, Z_{iy}, Z_{iz})$ is defined using the mass dependent transformation matrix \mathbf{T} :

$$Z_{i\gamma} = \sum_{j=1}^{N_{\text{at}}} T_{ij} \tilde{R}_{j\gamma}, \quad i = 1, \dots, N_{\text{at}}, \quad \gamma = x, y, z \quad (4.18)$$

Aiming at the description of the double HAT reaction in FAD, one of many possible mobiles for FAD is chosen as (see Figure 4.27):

$$\begin{aligned} \mathbf{Z}_1 &= \tilde{\mathbf{R}}_1 - \tilde{\mathbf{R}}_7 \\ \mathbf{Z}_2 &= \tilde{\mathbf{R}}_2 - \tilde{\mathbf{R}}_8 \\ \mathbf{Z}_3 &= \tilde{\mathbf{R}}_3 - \tilde{\mathbf{R}}_6 \\ \mathbf{Z}_4 &= \tilde{\mathbf{R}}_5 - \tilde{\mathbf{R}}_4 \\ \mathbf{Z}_5 &= \tilde{\mathbf{R}}_9 - \frac{1}{2}(\tilde{\mathbf{R}}_6 + \tilde{\mathbf{R}}_3) \\ \mathbf{Z}_6 &= \tilde{\mathbf{R}}_{10} - \frac{1}{2}(\tilde{\mathbf{R}}_4 + \tilde{\mathbf{R}}_5) \\ \mathbf{Z}_7 &= \frac{\tilde{\mathbf{R}}_1 m_C + \tilde{\mathbf{R}}_7 m_H}{m_C + m_H} - \frac{\tilde{\mathbf{R}}_2 m_C + \tilde{\mathbf{R}}_8 m_H}{m_C + m_H} \\ \mathbf{Z}_8 &= \frac{\tilde{\mathbf{R}}_9 m_H + \tilde{\mathbf{R}}_6 m_O + \tilde{\mathbf{R}}_3 m_O}{m_H + 2m_O} - \frac{\tilde{\mathbf{R}}_{10} m_H + \tilde{\mathbf{R}}_4 m_O + \tilde{\mathbf{R}}_5 m_O}{m_H + 2m_O} \\ \mathbf{Z}_9 &= \frac{1}{2} \left(\frac{\tilde{\mathbf{R}}_9 m_H + \tilde{\mathbf{R}}_6 m_O + \tilde{\mathbf{R}}_3 m_O}{m_H + 2m_O} + \frac{\tilde{\mathbf{R}}_{10} m_H + \tilde{\mathbf{R}}_4 m_O + \tilde{\mathbf{R}}_5 m_O}{m_H + 2m_O} - \frac{\tilde{\mathbf{R}}_1 m_C + \tilde{\mathbf{R}}_7 m_H}{m_C + m_H} - \frac{\tilde{\mathbf{R}}_2 m_C + \tilde{\mathbf{R}}_8 m_H}{m_C + m_H} \right) \\ \mathbf{Z}_{10} &= \frac{1}{\sum_i m_i} \sum_{i=1}^{N_{\text{at}}} m_i \tilde{\mathbf{R}}_i \end{aligned} \quad (4.19)$$

where the coordinate Z_{10} joins the center of mass of the molecule to the origin of the space fixed system. A molecular symmetry transformation \mathcal{T} which transforms the left minimum to the right one (Eq. (3.62)) permutes the atoms in the molecule and thus

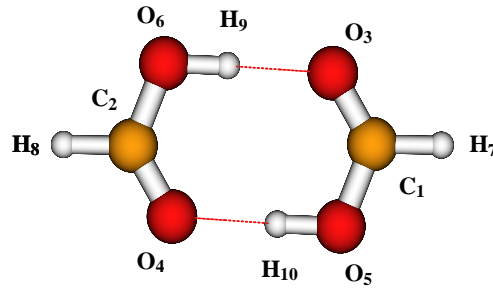


Figure 4.27: Minima structure of the formic acid dimer

changes the components of internal vectors $\{\mathbf{Z}_i\}$ as

$$\begin{aligned} \mathcal{T}\{Z_{1x}, Z_{2x}, Z_{3x}, Z_{4x}, Z_{5x}, Z_{6x}, Z_{7x}, Z_{8x}, Z_{9x}, Z_{10x}\} &= \{Z_{1x}, Z_{2x}, Z_{4x}, Z_{3x}, Z_{6x}, Z_{5x}, Z_{7x}, \\ &\quad -Z_{8x}, Z_{9x}, Z_{10x}\} \\ \mathcal{T}\{Z_{1y}, Z_{2y}, Z_{3y}, Z_{4y}, Z_{5y}, Z_{6y}, Z_{7y}, Z_{8y}, Z_{9y}, Z_{10y}\} &= \{-Z_{1y}, -Z_{2y}, -Z_{4y}, -Z_{3y}, -Z_{6y}, \\ &\quad -Z_{5y}, -Z_{7y}, Z_{8y}, -Z_{9y}, -Z_{10y}\} \\ \mathcal{T}\{Z_{1z}, Z_{2z}, Z_{3z}, Z_{4z}, Z_{5z}, Z_{6z}, Z_{7z}, Z_{8z}, Z_{9z}, Z_{10z}\} &= \{-Z_{1z}, -Z_{2z}, -Z_{4z}, -Z_{3z}, -Z_{6z}, \\ &\quad -Z_{5z}, -Z_{7z}, Z_{8z}, -Z_{9z}, -Z_{10z}\} \end{aligned}$$

The coordinates \mathbf{Z}_i are redefined in order to obtain symmetry adapted coordinates

$$\begin{aligned} \mathbf{Z}_3 &= \mathbf{Z}_3 + \mathbf{Z}_4 \\ \mathbf{Z}_4 &= \mathbf{Z}_3 - \mathbf{Z}_4 \\ \mathbf{Z}_5 &= \mathbf{Z}_5 + \mathbf{Z}_6 \\ \mathbf{Z}_6 &= \mathbf{Z}_5 - \mathbf{Z}_6 \end{aligned}$$

that separate correctly into symmetric $\mathbf{Z}^{(+)}$ and antisymmetric subgroups $\mathbf{Z}^{(-)}$ with respect to molecular symmetry transformation \mathcal{T} . The symmetry adapted coordinates transforms as

$$\begin{aligned} \mathcal{T}\mathbf{Z}_{i\gamma}^{(+)} &= \mathbf{Z}_{i\gamma}^{(+)} \\ \mathcal{T}\mathbf{Z}_{i\gamma}^{(-)} &= -\mathbf{Z}_{i\gamma}^{(-)} \end{aligned}$$

Alternatively, a related set of mass-weighted vectors $\tilde{\mathbf{S}}_i$ with elements

$$\tilde{\mathbf{S}}_{i\gamma} = \sqrt{\mu_i}\mathbf{Z}_i = \sum_{j=1}^{N_{\text{at}}} \tilde{\mathbf{W}}_{ij} \sqrt{m_j} \tilde{\mathbf{R}}_{j\gamma} \quad i = 1, \dots, N_{\text{at}} \quad \gamma = x, y, z \quad (4.20)$$

can be defined where the diagonal matrix μ is determined so that

$$\widetilde{\mathbf{W}}\widetilde{\mathbf{W}}^T = \mathbf{I}. \quad (4.21)$$

The form of the matrix $\widetilde{\mathbf{W}}$ follows from Eqs. (4.18) and (4.20):

$$\widetilde{\mathbf{W}} = \mu^{1/2} \mathbf{Tm}^{-1/2} \quad (4.22)$$

From the condition (4.21) and the fact that $\mathbf{Tm}^{-1/2}(\mathbf{Tm}^{-1/2})^T$ is a diagonal matrix it simply follows

$$\mu^{-1} = \mathbf{Tm}^{-1/2}(\mathbf{Tm}^{-1/2})^T \quad (4.23)$$

The matrix elements $\widetilde{W}_{i,1}, \widetilde{W}_{i,2}, \dots, \widetilde{W}_{i,N_{\text{at}}}$ form an N_{at} -dimensional vector $\widetilde{\mathbf{W}}_i$ and N_{at} vectors $\widetilde{\mathbf{W}}_1, \widetilde{\mathbf{W}}_2, \dots, \widetilde{\mathbf{W}}_{N_{\text{at}}}$ of unit length form a set of orthogonal coordinate axes in the N_{at} -space.

As for the choice of \mathbf{Z}_i coordinates, the choice of $\widetilde{\mathbf{S}}_i$ coordinates is not unique. Moreover, any set of new coordinates $\widetilde{\mathbf{S}}_i^{\text{new}}$ generated by unitary transformations of the form

$$\widetilde{\mathbf{S}}_i^{\text{new}} = \sum_{j=1}^{N-1} \widetilde{A}_{i,j} \widetilde{\mathbf{S}}_j \quad (4.24)$$

represents an equally acceptable set. In the geometrical sense the unitary transformation $\widetilde{\mathbf{A}}$ corresponds to the rotation of the coordinate axes $\widetilde{\mathbf{W}}_1, \widetilde{\mathbf{W}}_2, \dots, \widetilde{\mathbf{W}}_N$.

The Eq. (4.20) can be generalized as

$$S_i = \sum_j^{3N_{\text{at}}} W_{ij} \sqrt{m_j} R_j \quad i = 1, \dots, 3N_{\text{at}} \quad (4.25)$$

where $\mathbf{R} = (R_{1x}, R_{2x}, \dots, R_{N_x}, R_{1y}, R_{2y}, \dots, R_{N_y}, R_{1z}, R_{2z}, \dots, R_{N_z})^T$, and \mathbf{W} is a block diagonal matrix of size $3N_{\text{at}} \times 3N_{\text{at}}$ with blocks of size $N_{\text{at}} \times N_{\text{at}}$ formed by repeating $\widetilde{\mathbf{W}}$ on the diagonal. The set of $3N_{\text{at}}$ vectors \mathbf{W}_i form an orthogonal base. According to Eq. (4.24) new coordinates S_i can be derived by unitary transformations:

$$S_i^{\text{new}} = \sum_{j=1}^{3N_{\text{at}}} A_{i,j} S_j \quad (4.26)$$

Thus, in terms of a $3N_{\text{at}} - 3$ mass-weighted coordinates S_i the rovibrational Hamiltonian has a form

$$\hat{H} = -\frac{1}{2} \sum_{i=1}^{3N_{\text{at}}-3} \frac{\partial^2}{\partial S_i^2} + V(\mathbf{S}) \quad (4.27)$$

where $V(\mathbf{S})$ is the full dimensional potential. Note however that at this point rotational and vibrational motion are not separated.

Reaction Space Hamiltonian in reduced dimensionality

The next question to be answered is the nature of the best reaction coordinates that span the region of the potential relevant for the HAT process. According to Eq. (4.26) any unitary transformation of S_i coordinates yields an equally acceptable set of coordinates. The simplest option thus is to consider pure kinematic rotations between the pairs of $S_i^{(\pm)}$ coordinates belonging to the same symmetry subgroup:

$$\begin{aligned} S_i^{\text{new}} &= S_i \cos \theta + S_j \sin \theta \\ S_j^{\text{new}} &= -S_i \sin \theta + S_j \cos \theta \end{aligned} \quad (4.28)$$

As in the previous method, the intrinsic reaction path (IRP) defined in Eq. (3.56) is used in order to characterize the HAT in FAD serving as a basis for a selection of S_i coordinates that better portion the IRP. Accordingly, the angle θ is optimized in order to minimize the change of the coordinate S_i^{new}

$$\text{Min} \left(\text{Max}(S_i^{\text{new}}[s]) - \text{Min}(S_i^{\text{new}}[s]) \right) \quad (4.29)$$

over the entire series of geometries along the IRP. Thus, for each symmetric/antisymmetric subgroup, it was examined how many degrees of freedom can be made very small in change between neighbouring geometries on the IRP. Further, it should be emphasized that for all geometries on the IRP the Eckart conditions are imposed. In this way the intrinsic reaction path is made orthogonal to the infinitesimal rotations allowing for an approximative separation of vibrational and rotational motion.

In the case of FAD the kinematic optimization procedure (Eq. (4.28)-(4.29)) yields three large amplitude coordinates denoted as $S_1^{(-)}$, $S_2^{(+)}$ and $S_3^{(-)}$ that do change significantly along the IRP. The variation of the S_1 , S_2 and S_3 coordinates along the IRP is shown in Figure 4.28 together with the Cartesian displacements corresponding to the S_1 , S_2 and S_3 vectors. The Cartesian displacements are calculated by inverting the Eq. (4.20). One notices that the coordinate S_1 describes the synchronised HAT motion while S_2 and S_3 coordinates take into account the rearrangement of the molecular frame. These are the symmetric stretch and antisymmetric torsion of two monomers. The remaining coordinates S_i , $i = 4, 5, \dots, 3N_{\text{at}} - 3$ do not change appreciably along the IRP and can be treated via a harmonic approximation. The deviation between the IRP and a reaction space can be further quantified in terms of a root mean squared (RMS) difference between the non mass weighted IRP geometries ($\mathbf{x}(s)$) and its projections $\bar{\mathbf{x}}(s)$ on the reaction space spanned by relevant S_i coordinates. The RMS differences for $\tilde{n} = 2$ and $\tilde{n} = 3$ were calculated in analogy to the Eqs. (4.7) and (4.8). Also note that the Cartesian displacements corresponding to the displacements along the S_1 , S_2 and S_3 coordinates are

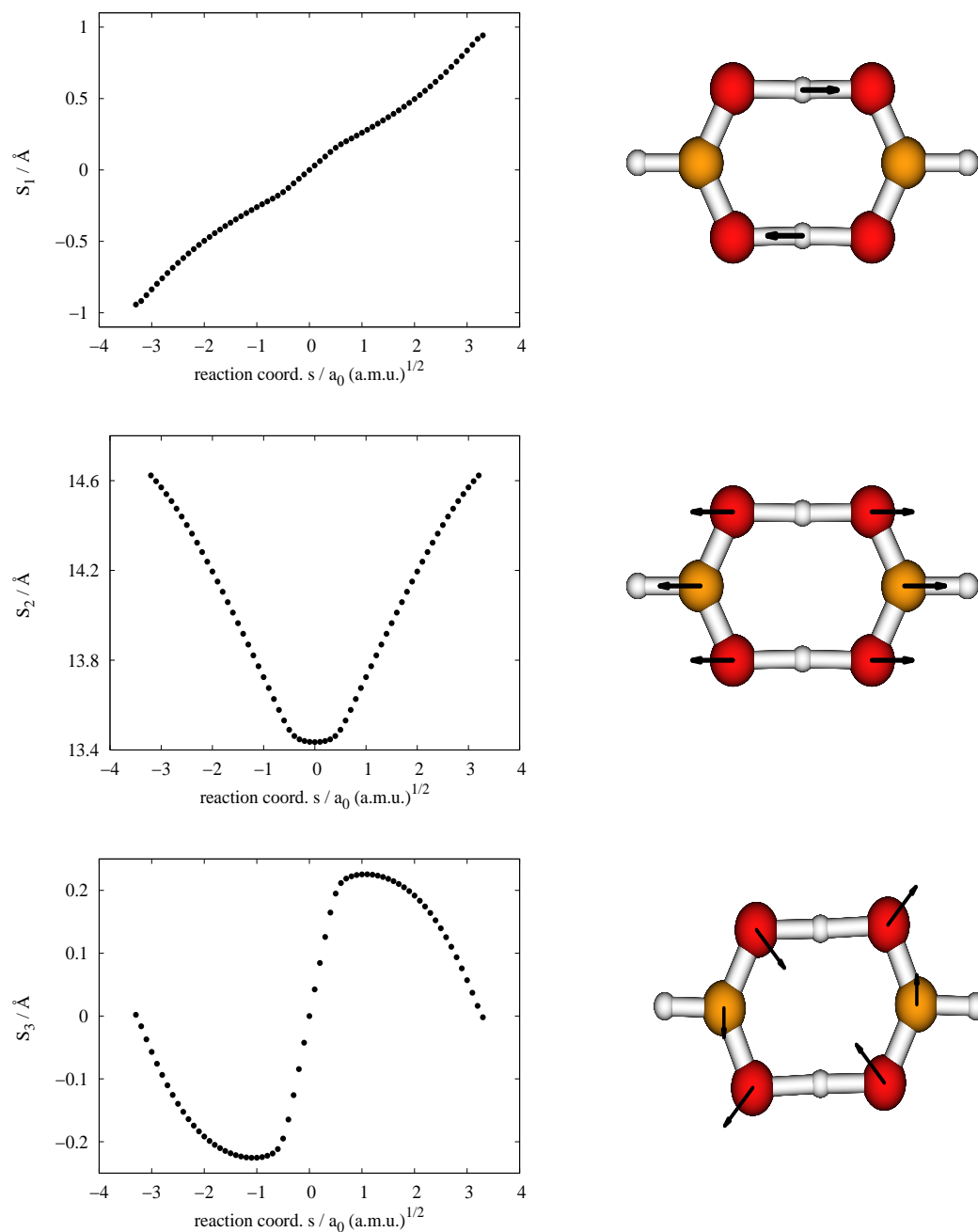


Figure 4.28: Left panel: The change of coordinates S_1 , S_2 and S_3 along the IRP for HAT reaction in the formic acid dimer. Right panel: Cartesian displacements corresponding to the coordinates S_1 , S_2 and S_3 . Only the most important displacements are shown.

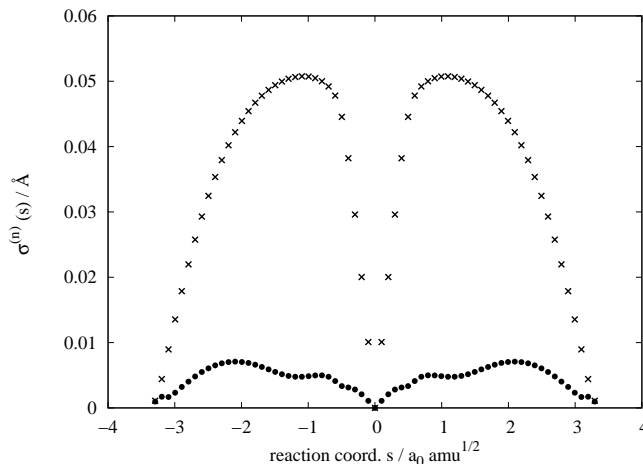


Figure 4.29: RMS difference between the IRP geometries and its projection on the plane spanned by S_1 and S_2 coordinates (crosses) and on the reaction space spanned by S_1 , S_2 and S_3 (solid dots).

obtained by inverting the Eq. (4.20). The RMS geometry difference $\sigma^{\tilde{n}}$ for $\tilde{n} = 2, 3$ are shown in Figure 4.29. By definition the RMS difference vanishes at the transition state but not at the minima where it is made very small, i.e., $\sigma_{s=\pm 3.3}^2$ and $\sigma_{s=\pm 3.3}^3$ are 0.0011 \AA and 0.00097 \AA in the 2D and 3D cases. Figure 4.29 also shows that the pair of symmetric and antisymmetric LAM coordinates S_1 and S_2 capture a large portion of the IRP, but it is only upon the inclusion of S_3 that the maximal difference between the IRP geometries and the projected geometries has been reduced to 0.007 \AA at $\sigma_{s=\pm 2.2}^3$. In terms of energy this corresponds to an difference of 25 cm^{-1} . Comparing Figures 4.20 and 4.29 one sees that calculated RMS differences match exactly the ones calculated when projecting the IRP geometries on a reaction space spanned by \mathbf{d}_1 , \mathbf{d}_2 and \mathbf{d}_3 vectors defined in Eqs. (3.59), (3.60) and (4.9). When comparing the Cartesian displacements corresponding to the displacements in coordinates S_1 , S_2 and S_3 with \mathbf{d}_1 , \mathbf{d}_2 and \mathbf{d}_3 vectors one finds scalar products 0.9999899 , 0.99998401 and 0.99971 which prove the collinearity between the two sets. Thus, the S_1, S_2, S_3 coordinates span the same configurational subspace as \mathbf{d}_1 , \mathbf{d}_2 and \mathbf{d}_3 vectors do. Moreover, the $\{\mathbf{d}_1, \mathbf{d}_2, \mathbf{d}_3\}$ set of vectors emerges naturally from the "mobile" coordinates by kinematic rotations aimed at spanning the configurational subspace close to the IRP.

The reaction coordinates S_1 , S_2 and S_3 account for the large amplitude hydrogen motion and span the same reaction space as \mathbf{d}_1 , \mathbf{d}_2 and \mathbf{d}_3 vectors. Consequently, the same approach as described in the last subsection can be further used to treat the remaining orthogonal degrees of freedom and to derive the form of the Hamiltonian. The procedure

has been detailed in sections 3.3.3 and 4.3.2 and only the most important issues will be given here. According to the Reaction Space Hamiltonian approach the potential $V(\mathbf{S})$ is harmonically approximated in the $S_4 \dots S_{3N-3}$ directions around the reaction space. However, since the quantum chemical packages provide the analytical forces and force constant matrices from which the translational and rotational directions are projected out it is more convenient to use the normal mode coordinates \mathbf{Q}_i of the reference D_{2h} structure instead. The later are simply related to the S_i as

$$S_i = \sum_j^{3N-9} C_{ij} Q_j \quad (4.30)$$

with \mathbf{C} being the overlap matrix.

The vectors \mathbf{Q}_i are obtained by diagonalizing the projected force constant matrix at the transition state $\mathbf{K}^{\mathcal{P}}$:

$$\mathbf{K}^{\mathcal{P}}(\mathbf{X}_{\text{TS}}) = (\mathbf{1} - \mathcal{P})\mathbf{K}^{(f)}(\mathbf{X}_{\text{TS}})(\mathbf{1} - \mathcal{P}) \quad (4.31)$$

where the projector \mathcal{P} projects out the rotational and translational directions and three reaction coordinates \mathbf{S}_1 , \mathbf{S}_2 and \mathbf{S}_3 (see Eq. (3.67)). To make the computation numerically feasible the number of \mathbf{Q}_i modes included in the treatment is reduced by considering linear combinations of the form

$$q_k = \sum_{j=1}^{N-9} c_{kj} Q_j, \quad k = 1, \dots, N-9 \quad (4.32)$$

which better describe the configurational space of interest. Other harmonic modes are set to zero. Assuming three large amplitude coordinates S_i and \tilde{n} relevant modes q_i the Reaction Space Hamiltonian read as

$$\begin{aligned} \hat{H} = & -\frac{1}{2} \sum_{i=1}^3 \frac{\partial^2}{\partial S_i^2} - \frac{1}{2} \sum_{k=1}^{\tilde{n}} \frac{\partial^2}{\partial q_k^2} + V(S_1, S_2, S_3, \mathbf{q} = 0) + \sum_{i=1}^{\tilde{n}} \left. \frac{\partial V(S_1, S_2, S_3, \mathbf{q})}{\partial q_i} \right|_{q=0} q_i \\ & + \frac{1}{2} \sum_{i,j=1}^{\tilde{n}} \left. \frac{\partial^2 V(S_1, S_2, S_3, \mathbf{q})}{\partial q_i \partial q_j} \right|_{q=0} q_i q_j \end{aligned} \quad (4.33)$$

Hamiltonian obtained in Eq.(4.33) is an analogue of an Hamiltonian defined in Eq.(4.11) and used further in section 4.3.2.

4.3.4 Summary and outlook

Table 4.21 summarized all the results concerning the ground state and excited state tunneling splitting in FAD calculated using three large amplitude approaches. The values are compared to the new VRT experimental results obtained by M. Ortlieb and M. Havenith who measured the ground state splitting in $(\text{HCOOH})_2$ as $0.0158(4) \text{ cm}^{-1}$ and the splitting in an asymmetric C-O stretching mode as $0.0100(3) \text{ cm}^{-1}$ [45]. The new assignment strongly supports the reversed assignment for the $(\text{DCOOH})_2$ given by F. Madeja and M. Havenith (ground state splitting of $0.0123(3) \text{ cm}^{-1}$ and the excited state splitting $0.0031(3) \text{ cm}^{-1}$) [14]. The new experimental results are in agreement with the theoretical predictions given in Table 4.21. The ratio of the splittings (ground state/excited state) for both quantum chemistry methods is 2.4/2.6 and finds good agreement to the experimental value of 1.59. The error of the absolute values for the splittings obtained by the RSH method is explained by the failure of the DFT theory to accurately predict the barrier height for the HAT reaction in FAD. Nevertheless apart from the region of the IRP for the HAT reaction, the tunneling dynamics is governed by all regions of the configurational space that are accessible to the ground state wave function. For instance, the IRP for the HAT in malonaldehyde is planar but it is well known that out of plane motion strongly influences the tunneling dynamics [16, 118]. To identify the regions of the configurational space that are relevant to the HAT process it is convenient to consider the difference between the reaction space spanned by $\{S_1, S_2, S_3\}$ or $\{d_1, d_2, d_3\}$ coordinates and a fully relaxed PES in internal coordinates ρ_1 and ρ_2 (Figure 4.17). The difference is quantified by inspecting the RMS differences between the geometries on a surface spanned by internal coordinates ρ_1 and ρ_2 and their projections on the reaction

Table 4.21: Results for the ground state and excited state tunneling splitting in the FAD calculated using three large amplitude approaches: Internal coordinates approach, Reaction Surface Hamiltonian (RSH)/General Approximation to the Reaction Path approach (GARP)

method	barrier height	internal	RSH	exp. [45]
B3LYP/6-311++G(3df,3pd)	2273 cm^{-1}			
ground state		0.012	0.155	0.0158
C-O stretching mode			0.0655	0.0100
B3LYP/6-31+G(d)	2973 cm^{-1}			
ground state		0.0013 [18]	0.003	0.0158
C-O stretching mode			0.001	0.0100

space calculated as

$$\sigma^{(3)}(\rho_1, \rho_2) = \frac{1}{\sqrt{N_{\text{at}}}} \left| 1 - \sum_{i=1}^3 \mathbf{d}_i \mathbf{d}_i^t (\mathbf{x}(\rho_1, \rho_2) - \mathbf{x}_{\text{TS}}) \right| \quad (4.34)$$

where $\mathbf{x}(\rho_1, \rho_2)$ corresponds to a non mass-weighted geometry with the ρ_1, ρ_2 value of the internal coordinates. Figure 4.30 shows the $V(\rho_1, \rho_2)$ potential together with the points on the potential whose RMS difference $\sigma^3(\rho_1, \rho_2)$ is less than $2 \cdot 10^{-2} \text{ \AA}$. The solid red line represents the IRP for the HAT connecting the two minima via a transition state. From Figure 4.30 one sees that d_1, d_2, d_3 or equivalent S_1, S_2, S_3 directions reproduce the full dimensional PES only in the IRP region. This is however expected as these LAM coordinates are constructed on the basis of the minima energy path which connects the transition state and the minima and thus gives no information about the shape of the potential beyond the minima. However, Figure 4.30 shows that the PES in the region which extends in the direction of increasing ρ_1 and ρ_2 values, i.e., in the dissociation limit of the dimer, is not well reproduced by $\mathbf{d}_1, \mathbf{d}_2, \mathbf{d}_3$ or S_1, S_2 and S_3 coordinates. Therefore, in future we intend to investigate the influence of a dimmer dissociative motion on the tunneling dynamics in FAD. This implies the introduction of additional degrees of freedom in the treatment described in section 4.3.3 in order to account for the full length of the dimer dissociation channels. The construction of new coordinates can be easily done by kinematic rotations (Eq.(4.28)) using the remaining $S_4, S_5 \dots S_{3N_{\text{at}}-6}$ vectors in such a

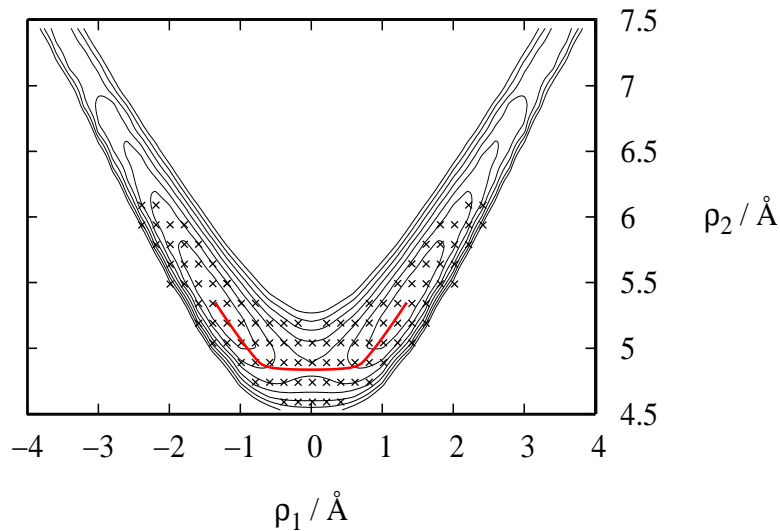


Figure 4.30: Black solid lines: $V(\rho_1, \rho_2)$ PES, the contours are drawn at each 800 cm^{-1} and the inner contour corresponds to an energy lying 800 cm^{-1} above the minimum of the PES. Crosses: geometries on a $V(\rho_1, \rho_2)$ PES with $\sigma^3(\rho_1, \rho_2) < 2 \cdot 10^{-2} \text{ \AA}$. Red solid line: the IRP for hydrogen atom transfer in FAD.

way to minimize the difference to the dimer dissociation region. A generalization of the IRP beyond the HAT region is therefore needed.

Chapter 5

Conclusion

Several methods are employed to investigate some of the basic features of hydrogen atom transfer reactions in the FAD and ACAC. These molecules serve as prototype systems for single and double hydrogen atom transfer. This is considered to be an important issue since testing the reliability of theoretical methods on simple, benchmark systems represents the key step to future quantitative treatment of the tunneling phenomena in biological systems.

The first part of the thesis was concerned with the performance of the normal mode based methods, second order perturbative treatment and non-perturbative calculations in reduced dimensionality. These methods are able to reproduce the basic features of IR spectra of hydrogen bonded molecules. For instance, the shape and the position of the OH stretch band in the FAD and ACAC are well reproduced. Also, the nature of the anharmonic couplings triggered by the formation of the hydrogen bond can be revealed. However, the normal coordinates describe the motion in the vicinity of the most stable conformation and appear to be unsuitable in reproducing the double-well shape of the potential. As a result, they are not efficient in explaining the tunneling splittings observed in high resolution ro-vibrational spectra. To investigate this aspect of the IR spectroscopy, three quantum methods capable of describing large amplitude motion of the bridging hydrogen were used in the second part of the thesis.

The most interesting points concerning the structure and dynamics of the hydrogen bond in acetylacetone are:

- The minimum energy structure of acetylacetone has C_s symmetry, while the transition state for HAT reaction has C_{2v} symmetry. The barrier height for HAT in ACAC was calculated using various ab initio, DFT and CCSD(T) theory with various basis sets and it is estimated to be $3.03 \text{ kcal mol}^{-1}$ at the CCSD(T)/cc-pVTZ//MP2(FC)/cc-pVTZ level of theory.

- It has been shown that the HAT reaction is coupled to the methyl group rotation, but that the two reactions do not occur simultaneously. Starting from the minimum, the HAT reaction takes place only after the methyl groups have reached an eclipsed conformation. The barrier height for the rotation of the distal methyl group in ACAC is estimated to be $0.27 \text{ kcal mol}^{-1}$ at the CCSD(T)/cc-pVTZ//MP2(FC)/cc-pVTZ level of theory.
- Within the normal mode approach in reduced dimensionality it was concluded that at least two rotamers of ACAC contribute to the extreme broadness of OH-stretch band in ACAC. Namely, the transitions in the OH stretching band arising from the minimum energy structure and from the eclipsed rotamer of ACAC are separated by more than 500 cm^{-1} . In addition, it is found that the IR spectrum of ACAC in the O-H stretching region displays some interesting features like disappearance of the ν_{OH} fundamental, resonance enhanced intensities and mixing with the low frequency modes of the molecular frame. These features can be considered as general features of the vibrational dynamics in hydrogen bonded systems.
- The treatment of the HAT reaction in ACAC using large amplitude internal coordinates revealed a ground state tunneling splitting of 116 cm^{-1} . An excited state tunneling splitting of 850 cm^{-1} is predicted for the OH-stretching vibration. Furthermore, it was concluded that the three-maxima shape of the C=O stretch band could be due to the OH-stretching doublet and accordingly a consequence of the double-well hydrogen atom motion.

The most interesting points concerning the structure and dynamics of the hydrogen bond in the formic acid dimer are:

- Both the second order perturbative treatment and a normal mode approach in reduced dimensionality which were used to investigate the OH stretching mode region in the IR spectrum of FAD showed that the red shift of the asymmetric OH stretching vibration in FAD is caused by Davydov coupling to the IR inactive symmetric OH stretch. Anharmonic couplings to low frequency modes of the dimer and Fermi resonances to mid-infrared modes contribute to the width and to the shape of the OH stretching band, but in minor extent to its position.
- It has been shown that the excitation of the asymmetric C-O vibration suppresses the tunneling motion. This result is in accordance with the new assignment of the VRT spectra of FAD [45]. Specifically, a ground state tunneling splitting in FAD was found to be 2.5 times larger than in the asymmetric C-O stretching mode. It has also been shown that the decrease of the tunneling splitting emerges

from the mixing of the reactions space containing the minimum energy path and CO-oscillator wavefunctions. These theoretical results together with the new experimental results ended the controversy concerning the assignment of the VRT spectra of FAD [14].

The most important points concerning the construction and use of LAM coordinates are

- The internal coordinates reproduce the absolute value for the ground state splitting that appear to be in good agreement with the experiment, but the kinetic coupling terms and variable, coordinate dependent reduced masses complicate the form of the vibrational Hamiltonian. Apart from these technical complications, the calculation of the tunneling splitting in the excited vibrational modes is far from being straightforward.

In the case of the HAT reactions the multidimensional nature of the hydrogen atom vibration is reflected in the strong coordinate dependence of the elements of Wilson G -matrix. In order to reproduce the high-resolution VRT results quantitatively accurate kinematic couplings have to be included in the treatment.

- The construction of the LAM coordinates from the stationary points on the IRP, i.e., the left and right-hand minimum energy structures and the transition state for the reaction as proposed by Takada et al. [93] has been applied to the FAD case in order to reproduce the energetics and geometries on the whole IRP. It has been shown that these coordinates were not sufficient for reproducing the IRP region of the FAD potential. An additional coordinate constructed from two non-stationary points had to be introduced in the treatment to fully confine the IRP. This 3D reaction space has been shown to account for the ground state splitting in FAD. Hence, apart from the two LAM coordinates introduced in Ref. [93] and used in Refs. [16, 19] an introduction of additional relevant coordinates depends on system at hand.
- Starting from mobile coordinates, the optimization scheme which tailors coordinates along a predefined general reaction path is presented for the first time. This method will be referred as to a *generalized approximation to the reaction path* (GARP). Compared to other methods it provides a *complete* set of orthogonal coordinates. Furthermore, the GARP procedure was applied to the FAD case and three LAM coordinates capable of describing the IRP were found to be collinear to the LAM coordinates proposed by Takada et al.[93]. Furthermore, the coordinates reproduce the barrier height of the full-dimensional potential and no further optimization is needed in order to reproduce the energetics of the full-dimensional

case. In both cases the remaining degrees of freedom are easily included in the treatment via the harmonic approximation and the vibrational excited dynamics can be treated within the Reaction Surface Hamiltonian approach. The only drawback is represented by the fact that both methods are confined to the minimum energy path. Possible extensions of the reaction space beyond the minima requires new algorithms aimed at generalizing the concept of Intrinsic Reaction Path.

Bibliography

- [1] S. Hammes-Shiffer, *Chem. Phys. Chem.* **3** (202) 33–42.
- [2] L. Rodriguez-Santiago, M. Sodupe, J. Bertran, *J. Am. Chem. Soc.* **121** (1999) 8882–8890.
- [3] H. H. Limbach, J. Manz, Hydrogen transfer: Experiment and theory, *Ber. Bunsenges. Phys. Chem.* **102** (1998) special issue.
- [4] W. W. Cleland, M. M. Kreevoy, *Science* **264** (1994) 1887–1890.
- [5] S. Hammes-Shiffer, *J. Chem. Phys.* **105** (1996) 2236–2246.
- [6] A. Kohen, R. Cannio, S. Bartolucci, J. P. Klinman, *Nature* **399** (1999) 496–499.
- [7] V. H. J. Florian, P. Hobza, *J. Am. Chem. Soc.* **116** (1994) 1457–1460.
- [8] M. L. Huggins, *J. Phys. Chem.* **40** (1936) 723–731.
- [9] G. Buntkowsky, H. Eckert, E. Roduner, *Z. Phys. Chem.* **217** (2003) special issue.
- [10] S. Bratož, J. Leicknam, G. Gallot, H. Ratajczak, in: T. Elsaesser, H. Bakker (Eds.), *Ultrafast Hydrogen Bonding Dynamics and Proton Transfer Processes in the Condensed Phase*, Kluwer Academic Publisher, Dordrecht, 2002, p. 5.
- [11] K. Giese, M. Petković, H. Naundorf, O. Kühn, *Physics Reports* **430** (2006) 211–276.
- [12] R. M. Badger, S. H. Bauer, *J. Chem. Phys.* **5** (1937) 839–851.
- [13] S. Bratož, D. Hadži, G. Rossmly, *Trans. Faraday Soc.* **52** (1956) 464–470.
- [14] F. Madeja, M. Havenith, *J. Chem. Phys.* **117** (2002) 7162–7168.
- [15] C. Duan, D. Luckhaus, *Chem. Phys. Lett.* **391** (2004) 129–133.
- [16] K. Yagi, T. Taketsugu, K. Hirao, *J. Chem. Phys.* **115** (2001) 10647–10654.

Bibliography

- [17] N. Shida, P. F. Barbara, J. Almlöf, *J. Chem. Phys.* **94** (1990) 3633–3643.
- [18] D. Luckhaus, *J. Phys. Chem.* **110** (2005) 3151–3158.
- [19] K. Giese, O. Kühn, *J. Chem. Phys.* **123** (2005) 0054315(1–14).
- [20] G. V. Mil'nikov, K. Yagi, H. Nakamura, T. Taketsugu, T. Hirao, *J. Chem. Phys.* **119** (2003) 10–13.
- [21] R. Meyer, T.-K. Ha, *Mol. Phys.* **101** (2003) 3263–3276.
- [22] G. V. Mil'nikov, K. Yagi, H. Nakamura, T. Taketsugu, T. Hirao, *J. Chem. Phys.* **120** (2004) 5036–5045.
- [23] A. Viel, M. Coutinho-Neto, U. Manthe, *J. Chem. Phys.* **126** (2007) 024308(1–9).
- [24] T. Baba, T. Tanaka, I. Morino, K. M. T. Yamada, K. Tanaka, *J. Chem. Phys.* **110** (1999) 4131.
- [25] G. M. Florio, T. S. Zwier, E. M. Myshakin, K. D. Jordan, E. L. Sibert, *J. Chem. Phys.* **118** (2003) 1735–1746.
- [26] K. Heyne, N. Huse, E. Nibbering, T. Elsaesser, S. Mukamel, *J. Chem. Phys.* **121** (2004) 902–913.
- [27] A. Horsewill, A. M. Alsanoozi, C. J. Carlisle, *J. Phys. C* **20** (1987) L869–L874.
- [28] H. Ogoshi, K. Nakamoto, *J. Chem. Phys.* **45** (1966) 3113–3120.
- [29] S. F. Tayyari, F. Milani-nejad, *Spectrochim. Acta A* **56** (2000) 2679–2691.
- [30] J. Dannenberg, R. Rios, *J. Phys. Chem. A* **98** (1994) 6714–6718.
- [31] J. Mavri, J. Grdadolnik, *J. Phys. Chem. A*, **105** (2001) 2039–2044.
- [32] J. Mavri, J. Grdadolnik, *J. Phys. Chem. A*, **105** (2001) 2045–2051.
- [33] M. Johnson, N. Jones, A. Geis, A. Horsewill, H.P.Trommsdorff, *J. Chem. Phys.* **116** (2002) 5694–5700.
- [34] N. Došlić, O. Kühn, *Z. Phys. Chem.* **217** (2003) 1507–1524.
- [35] Z. Smith, E. B. Wilson, R. W. Duerst, *Spectrochim. Acta A* **39** (1983) 1117.
- [36] Y. T. Chang, Y. Yamaguchi, W. H. Miller, H. F. Schaeffer, *J. Am. Chem. Soc.* **109** (1987) 7247–7253.

- [37] P. Jurečka, P. Hobza, *Chem. Phys. Lett.* **365** (2002) 89–94.
- [38] C. S. Tautermann, A. F. Voegelé, K. R. Liedl, *J. Chem. Phys.* **120** (2004) 631–637.
- [39] N. Shida, P. F. Barbara, J. Almlöf, *J. Chem. Phys.* **91** (1989) 4061–4072.
- [40] T. Carrington, W. H. Miller, *J. Chem. Phys.* **84** (1986) 4364–4370.
- [41] M. V. Vener, O. Kühn, J. M. Bowman, *Chem. Phys. Lett.* **349** (2001) 562–570.
- [42] G. V. Mil'nikov, O. Kühn, H. Nakamura, *J. Chem. Phys.* **123** (2005) 074308(1–9).
- [43] Z. Smedarchina, A. Fernandez-Ramos, W. Siebrand, *Chem. Phys. Lett.* **395** (2004) 339–345.
- [44] Z. Smedarchina, A. Fernandez-Ramos, W. Siebrand, *J. Chem. Phys.* **122** (2005) 134309(1–12).
- [45] M. Ortlieb, M. Havenith, *J. Phys. Chem., in press*.
- [46] K. Iijima, A. Ohnogi, S. Shibata, *J. Mol. Struct.* **156** (1987) 111–118.
- [47] R. Srinivasan, J. S. Feenstra, S. T. Park, S. Xu, A. H. Zewail, *J. Am. Chem. Soc.* **126** (2004) 2266–2267.
- [48] A. Camerman, D. Mastropalo, N. Camerman, *J. Am. Chem. Soc.* **105** (1983) 1584–1586.
- [49] W. Egan, G. Gunnarsson, T. E. Bull, S. Forsen, *J. Am. Chem. Soc.* **99** (1977) 4568–4572.
- [50] S. F. Tayyari, T. Zeegers-Huyskens, J.L. Wood, *Spectrochim. Acta A* **35** (1979) 1289–1295.
- [51] W. Caminati, J. U. Grabow, *J. Am. Chem. Soc.* **128** (2006) 854–857.
- [52] V. Sliznev, S. Lapshina, G. Girichev, *J. Struct. Chem.* **43** (2002) 47–55.
- [53] A. H. Lowrey, C. George, P. D'Antonio, J. Karle, *J. Am. Chem. Soc.* **93** (1971) 6399–6403.
- [54] A. L. Andreassen, S. H. Bauer, *J. Mol. Struct.* **12** (1972) 381–403.
- [55] T. Chiavassa, P. Verlaque, L. Pizzala, P. Roubin, *Spectrochim. Acta A* **50** (1994) 343–351.

Bibliography

- [56] B. Cohen, S. Weiss, *J. Phys. Chem.* **87** (1984) 3606–3610.
- [57] O. Kühn, *J. Phys. Chem.* **106** (2002) 7671–7679.
- [58] K. Belharaya, P. Blaise, O. Henri-Rousseau, *Chem. Phys.* **293** (2003) 9.
- [59] Y. Kim, *J. Am. Chem. Soc.* **118** (1996) 1522–1528.
- [60] S. Miura, M. E. Tuckerman, M. L. Klein, *J. Chem. Phys.* **109** (1998) 5290–5299.
- [61] H. Ushiyama, K. Takatsuka, *J. Chem. Phys.* **115** (2001) 5903–5912.
- [62] B. S. Jursic, *J. Mol. Struct.* **417** (1997) 89–94.
- [63] A. Almenningen, O. Bastiansen, T. Motzfeld, *Acta Chem. Scand.* **23** (1969) 2848–2864.
- [64] S. Tsuzuki, H. P. Lüthi, *J. Chem. Phys.* **114** (2001) 3949–3957.
- [65] A. Garg, *Am. J. Phys.* **68** (2000) 430–436.
- [66] P. R. Bunker, P. Jensen, *Molecular Symmetry and Spectroscopy*, NRC Research Press, Ottawa, 1998.
- [67] M. J. Frisch, et al., *Gaussian 03, Revision B.05*, Gaussian, Inc., Pittsburgh PA, <http://www.gaussian.com> (2003).
- [68] M. Schmidt, et al., *Gamess version 2000*, Gordon research group at Iowa State University, <http://www.msg.chem.iastate.edu/gamess/> (1993).
- [69] S. Carter, N. C. Handy, *J. Chem. Phys.* **113** (2000) 987–993.
- [70] C. F. Jackels, Z. Gu, D. G. Truhlar, *J. Chem. Phys.* **102** (1995) 3188–3201.
- [71] J. E. B. Wilson, J.C. Decius, P. C. Cross, *Molecular Vibrations, The Theory of Infrared and Raman Vibrational Spectra*, Dover Publications, New York, 1995.
- [72] H.-J. Werner, P. J. Knowles, R. Lindh, F. R. Manby, M. Schütz, et al., *Molpro, Molpro version 2006.1*, Cardiff, UK, <http://www.molpro.net> (2006).
- [73] J. O. Jung, R. B. Gerber, *J. Chem. Phys.* **105** (1996) 10332–10347.
- [74] V. Barone, C. Manichino, *J. Mol. Struct.* **330** (1995) 365–376.
- [75] V. Barone, *J. Chem. Phys.* **120** (2004) 3059–3065.

- [76] V. Barone, *J. Chem. Phys.* **122** (2005) 04108(1–10).
- [77] T. Hrenar, H. J. Werner, G. Rauhut, *J. Chem. Phys.* **126** (2007) 134108(1–9).
- [78] N. J. Wright, R. B. Gerber, *J. Chem. Phys.* **114** (2001) 8763–8768.
- [79] J. Antony, G. von Helden, G. Meijer, B. Schmidt, *J. Chem. Phys.* **123** (2005) 014305(1–11).
- [80] L. C. Light, I. P. Hamilton, J. V. Lill, *J. Chem. Phys.* **82** (1985) 1400–1409.
- [81] Z. Bačić, J. C. Light, *Annu. Rev. Phys. Chem.* **40** (1989) 469–498.
- [82] R. Kosloff, H. Tal-Ezer, *Chem. Phys. Lett.* **127** (1986) 223–230.
- [83] C. C. Marston, G. G. Balint-Kurti, *J. Chem. Phys.* **91** (1989) 3571–3576.
- [84] B. Podolsky, *Phys. Rev.* **32** (1928) 812–816.
- [85] J. Stare, G. G. Balint-Kurti, *J. Phys. Chem.* **107** (2003) 7204–7214.
- [86] B. A. Ruf, W. H. Miller, *J. Chem. Soc., Faraday Trans. 2* **84** (1988) 1523–1534.
- [87] S. L. Baughcum, Z. Smith, E. B. Wilson, R. W. Duerst, *J. Am. Chem. Soc.* **106** (1984) 2260–2265.
- [88] K. Fukui, *J. Phys. Chem.* **74** (1970) 4161–4163.
- [89] F. Jensen, *Introduction to Computational Chemistry*, John Wiley and Sons, Sussex, 2002.
- [90] C. Gonzales, H. Schlegel, *J. Chem. Phys.* **90** (1989) 2154–2161.
- [91] W. H. Miller, N. C. Handy, J. E. Adams, *J. Chem. Phys.* **72** (1980) 99–112.
- [92] D. Tew, N. C. Handy, S. Carter, S. Irle, J. Bowman, *Mol. Phys.* **101** (2003) 3513–3525.
- [93] S. Takada, H. Nakamura, *J. Chem. Phys.* **102** (1995) 3977–3992.
- [94] D. W. Jepsen, J. O. Hirschfelder, *Proc. Nat. Acad. Sci.* **45** (1959) 249–256.
- [95] J. O. Hirschfelder, J. S. Dahler, *Proc. Nat. Acad. Sci.* **42** (1956) 363–365.
- [96] J. O. Hirschfelder, *Int. J. Quant. Chem.* (1969) 17–31.
- [97] A. D. Becke, *J. Chem. Phys.* **98** (1993) 5648–5652.

- [98] C. Adamo, V. Barone, *Chem. Phys. Lett.* **274** (1997) 242–250.
- [99] P. Pechukas, *J. Chem. Phys.* **78** (1976) 365.
- [100] T. Taketsugu, N. Tajima, K. Hirao, *J. Chem. Phys.* **105** (1996) 1933–1939.
- [101] P. Valtazanos, K. Ruedenberg, *Theor. Chim. Acta* **69** (1986) 281–307.
- [102] W. Quapp, M. Hirsch, D. Heidrich, *Theor. Chem. Acc.* **100** (1998) 285–299.
- [103] W. Quapp, M. Hirsch, D. Heidrich, *Theor. Chem. Acc.* **112** (2004) 40–51.
- [104] S. F. Boys, F. Bernardi, *Mol. Phys.* **19** (1970) 553–566.
- [105] S. Simon, M. Duran, J. J. Dannenberg, *J. Chem. Phys.* **105** (1996) 11024.
- [106] G. H. Kwei, R. F. Curl, *J. Chem. Phys.* **32** (1960) 1592–1594.
- [107] T. Neuheuser, B. A. Hess, C. Reutel, E. Weber, *J. Phys. Chem.* **98** (1994) 6459–6467.
- [108] R. J. Renka, *ACM Trans. Math. Software* **14** (1988) 151–152.
- [109] G. H. Golub, C. F. V. Loan, *Matrix Computations*, The Johns Hopkins University Press, Baltimore, 1985.
- [110] D. Sörensen, Rice University, Houston, 1995.
- [111] R. B. Lehoucq, D. Sorensen, C. Yang, *ARPACK User's Guide: Solution of Large Scale Eigenvalue Problems with Implicitly Restarted Arnoldi Methods*, Rice University, Houston, 1997.
- [112] V. May, O. Kühn, *Charge and Energy Transfer Dynamics in Molecular Systems*, Wiley–VCH, Berlin, 2000.
- [113] F. Ito, T. Nakanaga, *Chem. Phys.* **277** (2002) 163–169.
- [114] P. Blaise, M. J. Wojcik, O. Henri-Rousseau, *J. Chem. Phys.* **122** (2005) 064306(1–12).
- [115] J. Dreyer, *J. Chem. Phys.* **122** (2005) 184306(1–10).
- [116] V. Špirko, A. Čejchan, R. Lutchny, J. Leszczynski, *Chem. Phys. Lett.* **355** (2002) 319–326.

- [117] V. Alexandrov, D. M. A. Smith, H. Rostkowska, M. J. Nowak, L. Adamowicz, W. McCarthy, *J. Chem. Phys.* **108** (1998) 9685–9693.
- [118] D. Babić, S. D. Bosanac, N. Došlić, *Chem. Phys. Lett.* **358** (2002) 337–343.
- [119] T. Taketsugu, N. Watanabe, K. Hirao, *J. Chem. Phys.* **111** (1999) 3410–3419.
- [120] D. W. Kohn, E. S. J. Robles, C. F. Logan, P. Chen, *J. Phys. Chem.* **97** (1993) 4936–4940.

Appendix A

The Eckart Equations

The Eckart equations optimize the separation of the rotational and vibrational degrees of freedom in the rotational-vibrational Schrödinger equation. For any displacement in the molecule there is an unambiguous way of rotating the molecule fixed axes (x, y, z) to the new axes system (x', y', z') in which the Eckart conditions are satisfied. The Euler angles θ, ϕ i χ are used to define the orientation of the (x, y, z) axis system to the new (x', y', z') axis system (Figure A.1).

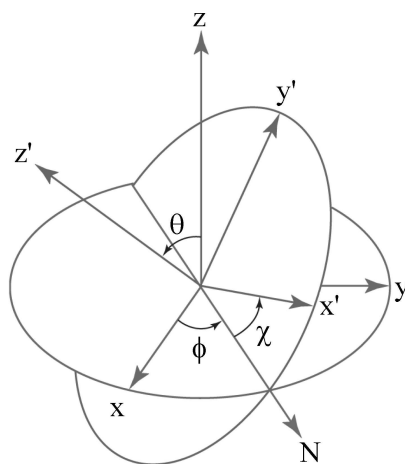


Figure A.1: The definition of the Euler angles θ, ϕ and χ that relate the orientation of the molecule fixed axes (x, y, z) to the new axes system (x', y', z') . To get from one system to the other system of axes, first the (x, y, z) system is rotated by an angle ϕ counterclockwise about the z axes (x goes to N). In the second step the intermediate axes are rotated by an angle θ counterclockwise about the N axes to get the second intermediate axes (z goes to z'). Finally, this axes are rotated counterclockwise by and angle χ about the z' axes to produce the desired (x', y', z') system of axes.

For any atom in the molecule its coordinates in the (x', y', z') axis system can be related to its coordinates in (x, y, z) axis system as:

$$\begin{bmatrix} x_i \\ y_i \\ z_i \end{bmatrix} = \begin{bmatrix} \lambda_{xx'} & \lambda_{xy'} & \lambda_{xz'} \\ \lambda_{yx'} & \lambda_{yy'} & \lambda_{yz'} \\ \lambda_{zx'} & \lambda_{zy'} & \lambda_{zz'} \end{bmatrix} \begin{bmatrix} x'_i \\ y'_i \\ z'_i \end{bmatrix} \quad (\text{A.1})$$

where

$$\begin{aligned} \lambda_{xx'} &= \cos \theta \cos \phi \cos \chi - \sin \phi \sin \chi, & \lambda_{xy'} &= \cos \theta \sin \phi \cos \chi - \cos \phi \sin \chi, \\ \lambda_{yx'} &= -\cos \theta \cos \phi \sin \chi - \sin \phi \cos \chi, & \lambda_{yy'} &= -\cos \theta \sin \phi \sin \chi - \cos \phi \cos \chi, \\ \lambda_{zx'} &= \sin \theta \cos \phi, & \lambda_{zy'} &= \sin \theta \sin \phi, \end{aligned}$$

$$\begin{aligned} \lambda_{xz'} &= -\sin \theta \cos \chi, \\ \lambda_{yz'} &= \sin \theta \sin \chi, \\ \lambda_{zz'} &= \cos \theta. \end{aligned}$$

Using the defined relations three Eckart equations:

$$\sum_i m_i (x'_i y_i - y'_i x_i) = 0 \quad (\text{A.2})$$

$$\sum_i m_i (y'_i z_i - z'_i y_i) = 0 \quad (\text{A.3})$$

$$\sum_i m_i (z'_i x_i - x'_i z_i) = 0 \quad (\text{A.4})$$

can be written as:

$$\begin{aligned} [xx']\lambda_{yx'} + [xy']\lambda_{yy'} + [xz']\lambda_{yz'} - [yx']\lambda_{xx'} - [yy']\lambda_{xy'} - [yz']\lambda_{xz'} &= 0 \\ [yx']\lambda_{zx'} + [yy']\lambda_{zy'} + [yz']\lambda_{zz'} - [zx']\lambda_{yx'} - [zy']\lambda_{yy'} - [zz']\lambda_{yz'} &= 0 \\ [zx']\lambda_{xx'} + [zy']\lambda_{xy'} + [zz']\lambda_{xz'} - [xx']\lambda_{yx'} - [zy']\lambda_{zy'} - [xz']\lambda_{zz'} &= 0 \end{aligned} \quad (\text{A.5})$$

where

$$[\alpha\tau] = \sum_{i=1}^N m_i \alpha_i^0 \tau_i$$

with $\alpha^0 = x^0, y^0, z^0$ and $\tau = x', y', z'$. The equilibrium coordinates in the molecule fixed axis (x^0, y^0, z^0) together with the displaced coordinates (x'_i, y'_i, z'_i) can be used to determine the values $[\alpha\tau]$ and to form three equations A.5. Solving this equations simultaneously, for instance by using the Newton-Raphson method, three Euler angles θ, ϕ i χ are obtained. Furthermore, using Eq. A.1 molecular coordinates which satisfy the Eckart conditions can be determined.

There is also an analytical procedure for solving the Eckart conditions [120]. The Eckart equations can be written as

$$\sum_{i=1}^N m_i [\mathbf{r}_i^0 \times \mathbf{O}\mathbf{r}_i] \quad (\text{A.6})$$

where \mathbf{O} is a 3×3 rotation matrix which rotates the geometry \mathbf{r}_i in order to satisfy the Eckart conditions with respect to the equilibrium geometry \mathbf{r}_i^0 . A solution for \mathbf{O} is given by Yaron [120]. First, one has to define a matrix \mathbf{C} with the elements

$$C_{\alpha\beta} = \sum_{i=1}^N m_i [(\mathbf{r}_i^0)_{\alpha} (\mathbf{r}_i)_{\beta}] \quad (\text{A.7})$$

where α and β denote the x, y, z coordinates of a nonplanar molecule. To satisfy the Eckart conditions one has to diagonalize the product $\mathbf{C}^+\mathbf{C}$ and get the matrix \mathbf{U} (eigenvectors of $\mathbf{C}^+\mathbf{C}$) and a diagonal matrix λ (eigenvalues of $\mathbf{C}^+\mathbf{C}$). The solution for the rotational matrix \mathbf{O} for a nonplanar molecule is given by

$$\mathbf{O} = \mathbf{U}^+ \Lambda \lambda^{1/2} \mathbf{U} \mathbf{C}^{-1} \quad (\text{A.8})$$

where Λ is a 3×3 diagonal matrix with +1 or -1 on the diagonal. Because there are 2^3 possibilities for the +/- sign when calculating the square root of λ , the matrix Λ presents the only ambiguity in the procedure. In principle, four signs are correct and they yield $\det(\mathbf{O}) = 1$ (the rest would yield $\det(\mathbf{O}) = -1$). However, the correct solution is the one that gives the rotated $\mathbf{O}\mathbf{r}_i$ geometry closest to the starting \mathbf{r}_i geometry.

For planar molecules element C_{zz} is set to unity. This assumes that the molecule is placed in xy plane and is rotated around the z axis. The problem represents the case in which the equilibrium geometry is planar and the displaced geometry is not or vice versa. Then the analytical solution does not exist because the $\mathbf{C}^+\mathbf{C}$ is not regular and the problem has to be solved numerically.

Appendix B

The Fourier Grid Hamiltonian method for solving the vibrational Schrödinger equation

The Fourier Grid Hamiltonian (FGH) method is based on the transformation between the coordinate and momentum representation of a Schrödinger equation. In the momentum representation, the kinetic energy is diagonal since the basic vectors or kets of this representation $|k\rangle$ ¹ are eigenfunctions of both linear momentum and kinetic energy operator. On the other hand, the potential is diagonal in coordinate representation since the basic vectors of this representation $|x\rangle$ are eigenfunctions of the position operator.

Using the Fourier representation of the Dirac delta function² the first derivative of the wave function can be written:

$$\begin{aligned}\frac{\partial}{\partial x}\psi(x) &= \frac{\partial}{\partial x} \int_{x'=0}^{\infty} \delta(x'-x)\psi(x')dx' \\ &= \frac{\partial}{\partial x} \int_{x'=0}^{\infty} \left\{ \frac{1}{2\pi} \int_{k=-\infty}^{\infty} \exp^{-ik(x-x')} dk \right\} \psi(x')dx' \\ &= \int_{k=-\infty}^{\infty} \left\{ \frac{1}{2\pi} \int_{k=-\infty}^{\infty} ik \exp^{-ik(x-x')} dk \right\} \psi(x')dx' \quad (\text{B.1})\end{aligned}$$

The continuous range of coordinate values x is replaced by a grid of discrete values x_i :

$$x_i = i\Delta x$$

where Δx is the spacing between the grid points. The grid size and the spacing chosen in the coordinate space determines the reciprocal grid size in momentum space. If the

¹this is the Dirac bra-ket notation in which the scalar product of vectors f and g is $\langle f | g \rangle$. If f and g are functions the scalar product is $\langle f | g \rangle = \int f^* g d\tau$

² $\delta(x-x') = \frac{1}{2\pi} \int_{k=-\infty}^{\infty} \exp^{-ik(x-x')} dk$

total length of the coordinate space is $L = N\Delta x$ then $\Delta k = 2\pi/L$ is the spacing in the momentum grid. The odd number of grid points is always used to obtain a real form of the matrix representation of the first derivative operator in the grid representation. If the values of k range from $k = -n\Delta k$ to $k = +n\Delta k$ then the value of the partial differential at the j th grid is

$$\begin{aligned} \left[\frac{\partial}{\partial x} \psi(x) \right]_{x=x_j} &= \sum_{t=1}^N \left\{ \frac{1}{2\pi} \sum_{p=-n}^n ip\Delta k \exp^{-ip\Delta k(t-j)\Delta x} \Delta k \right\} \psi_t \Delta x \\ &= \sum_{t=1}^N \left\{ -\frac{4\pi}{LN} \sum_{p=1}^n p \sin[2\pi p(j-t)/N] \right\} \psi_t \end{aligned} \quad (\text{B.2})$$

where ψ_t is the value of the wave function at the grid point x_t i.e. $\psi(x_t)$. The term in braces, which is the (j, t) th matrix element, represents the grid representation of the first derivative operator

$$\left[\frac{\partial}{\partial x} \right]_{j,t} = \left\{ -\frac{4\pi}{LN} \sum_{p=1}^n p \sin[2\pi p(j-t)/N] \right\}$$

The summation in the last equation is performed analytically [85]. A similar derivation leads to the grid representation of the second derivative and the grid representation of the kinetic energy operator from the Eq. 3.46 has the form

$$\begin{aligned} T_{\mu_1, \dots, \mu_m; \mu'_1, \dots, \mu'_m} &= -\frac{\hbar^2}{2} \sum_{r=1}^M \sum_{s=1}^M \left\{ \delta_{rs} \sum_{l=1}^{N_r} \left[\frac{\partial}{\partial q_r} \right]_{q_r, \mu_r; q_r, l} \left[\frac{\partial}{\partial q_r} \right]_{q_r, l; q_r, \mu'_r} \right. \\ &\times G^{rs}(q_{r,l}, q_{s, \mu_s}; q_{i, \mu_i}) + (1 - \delta_{rs}) \left. \left[\frac{\partial}{\partial q_r} \right]_{q_r, \mu_r; q_r, \mu'_r} \left[\frac{\partial}{\partial q_r} \right]_{q_s, \mu_s; q_s, \mu'_s} \right\} \prod_{i \neq r, s}^M \delta_{\mu_i, \mu'_i} \end{aligned} \quad (\text{B.3})$$

The notation q_{r, μ_r} indicates the grid point μ_r of the coordinate q_r . $G^{rs}(q_{r,l}, q_{s, \mu_s}; q_{i, \mu_i})$ indicates that among the arguments of the G -matrix the q_{i, μ_i} term stands for all the coordinates other than the q_r and q_s . The grid representation of the potential is

$$V_{\mu_1, \dots, \mu_M; \mu'_1, \dots, \mu'_M} = V(q_{1, \mu_1}, \dots, q_{M, \mu_M}) \prod_{i=1}^M \delta_{\mu_i, \mu'_i} \quad (\text{B.4})$$

The overall grid representation of the Hamiltonian is the sum of the terms (B.3) and (B.4). The vibrational eigenvalues and eigenfunctions are obtained by diagonalizing the Hamiltonian matrix.

Appendix C

List of abbreviations

C.1 Notation

χ_{ij}	elements of the anharmonic correction matrix
δ_{ij}	Kronecker delta ($\delta_{ij} = 1$ for $i = j$, $\delta_{ij} = 0$ for $i \neq j$)
\mathbf{d}_i	large amplitude coordinates defined in Ref. [93]
G^{rs}	G -matrix element
$\hat{\mathbf{H}}$	Hamilton operator
\mathbf{I}	moment of inertia tensor
\hat{J}_i	angular momentum operator
$\epsilon_{\alpha\beta\gamma}$	unit antisymmetric tensor
\mathbf{K}	force constant matrix, also called Hessian matrix
μ	reduced mass
m_i	mass of the particle i
M	mass of the molecule
\tilde{n}	dimensionality of the problem
N_{at}	number of atoms in the molecule
ω_i	vibrational frequency
\mathcal{P}, \mathcal{R}	projector operators
\hat{P}_i	momentum operator
q	linear combination of normal modes Q_i
Q_i	normal coordinate
ρ	internal coordinate
\mathbf{r}_i	Cartesian coordinates for particle i in a molecule fixed system
\mathbf{R}_i	Cartesian coordinates for particle i in a space fixed system
σ	root mean square difference
\mathbf{S}_i	large amplitude "mobile" coordinates

T	kinetic energy
\mathcal{T}	molecular symmetry transformation
V	potential energy
\mathbf{X}	mass-weighted Cartesian coordinates
$\mathbf{Y}_i^{[\widetilde{\text{ND}}]}$	the so-called reduced normal modes
$\mathbf{Y}_i^{(f)}$	full normal modes at the minimum
ζ_{lk}	Coriolis coupling constants

C.2 Abbreviations

ACAC	acetylacetone
ANTI	anti- <i>enol</i> structure of acetylacetone
B3LYP	exchange-correlation functional, Becke 1-parameter functional for the exchange Lee, Yang and Parr functional for correlation
B1LYP	exchange-correlation functional, Becke 3-parameter functional for the exchange Lee, Yang and Parr functional for correlation
BSSE	basis set superposition error
CCSD(T)	couple cluster singles doubles with perturbative evaluation of triple excitations
CISD	configuration interaction method, includes single and double electronic excitations
CISD+T	configuration interaction method, includes single, double and triple electronic excitations
DFT	density functional theory
DOF	degree of freedom
FA	formic acid monomer
FAD	formic acid dimer
FC	frozen core approximation
FGH	Fourier grid Hamiltonian method for solving the nuclear Schrödinger equation
GARP	general approximation to the reaction path method
HAT	hydrogen atom transfer reaction
HB	hydrogen bond
HF	Hartree-Fock method
IRC	intrinsic reaction coordinate
IRP	intrinsic reaction path
LAM	large amplitude motion
MP2	Möller-Plesset second order perturbation theory
MSM	modified Shepard method for interpolation
MA	malonaldehyde

PES	potential energy surface
RSH	reaction surface Hamiltonian
RMS	root mean square
SYN	global minimum structure of acetylacetone
TS	transition state
TS2	acetylacetone conformer with eclipsed conformation of methyl groups
TS3	transition state for the hydrogen atom transfer reaction in acetylacetone
WKB	Wentzel-Kramers-Brillouin theory
VRI	valley-ridge inflection point
VRT	vibration rotation tunneling spectroscopy
VSCF	vibrational self-consistent field method

Rođena sam 15. prosinca 1979. godine u Slavonskom Brodu gdje sam završila osnovnu školu i s odličnim uspjehom maturirala 1998. godine u Općoj gimnaziji "Matija Mesić". Od iste sam godine student Kemijskog odsjeka Prirodoslovno-matematičkog fakulteta Sveučilišta u Zagrebu, smjer diplomirani inženjer kemije. Diplomirala sam 28. veljače 2003. s tezom na području fizikalne kemije pod naslovom: "Teorijski pristup reakciji prijenosa vodika u acetalacetonu". Od srpnja 2003. zaposlena sam u Grupi za teorijsku kemiju na Institutu Ruđer Bošković gdje radim na izradi doktorske teze pod vodstvom dr. Nađe Došlić. Od ožujka do kolovoza 2005. boravila sam u grupi Prof. Jörna Manza na Freie Universität u Berlinu.

Znanstveni radovi u časopisima:

1. I. Matanović, N. Došlić, Z. Mihalić: “*Exploring the potential energy surface for proton transfer in acetylacetone*”, *Chem. Phys.* **306** (2004.) 201-207
2. I. Matanović, N. Došlić: “*Infrared Spectroscopy of the Intramolecular Hydrogen Bond in Acetylacetone - a Computational Approach*”, *J. Phys. Chem. A* **109** (2005.) 4185-4194
3. I. Matanović, N. Došlić: “*Anharmonic Vibrational Spectra of Acetylacetone*”, *Int. J. Quant. Chem.* **106** (2005.) 1367-1374
4. G. Pavlović, V. Tralić-Kulenović, M. Vinković, D. Vikić-Topić, I. Matanović, Z. Popović: “*Supramolecular amide and thioamide synthons in hydrogen bonding patterns of N-aryl-furamides and N-aryl-thiofuramides*”, *Struc. Chem.* **17** (2006.) 275-285
5. I. Matanović, N. Došlić: “*Theoretical modeling of the formic acid dimer infrared spectrum: Shaping the O-H stretch band*”, *Chem. Phys.* **338** (2007.) 121-126
6. I. Matanović, N. Došlić, O. Kühn: “*Ground and Asymmetric CO stretch Excited State Tunneling Splittings in the Formic Acid Dimer*”, *J. Chem. Phys.* **127** (2007.) 014309(1-7)

Priopćenja znanstvenim skupovima:

1. G. Kovačević; I. Matanović, N. Došlić: “*Hydrogen atom transfer in acetylacetone: ab initio approach*”, Brijuni conference: Space, Time and Life, Brijuni, Croatia, 26-30.08.2002.
2. I. Matanović, N. Došlić: “*Intramolecular hydrogen bond in acetylacetone: Infrared spectroscopy and tunneling dynamics*”, The 18th International Conference on High Resolution Molecular Spectroscopy, Prague, Czech Republic, 8.10-12.10.2004.
3. I. Matanović, N. Došlić, O. Kühn: “*Quantum dynamics of large amplitude mo-*

tion”, NATO Advanced Research Workshop on Remote Sensing of the Atmosphere for Environmental Security, Rabat, Morocco, 16-19.11. 2005.

4. I. Matanović, N. Došlić, O. Kühn, B. R. Johnson: “*Quantum treatment of large amplitude motion in hydrogen bonded systems*”, Biannual Conference on Chemistry Chem.04, Cairo, Egypt, 04.03-08.03.2006.

5. I. Matanović, N. Došlić, O. Kühn: “*Quantum treatment of large amplitude motion in the formic acid dimer*”, The 2nd Opatija meeting on Computational Solutions in the Life Sciences, Opatija, 04.09.-09.09.2007.